Università degli Studi di Trento

PhD thesis

A tunable Bose-Einstein condensate for quantum interferometry

Candidate: **Manuele Landini**

Supervisor: **Prof. Giovanni Modugno**

Supervisor: **Prof. Augusto Smerzi**

24° cycle of the phd school in physics (2008/2009-2010/2011)

Contents

Chapter 1

Introduction

Since the first experimental realization of a Bose-Einstein condensate (BEC) in 1995[1], increasing interest has grown around these particular objects. The principal reason is that BECs are macroscopic, therefore easily observable, but their behavior is completely dominated by their wave nature. Thanks to this property a lot of exciting research was carried out using BECs, spanning many different research fields[2]. For example the observation of their superfluid behavior, the most striking evidence being the formation of quantized vortices[3], has led to test various theories developed in the context of superfluid Helium. BECs can be also used to simulate interesting phenomena of condensed matter physics like Andersson localization[4, 5], the superfluid to Mott insulator transition[6] and many others. Recently the achievement of single atom and single site resolution in such systems opens a new era of observations in this direction[7]. BECs in optical lattice represents also appealing candidates for quantum computation[8] thanks to their long coherence times, good scalability, and the control of interactions between atoms via Feshbach resonances[9, 10, 11].

The subject of this thesis is the use of BECs for atom interferometry[12, 13]. The standard way atom interferometry is today performed is by interrogating free

falling samples of atoms[14]. The employed samples are cold (but not condensed) to have high coherence, and dilute, not to interact significantly with each other. This technique represents nowadays an almost mature field of research in which the achievable interferometric sensitivity is bounded by the atomic shot noise. Until a few years ago the employment of BECs in such devices was strongly limited by the effect of the interactions between the condensed atoms. This obstacle is today removable exploiting interaction tuning techniques. The use of BECs would be advantageous for atom interferometry inasmuch they represents the matter analogue of the optical laser providing the maximum coherence allowed by quantum mechanics. In this direction, enhanced phase coherence was demonstrated employing almost non-interacting samples[15]. Moreover, non-linear dynamic can be exploited in order to prepare entangled states of the system. The realization of entangled samples can lead to sub-shot noise sensitivity of the interferometers[16]. At today very nice proof-of-principle experiments have been realized in this direction[17, 18] but a competitive device is still missing.

This thesis work is inserted in a long term project whose goal is the realization of such a device. The basic operational idea of the project starts with the preparation of a BEC in a double well potential. By the effect of strong interactions the atomic system can be driven into an entangled state. Once the entangled state is prepared, interactions can be "switched off" and the interferometric sequence performed. The two modes of the interferometer that we want to build will be represented by the two ground states of two spatially separated potential wells created via optical potentials. The measured phase will be sensitive to the energy difference between the wells. The use of a trapped configuration would also allow for very long phase accumulations as compared to a free-falling scheme.

This thesis begins with the description of the apparatus for the production of tunable BECs to be used in the interferometer. We chose to work with ^{39}K atoms

because this atomic species presents many convenient Feshabch resonances at easily accessible magnetic field values. The cooling of this particular atomic species presents many difficulties, both for the laser and evaporative cooling processes. For this reason, this was the last alkaline atom to be condensed. Its condensation up to now was only possible by employing sympathetic cooling with another species[19, 20]. In this thesis our solutions to the various cooling issues is reported. In particular we realized sub-Doppler cooling for the first time for this species and we achieved condensation via evaporation in an optical dipole trap taking advantage of a Feshbach resonance. In the last part of this work, are presented original calculations for the effects of thermal fluctuations on the coherence of a BEC in a double well, discussing the interplay between thermal fluctuations and interactions in this system. Estimations and feasibility studies regarding the double well trap to be realized are also reported. This kind of calculations are part of the design process in order to identify realistic operational parameters and optimized design strategies for the realization of the double well interferometer.

In more details, Chapter 2 contains an introduction to the theory of atomic cooling (laser cooling and evaporative cooling). In Chapter 3 are revised the basic aspects of quantum interferometry. The details about the building and operation of the experimental apparatus are given in Chapter 4. The achievement of sub-Doppler cooling and the details of the laser cooling procedures are the subject of Chapter 5. The optimization of the optical and magnetic trapping techniques, as well as the achievement of condensation in single species operation are reported in Chapter 6. In Chapter 7 are given the theoretical calculations about thermal effects on the condensate coherence together with calculations regarding the realization of the double well.

Chapter 2

Theory

Here I give the basic theoretical background for the physical phenomena explored in this thesis. Sec.2.1 of the chapter describes the cooling techniques used to cool a thermal gas of atoms to the extremely low temperatures that are necessary to achieve Bose-Einstein condensation (BEC). Sec.2.2 recalls the principal features of this quantum state of matter. In Sec.2.3 is described the tool of Fano-Feshbach resonances, used to control the atomic interactions in the BEC. In Sec.2.4 is introduced the theoretical framework for the description of a double well Mach-Zehnder atomic interferometer.

2.1 Laser and evaporative cooling

The two basic techniques used to reach low temperatures in alkaline's atomic gases are laser cooling and evaporative cooling. Laser cooling allows to cool a gas from room temperature down to a few μK. Evaporative cooling is instead used to reach the few hundreds of nK that are necessary to reach the BEC transition.

2.1.1 Laser cooling

In the description of laser cooling I am going to make use of the semi-classical picture for the atomic interaction with the light field[21]. In doing this, I will treat the internal degrees of freedom of the atom in a fully quantum mechanical way. The external degrees of freedom (position and momentum), as well as the light field, will instead be treated classically. To do so one has to be sure that the atomic position and velocity are well defined during the interaction with light

$$\Delta x \ll \lambda \tag{2.1}$$

$$k\Delta v \ll \Gamma \quad . \tag{2.2}$$

Here Δx is the spatial extension of the atomic wavepacket, which is given by the De Broglie wavelength; λ is the wavelength of the laser light, and k=$2\pi/\lambda$ is the wavenumber. Δv is the velocity spreading of the atomic wavepacket. Γ is the scattering rate which is given by Γ=$2\pi/\tau$, with τ the radiative lifetime of the excited atomic level. By writing the Heisenberg indetermination principle for the conjugated variables of the atomic motion and making use of the above equations the following condition can be obtained:

$$E_R = \frac{\hbar^2 k^2}{2m} \ll \hbar\Gamma \tag{2.3}$$

in which $\hbar = h/2\pi$ with h the Planck constant.

The quantity on the left-hand-side is the recoil energy that an atom gets from the light field in an absorption event. This is also called the broadband condition[22]. It ensures that the interaction with the light field does not change significantly the atomic energy. If 2.3 is verified the atomic conditions don't change significantly over many absorption re-emission cycles. For the cooling transition of ^{39}K the ratio $\hbar\Gamma/\mathrm{E}_R$ is about 350.

Under this condition it makes sense to consider the mean optical dipole force **F** that the light exerts on an atom moving with velocity **v** at a given position **x**.

Given the electric field **E** generated by a monochromatic laser beam of polarization unit vector $\widehat{\epsilon}$, field amplitude E, angular frequency ω_L=2πc/λ and phase ϕ:

$$\mathbf{E} = \widehat{\epsilon}(\mathbf{x})\frac{E(\mathbf{x})}{2}e^{-i(\omega_L t-\phi(\mathbf{x}))} + c.c. \quad . \tag{2.4}$$

The mean force the light field exerts on an atom is:

$$\mathbf{F} = \sum_{i=x,y,z} d_i \nabla E_i \qquad . \tag{2.5}$$

Here **d** is the averaged atomic dipole operator:

$$\mathbf{d} = \langle \mathbf{D} \rangle = Tr(\rho_{at}\mathbf{D}) \quad , \tag{2.6}$$

ρ_{at} is the steady-state atomic-density operator, given by the solution of the optical Bloch equations (OBE)[23].

In the simple case of a two-level atom at rest, the expression for the force has two contributions: the radiation pressure force and the dipole force

$$\mathbf{F}_{RP} = \frac{\hbar\Gamma}{2}\frac{s}{1+s}\nabla\phi \quad , \tag{2.7}$$

$$\mathbf{F}_{dip} = -\frac{\hbar\delta}{2}\frac{\nabla s}{1+s} \quad . \tag{2.8}$$

Here δ=ω_L-ω_A is the detuning from the atomic transition and s is the saturation parameter

$$s = \frac{\Omega^2/2}{\delta^2 + \Gamma^2/4} \tag{2.9}$$

Ω=E$\mathbf{d}_0\widehat{\epsilon}/\hbar$ is the Rabi frequency and $\mathbf{d}_0$ is the matrix element of the dipole operator between the ground- and the excited-state electronic wavefunctions.

Let us discuss the effect of these two forces. For the case of a single plane wave ($\phi(x) = kx$ and s=const) the dipole force is zero and the radiation pressure is:

$$\mathbf{F}_{RP} = \hbar\mathbf{k}\frac{\Gamma}{2}\frac{s}{1+s} \tag{2.10}$$

this force can be interpreted as the viscous force coming from scattering of photons at a rate γ=$\frac{\Gamma}{2}\frac{s}{1+s}$. The absorbed photon changes the atomic momentum by ħk, and

the spontaneously re-emitted photon takes off in a random direction, not changing, on average, the atomic momentum. The acceleration that this force can cause on a potassium atom for $s \gg 1$ is 2.4×10^5 m/s^2, which is sufficient to stop an atom moving at 250 m/s (typical velocity for an atom at room temperature) over a distance of 12 cm in a ms.

To have a non zero dipolar force, it is necessary to allow a spatial variation of the beam amplitude, or, in other words, one needs to deal with several plane waves. The dipolar force is originated by the redistribution of photons that an atom can operate by absorbing a photon from one plane wave and emitting it by stimulated emission in another one. The dipolar force can be derived from a potential

$$U_{dip} = \frac{\hbar\delta}{2}\ln(1+s(\mathbf{x})) \quad , \tag{2.11}$$

it is thus conservative and it can be used for trapping. The dipole potential is related to the light shift or AC Stark shift Δ_{AC} by $U_{dip} = \hbar\Delta_{AC}$. In the limit of low saturation ($s \ll 1$) there is a simple relation between scattering rate and dipole potential

$$\gamma = \frac{\Gamma}{\hbar\delta}U_{dip} = \frac{\Gamma}{\delta}\Delta_{AC} \quad . \tag{2.12}$$

The modification to the force, caused by the fact that the atom is in movement with velocity $\mathbf{v}$, only consists in considering the laser frequency as seen by the atom. The Doppler effect modifies the laser frequency according to: $\omega_L' = \omega_L$-kv, $\delta'=\delta$-kv. Let us consider the situation in which the atoms interact with two counterpropagating plane waves. In this case, by Taylor expanding the radiation pressure force for the two laser fields at small velocity, one gets:

$$\mathbf{F} = -\alpha\mathbf{v} \quad . \tag{2.13}$$

In the case of low saturation, the contributions from the two plane waves can be added independently and the value of the friction coefficient is:

$$\alpha = -\hbar k^2 s\frac{2\delta\Gamma}{\delta^2+\Gamma^2/4} \quad . \tag{2.14}$$

If $\delta < 0$, this force causes dissipation. The velocity range over which the Taylor expansion remains valid (velocity capture range) is given by v$< \Gamma/k$, that is satisfied if the semi-classical picture is applicable.

Spontaneous emission does not change the mean velocity, but can change the averaged square velocity by causing fluctuations. Fluctuations are described by a random walk in momentum space, expressed by

$$\langle p^2 \rangle(t) = 2D_p t \quad . \tag{2.15}$$

By the fluctuation-dissipation theorem, the limit temperature reachable by laser cooling is as follows

$$k_B T = \frac{D_p}{\alpha} \quad . \tag{2.16}$$

The calculation of the diffusion constant for a two-level system gives $\mathrm{D}_p = \hbar^2 k^2 \Gamma$s. This cooling scheme is called an "optical molasses"[24] and is applicable also in 3D. The temperature one gets for a two level atom is called Doppler temperature. It is independent of the laser power and it is minimum for $\delta = -\Gamma/2$, for which its value is given by:

$$k_B T_D = \frac{\hbar \Gamma}{2} \quad . \tag{2.17}$$

For the D2 transition used for cooling potassium $T_D \simeq 145\ \mu$K.

2.1.2 Sub-Doppler cooling

Cooling below the Doppler temperature is possible for multilevel atoms in presence of a non homogeneous polarization of the light field[25]. To get some insight, we can consider the electric field generated in a common experimental situation. Let us take two counter-propagating laser fields of opposite circular polarization (σ_- for the beam propagating along z and σ_+ for the one propagating in the opposite direction). The resulting electric field is always linearly polarized with the polarization axis that rotates in space around the z axis describing an helix with step λ. If an atom moves

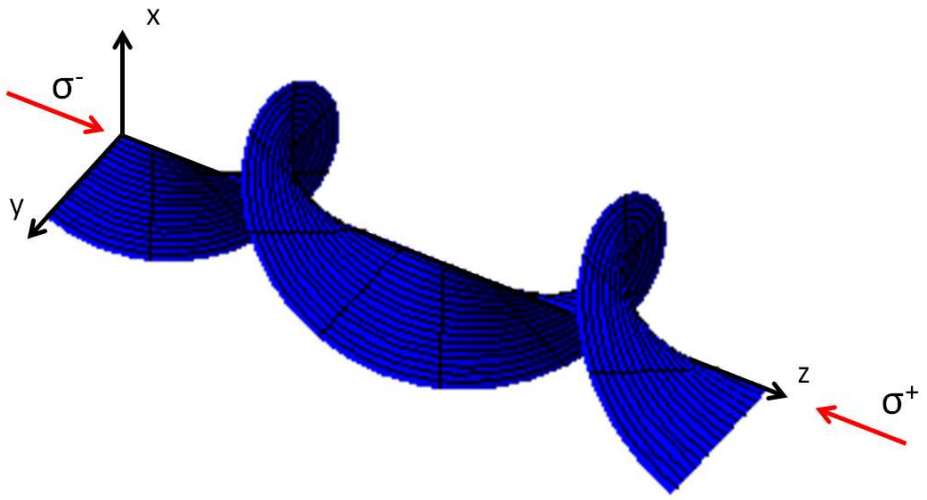

Figure 2.1: Polarization pattern produced by the laser configuration described in the text, the resulting electric field has linear polarization, the polarization axis describes an helix with step λ

along z it will therefore see the light polarization rotated by an angle kz.

The simpler transition exhibiting sub-Doppler cooling in this situation is a $J = 1 \rightarrow J' = 2$ transition. If we take as the quantization axis z, and we analyze the situation for an atom at rest at in a given position, for which the polarization of the light is $\widehat{x}$, it is possible to calculate the light shifts and the populations of the different ground state sub-levels. The result is, of course, symmetric for $m_F = +1$ and $m_F = -1$. If we repeat the analysis for an atom at rest in another position and with a different polarization of the light, nothing will change. So the light shifts and the populations in the ground state are independent of position for an atom at rest. If we now consider an atom moving in such a laser configuration with velocity v along the z axis, it is clear that the atom, in its rest frame, is in the presence of a varying polarization. The question arises whether it is able to follow the variation

during its motion or not.

We will work in a regime of velocity such that $kv \ll \Gamma$ in order to neglect the Doppler effect on detuning. The simplest approach is to describe the system in a rotating reference frame in which the laser polarization is constant. In this reference frame, a non inertial term is added to the Hamiltonian

$$V_{rot} = kvJ_z \quad . \tag{2.18}$$

This term rises the energy of the $m_F = +1$ state and lowers the energy of the $m_F = -1$, causing an imbalance in the populations of these two levels due to optical pumping processes. To calculate such imbalance one has to solve the OBE of the system. To have an estimation of the imbalance, we can consider the coherent Raman process that couples the $m_F = 1$ state to the $m_F = -1$ through absorption of a photon from the σ_- beam and re-emission into the σ_+ one (see Fig.2.2). We

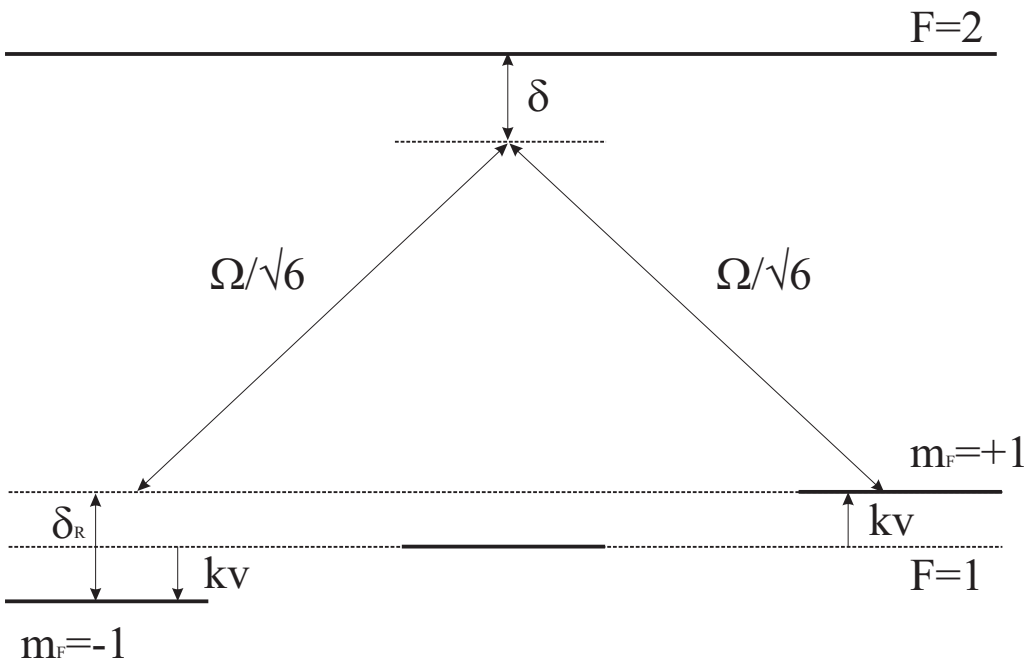

Figure 2.2: Scheme of the Raman coupling described in the text.

consider this process because it is Doppler free; so it is likely to exhibit a velocity

dependence even for $kv \ll \Gamma$. We can restrict the analysis to the two levels coupled by the Raman transition and describe the process on the Bloch sphere. The effective Rabi frequency of the Raman coupling is

$$\Omega_R = \frac{\Omega^2/6}{\delta} \quad , \tag{2.19}$$

the effective detuning of the Raman transition is

$$\delta_R = 2kv \quad . \tag{2.20}$$

The situation is the one depicted in Fig.2.3. For $v = 0$ there is no evolution, and the populations remain balanced. The introduction of a Raman detuning by the atomic velocity gives rise to a Rabi oscillation around the combined axis. On average and for small angles the population imbalance p will be

$$p \approx \frac{\delta_R}{\Omega_R} = \frac{2kv\delta}{\Omega^2} \tag{2.21}$$

in favor of the m_F=-1 state for positive δ. It is easy to see that, for increasing Raman detuning, the imbalance reaches a maximum for $kv_c \approx \Omega^2/\delta$; this defines the velocity capture range of sub-Doppler cooling. The force generated by the population imbalance is simply the radiation pressure force times p (the σ_- beam is pointing towards the velocity).

$$F_{SD} \approx \hbar k \frac{\Gamma}{2} sp \approx \frac{\hbar k^2 \delta \Gamma}{\delta^2 + \Gamma^2/4} v \tag{2.22}$$

which gives, for the friction coefficient at large detuning:

$$\alpha_{SD} \approx -\hbar k^2 \frac{\Gamma}{\delta} \quad . \tag{2.23}$$

Remarkably this is independent of laser power. The pre-factor on the above estimation and possible deviations from this behavior at small detuning will depend on the particular level scheme that one is dealing with. It is easy to see that the population imbalance of the extreme levels grows according to the degeneracy of the ground

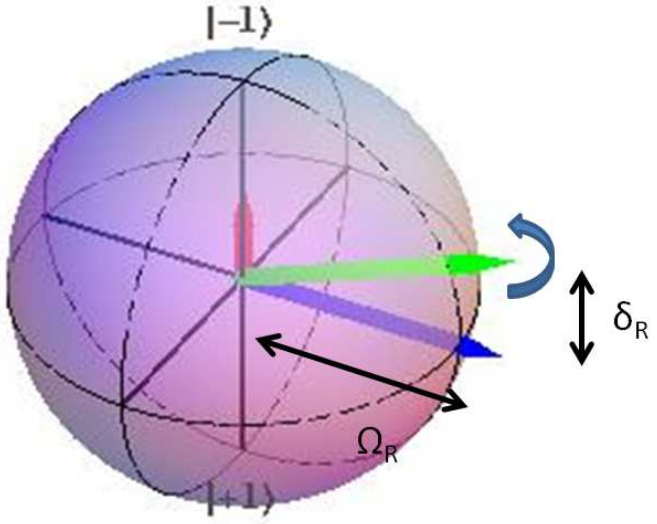

Figure 2.3: Bloch sphere representation of the effect of the Raman coupling. The situation in which Ω_R (and since δ) is positive is shown, in this case, on average there are more atoms in the $m_F = -1$ level. The initial situation is supposed to be with the representative Bloch vector aligned with Ω_R for simplicity.

state $\delta_R \propto m$, with m the magnetic quantum number. So an higher degeneracy implies higher friction. For large detuning, $\delta \gg \Gamma$, using the same diffusion constant in momentum space used for the Doppler case, one gets:

$$k_B T_{SD} = \frac{D_p}{\alpha_{SD}} \approx \frac{\hbar\Omega^2}{\delta} \approx k_B T_D \frac{I}{I_s}\frac{\Gamma}{\delta} \tag{2.24}$$

in which we made use of $\Omega = \frac{\Gamma}{2}\sqrt{\frac{I}{2I_s}}$. I is the intensity of the light wave and I_s is the saturation intensity.

From the above expression one sees that, using this method it is possible to reach very low temperatures. For $\delta \gg \Gamma$ and $I \ll I_s$, the temperature can be much lower than the Doppler temperature. The limit of the cooling method is reached when the thermal velocity spread exceeds the velocity capture range of the process. At that point the Doppler cooling becomes dominant and the temperature grows eventually

reaching T_D. For the limit temperature:

$$k_B T_{lim} \approx \frac{1}{2} m v_c^2 \approx \frac{m}{2\hbar^2 k^2} \frac{\hbar^2 \Omega^4}{\delta^2} \approx \frac{k_B^2 T_{lim}^2}{E_R} \quad ; \tag{2.25}$$

this implies

$$k_B T_{lim} \approx E_R \quad . \tag{2.26}$$

In conclusion, this cooling method is limited only by the recoil energy, which for potassium is 0.4 μK. The prefactor on the expression for the limit temperature was calculated using Monte Carlo simulations and was found to be in the range of 10-40, depending on the actual level scheme[26].

2.1.3 Evaporative cooling

In order to reach even lower temperatures, an evaporative cooling scheme is used by which the higher energy atoms are selectively extracted from the trap. The atoms with higher energy are populating the low density tails of the cloud. If they are removed slowly, on a time scale which is longer than the time the cloud needs to reach thermal equilibrium τ_{eq}, the evaporation determines cooling and the process can be sustained up to the condensation point. Since only a few collisions are sufficient to equilibrate the thermal distribution, we can approximate $\tau_{eq} \simeq \tau_{coll} = (n\sigma v)^{-1}$, in which σ is the cross section for elastic collisions between atoms, n is the atomic density, and v the typical atomic velocity. This is indeed the same process that happens everyday when a cup of coffee cools down.

In cold atoms this process is usually realized in magnetic or optical traps. In a magnetic trap, the spatial variation of the magnetic field across the trap offers an elegant way to evaporate the cloud. Using a radio frequency transition, the trapped state can be coupled to an untrapped one. The frequency can be chosen in such a way that only atoms with a given potential energy will be resonant. This scheme

removes all atoms on a "resonance surface" (three dimensional evaporation). The radio frequency gets progressively reduced up to the condensation point.

In an optical trap instead, a focused laser beam, tuned on the red of the atomic transition, is used for trapping by the dipole potential. The potential experienced by the atoms is given by:

$$U(\mathbf{x}) = \alpha(\omega_L) I(\mathbf{x}) = \alpha(\omega_L) \frac{I_0}{1 - \frac{z^2}{z_0^2}} e^{-\frac{2r^2}{W_0^2}} \tag{2.27}$$

where $\alpha(\omega_L)$ is the atomic polarizability at the laser frequency, I_0 is the intensity at the focal point, z and r are coordinates along and transverse to the laser beam axis respectively, W_0 is the beam waist, and $z_0 = \pi W_0^2/\lambda_L$ is the Rayleigh range. This potential yields a finite depth given by $U_0 = \alpha(\omega_L) I_0$. Atoms with an energy larger than U_0 cannot be confined by the potential and they will leave the trap due to gravity. Atoms are therefore lost on a preferential direction (one dimensional evaporation). The evaporation in this case is performed by progressively reducing the laser power and therefore the trap depth. Differently from the magnetic case, for dipole traps, during evaporation the trap frequencies are also reduced. This can be a problem since it causes the collision rate to decrease in typical situations.

The first quantity that characterizes the evaporation is the truncation parameter $\eta = U_0/(k_B T)$. A low η inhibits thermalization, while a high one results in slow evaporation, that can in turn lead to losses. The evaporation rate, in fact, is determined by the truncation parameter. Every time a collision takes place, the probability to evaporate a new atom is given by the Boltzmann factor $e^{-\eta}$. Therefore for the evaporation rate:

$$\Gamma_{ev} = \Gamma_{el} e^{-\eta} \tag{2.28}$$

with

$$\Gamma_{el} = \frac{1}{\tau_{coll}} = n\sigma v \tag{2.29}$$

the rate of elastic collisions. Two different time scales are driving the evaporation

ramp, determining the optimum value of the truncation parameter. The first one is the thermalization time τ_{eq} that is the inverse of the elastic collision rate. The second time scale is determined by losses and heating in the system; these can be of various nature: collisions with the background gas, two-body or three-body collisions, technical noise on the trapping potential, etcetera. They all contribute to an inelastic rate Γ_{in}. The evaporation is efficient when the evaporation rate is, on the one hand, lower than the elastic collision rate (necessary condition for the gas to be able to equilibrate), and on the other, higher than the inelastic collision rate (condition this for the evaporation to be the dominant loss process). This means that a lower η is favorable when we are in presence of strong inelastic rates. There is anyway a limit. In fact it can be proven that, for a harmonic trap, an $\eta < 3$ leads to a decreasing phase space density during the evaporation[27].

The efficiency of the evaporation process is measured by the χ parameter, which is defined by:

$$\chi = \frac{\log \rho_f/\rho_i}{\log N_i/N_f} \tag{2.30}$$

in which $\rho_{i(f)}$ is the initial (final) phase space density and $N_{i(f)}$ is the initial (final) number of atoms.

2.2 Bose-Einstein condensation

Bose-Einstein condensation is a phase transition occurring when the thermal De Broglie wavelength λ_{DB} of the particles

$$\lambda_{DB} = \frac{h}{\sqrt{2\pi m k_B T}} \tag{2.31}$$

becomes comparable with their inter-atomic distance[28, 29]. In this regime the wave nature of atoms becomes dominant and quantum effects are important for the macroscopic behavior of the system. In terms of the phase space density

$$\rho = n\lambda_{DB}^3 \tag{2.32}$$

the phase transition takes place when ρ=2.612.

For a normal gas at room temperature and atmospheric pressure the De Broglie wavelength of the particles is smaller than the atomic radius, the phase space density of the gas is around 10^{-7}. From this point, it is possible to increase the phase space density either by increasing the density or decreasing the temperature. However, as can be seen from Fig.2.4, the BEC transition happens in a region of the phase diagram in which the equilibrium state of matter is a solid[1].

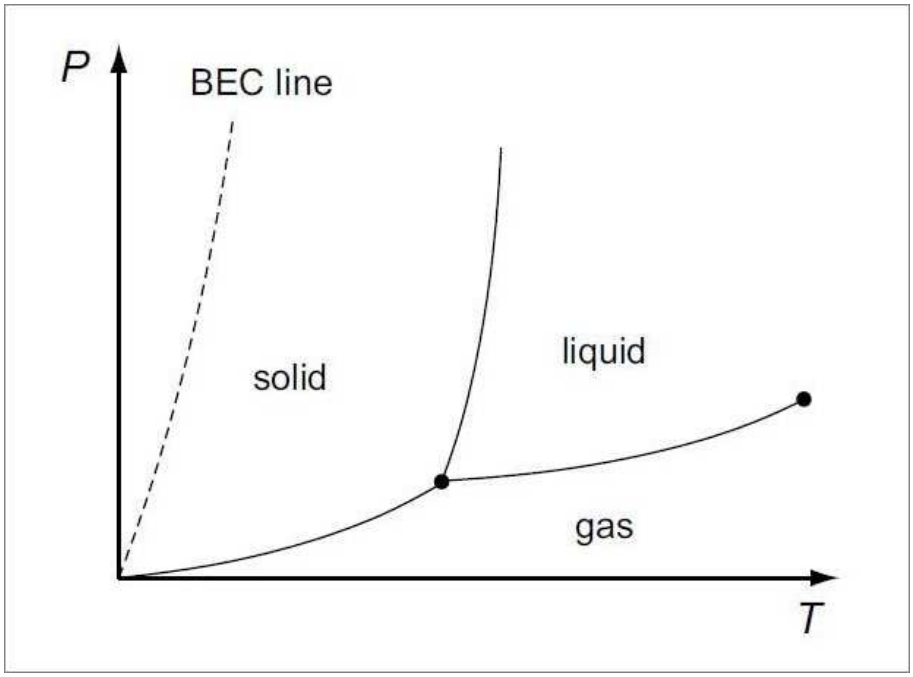

Figure 2.4: Phase diagram of a typical bosonic element. The BEC region is dashed since the true equilibrium state of the system is the solid state.

This means that all BECs are metastable, the solid state being the true ground state of the system. The first processes that leads to the sample's solidification are the ones in which three atoms collide, two of them form a molecule and the third one ensures conservation of momentum. The binding energy of the molecule gets converted into kinetic energy, leading to the loss of all three atoms from the trap

[1]the only element that makes exception in this sense is helium

(three body loss). If the sample is dilute the probability to find three atoms, close enough to determine a three body loss, can be negligible and the lifetime of the BEC can be long. To be quantitative, three body losses in a gas are described by the formula

$$\dot{n} = -K_3 n^3 \tag{2.33}$$

The minimum value of K_3 for ^{39}K is 10^{-29} cm^6/s. For a normal BEC at a density of 10^{14} atoms/cm^3, this equation predicts a 10 s lifetime for the condensate. Such density is 5 orders of magnitude lower than the density of air at atmospheric pressure.

2.2.1 BEC of weakly interacting atoms in a harmonic trap

In experiments, we deal with interacting samples of atoms trapped by inhomogeneous external potentials. To describe the system in this situation the so-called Gross-Pitaevskii equation[30] (GPE) is required. In second quantization, the many-body Hamiltonian operator describing a system of N bosons in an external potential V_{ext} is given by

$$\widehat{H} = \int d\mathbf{x}\widehat{\Psi}^\dagger(\mathbf{x}) \left[-\frac{\hbar^2\nabla^2}{2m} + V_{ext}(\mathbf{x})\right] \widehat{\Psi}(\mathbf{x}) + \frac{1}{2}\int\int d\mathbf{x}d\mathbf{x}'\widehat{\Psi}^\dagger(\mathbf{x})\widehat{\Psi}^\dagger(\mathbf{x}')V_{int}(\mathbf{x},\mathbf{x}')\widehat{\Psi}(\mathbf{x})\widehat{\Psi}(\mathbf{x}') \quad . \tag{2.34}$$

In the case of ultra-cold bosons, the interaction potential can be greatly simplified. Every collision channel but the s-wave is in fact strongly inhibited due to the very low collisional energy (see Sec. 2.3). When only s-wave scattering is present, the details of the interaction potential are not important anymore, therefore it can be substituted by a pseudo-potential with the same s-wave scattering amplitude

$$V_{int}(|\mathbf{x}-\mathbf{x}'|) \to \frac{4\pi\hbar^2 a}{m}\delta(\mathbf{x}-\mathbf{x}') \quad . \tag{2.35}$$

The parameter a is the s-wave scattering length which is an experimentally determined parameter.

Even with this simplification, the solution of the Schrödinger equation for a system of typically 10^5 atoms is a numerically impracticable task. To further simplify the problem, we can make use of our knowledge of the ground state of the system. The ground state is the condensate, which is characterized by a macroscopic occupation of a single quantum state. In this case, the fluctuations on the wave function amplitude can be neglected and the amplitude itself can be substituted by a c-number (mean field approximation)[31]:

$$\widehat{\Psi}(\mathbf{x}) = \widehat{b}_0\Psi_0(\mathbf{x}) + \delta\widehat{\Psi}(\mathbf{x}) \approx \sqrt{N_0}\Psi_0(\mathbf{x}) \quad . \tag{2.36}$$

Here $\widehat{b}_0$ is the destruction operator of the ground state, $\Psi_0(\mathbf{x})$ is the condensate wave-function, and $\delta\widehat{\Psi}(\mathbf{x})$ represent excitations of the system, which are neglected. N_0 is the number of atoms in the ground state. By substituting this ansatz for the wave-function back into the Hamiltonian and writing the equation of motion, we get the GPE

$$i\hbar\dot{\Psi}_0(\mathbf{x},t) = \left[-\frac{\hbar^2\nabla^2}{2m} + V_{ext}(\mathbf{x}) + \frac{4\pi\hbar^2 a}{m}|\Psi_0(\mathbf{x},t)|^2\right]\Psi_0(\mathbf{x},t) \quad . \tag{2.37}$$

From the mathematical point of view the GPE is a single particle Schrödinger equation with a non-linear term accounting for interactions. The stationary solution to this equation is calculated by replacing $\Psi_0(\mathbf{x},t) = e^{-i\mu t/\hbar}\Psi_0(\mathbf{x})$

$$\mu\Psi_0(\mathbf{x}) = \left[-\frac{\hbar^2\nabla^2}{2m} + V_{ext} + \frac{4\pi\hbar^2 a}{m}|\Psi_0(\mathbf{x})|^2\right]\Psi_0(\mathbf{x}) \tag{2.38}$$

the parameter μ is the chemical potential of the condensate.

This equation has two limit behaviors: for very low interaction strengths the non linear term can be neglected and the GPE becomes simply the Schrödinger equation for a particle in the external potential V_{ext}. In this case the condensate wavefunction is nothing but the ground state wavefunction of a single particle in the external potential. If the potential is harmonic with angular frequencies $\omega_x, \omega_y, \omega_z$

$$\Psi_0(x,y,z) = \left(\frac{m\overline{\omega}}{\pi\hbar}\right)^{3/4} e^{-\frac{m}{2\hbar}(\omega_x x^2 + \omega_y y^2 + \omega_z z^2)} \tag{2.39}$$

here $\overline{\omega}$ is the geometric average of the three angular frequencies. The chemical potential in this case is simply the harmonic oscillator ground state energy $\mu = \frac{\hbar(\omega_x+\omega_y+\omega_z)}{2}$.

The other limit case is the one in which repulsive interactions are dominating over the kinetic term. In this case, which is the case for typical BECs, we can neglect the kinetic term in the GPE applying the so-called Thomas-Fermi approximation. In this case, the GPE becomes a simple algebraic equation for the condensate density, whose solution gives an inverted parabola profile of the condensate

$$n(x,y,z) = |\Psi_0(x,y,z)|^2 = \frac{m}{4\pi\hbar^2 a}(\mu - V_{ext}(x,y,z))\theta(\mu - V_{ext}(x,y,z)) \quad . \tag{2.40}$$

The chemical potential is obtained by the condition that the integral of n gives the total atom number and it is given by

$$\mu = \frac{\hbar\overline{\omega}}{2}\left(\frac{15Na}{\bar{l}_{ho}}\right)^{2/5} \quad , \tag{2.41}$$

where l_{ho} is the harmonic oscillator length. For the same potential considered in the non interacting case, the density at the center and the radii of the cloud can be calculated

$$n_0 = \frac{m}{4\pi\hbar^2 a}\mu \tag{2.42}$$

$$R_i = \sqrt{\frac{2\mu}{m\omega_i^2}} \tag{2.43}$$

for $i = x, y, z$. The condition for the interaction energy to be larger than the kinetic energy can be rephrased in $\mu \gg \hbar\omega/2$[32]. This is true if $Na \gg l_{ho}$. The oscillator length l_{ho} for a typical trapping frequency of 100 Hz is 1.6 μm. For a condensate of 10^5 atoms, Na become 10 times larger than l_{ho} for a scattering length of only 3 a_0, where a_0 is the Bohr radius. Since the typical values of the scattering length are of the order of one hundred a_0, the Thomas-Fermi approximation is typically very well justified.

2.3 Tuning the interactions

Interactions among neutral atoms are typically due, on the one hand, to Fermi pressure at short distances which prevents the nuclei to come too close to each other, and on the other, to Van Der Waals attraction at large distances, which fall off with the interaction distance r as r^{-6}. To treat collisions I will make use of some well known results from scattering theory[33]. Before going into details, let us consider the typical length scales in the system. The three relevant distances for the collisional physics of the gas are: the inter-particle distance $n^{-1/3}$, the range of action of the interaction potential r_0, and the De Broglie wavelength λ_{DB}. Since we deal with dilute gases $n^{-1/3} > r_0$, is typically valid. At high temperature, the De Broglie wavelength is shorter than r_0 . Decreasing the temperature, λ_{DB} becomes of the same order, or larger, than r_0. Finally, for even lower temperatures, it can reach $n^{-1/3}$ leading to condensation. In the intermediate regime, $r_0 < \lambda_{DB} < n^{-1/3}$, the gas is still thermal but the wave nature of the particles influences the collisional properties. A quantum-mechanical treatment of the collisions is therefore required. To have an idea, if we consider an r_0 of around 2-3 nm, the De Broglie wavelength is larger than r_0 for temperatures lower than 10 mK.

Let us consider the collision of two atoms having the same mass m. The full Hamiltonian reads

$$H = \frac{|\mathbf{p}_1|^2}{2m} + \frac{|\mathbf{p}_2|^2}{2m} + V(|\mathbf{r}_1 - \mathbf{r}_2|) \quad . \tag{2.44}$$

The interaction potential is supposed to have central symmetry, since we will always deal with alkali atoms with one unpaired electron in the external s orbital. We can introduce the center of mass and relative coordinates, in which the Hamiltonian is re-written as

$$H = \frac{|\mathbf{p}_{CM}|^2}{4m} + \frac{|\mathbf{p}|^2}{m} + V(|\mathbf{r}|) \tag{2.45}$$

the following notations are used

$$\mathbf{p}_1 + \mathbf{p}_2 = \mathbf{p}_{CM} = \hbar\mathbf{k}_{CM}, \qquad \frac{\mathbf{p}_1 - \mathbf{p}_2}{2} = \mathbf{p} = \hbar\mathbf{k}, \tag{2.46}$$

$$\frac{\mathbf{r}_1 + \mathbf{r}_2}{2} = \mathbf{r}_{CM}, \qquad \mathbf{r}_1 - \mathbf{r}_2 = \mathbf{r} \quad . \tag{2.47}$$

It is a known result of scattering theory that for the system wave-function after the collision the following limit behavior is valid

$$\Psi(\mathbf{r}_1, \mathbf{r}_2) \rightarrow_{\mathbf{r}\to\infty} e^{i\mathbf{k}_{CM}\cdot\mathbf{r}_{CM}} \left(e^{i\mathbf{k}\cdot\mathbf{r}} + f_k(\theta)\frac{e^{ik|\mathbf{r}|}}{|\mathbf{r}|} \right) \quad . \tag{2.48}$$

where θ is the axial angle between $\mathbf{r}$ and $\mathbf{k}$. This equation consists of two terms in the relative reference frame: the first one describes the two waves passing away from each other (transmission), while the second one describes a spherical wave originated from the collision point (diffusion). The quantity $f(\theta)$ sets the strength of the diffusion with respect to the transmission and it can only depend on the axial angle because of the cylindrical symmetry of the problem.

The above expression needs to be symmetrized (bosons) or anti-symmetrized (fermions) if we are dealing with identical particles. The only term that changes when exchanging the two particles is $f(\theta)$. It is easy to realize that the two events depicted in Fig.2.5 are indistinguishable for identical particles. The symmetrization,

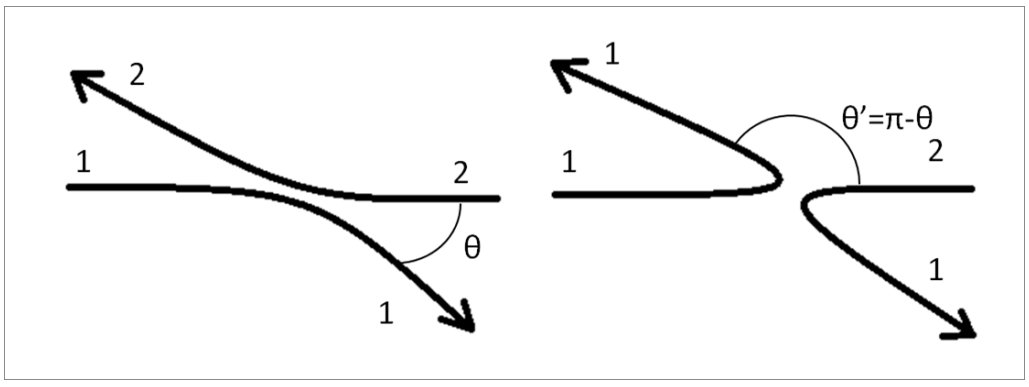

Figure 2.5: The two collisional events in this picture are indistinguishable for identical particles. Their amplitude probability has therefore to be symmetrized.

therefore, consists simply in the replacement

$$f(\theta) \rightarrow f(\theta) \pm f(\pi - \theta) \tag{2.49}$$

with the plus sign for bosons and the minus sign for fermions. The total cross section for the collision process can be found to be

$$\sigma_{tot} = 2\pi \int_0^{\frac{\pi}{2}} |f(\theta) \pm f(\pi - \theta)|^2 \sin(\theta) d\theta \quad . \tag{2.50}$$

Since the interaction potential is centrally symmetric we can describe the collision in term of partial waves. The symmetrization causes the cancellation of the odd waves for bosons and of the even ones for fermions

$$\sigma_{tot} = \frac{8\pi}{k^2} \sum_{2l} (2l+1) \sin^2(\delta_l(k)) \qquad (bosons) \tag{2.51}$$

$$\sigma_{tot} = \frac{8\pi}{k^2} \sum_{2l+1} (2l+1) \sin^2(\delta_l(k)) \qquad (fermions) \tag{2.52}$$

The parameters $\delta_l(k)$ are the partial wave's phases and they carry information about the interaction potential. The equation for the radial wave function $u_{k,l}$ is

$$u''_{k,l}(r) + \left[k^2 + \frac{l(l+1)}{r^2} + V(r) \right] u_{k,l}(r) = 0 \quad . \tag{2.53}$$

This equation is the same as the one describing the 1D motion of a particle moving in the effective potential $V_{eff}(r) = \frac{l(l+1)}{r^2} + V(r)$. The potential $V(r)$ has a typical range of action of a few nm, while for larger distances the repulsive centrifugal term dominates.

If $V(r) = 0$, the shortest distance a particle with low energy can reach is $r_l = \frac{\sqrt{l(l+1)}}{k}$, which is of the order of the De Broglie wavelength ($\lambda_{DB} \approx 1/k$). At the condensation point, the De Broglie wavelength can take typical values of about 1 μm; therefore, unless $l = 0$, the potential is unreachable by the particles. This phenomenon can be visualized in terms of a centrifugal barrier given by the term $\frac{l(l+1)}{r^2}$, whose height can be a few hundreds of μK. For temperatures lower than the

centrifugal barrier's height, the only partial wave contributing to the scattering is the s-wave. Because of this and of the symmetrization rules, it follows that ultra-cold fermions are practically non-interacting and that the cross section for bosons is

$$\sigma_{tot} = \frac{8\pi}{k^2} \sin^2(\delta_0(k)) \quad . \tag{2.54}$$

At this point we can define the s-wave scattering length to be

$$a = \lim_{k \to 0} -\frac{\delta_0(k)}{k} \quad , \tag{2.55}$$

such that

$$\lim_{k \to 0} \sigma_{tot} = 8\pi a^2 \quad . \tag{2.56}$$

The only parameter that we need to know, in order to characterize the collision at low energy is thus a.

2.3.1 Square well potential

To get some insight on the scattering length, we can look at the simple case in which the interaction potential is a square well. For this potential, the scattering problem is easily solvable analytically.

$$\begin{cases} V = -V_0 & 0 < r < r_0 \\ V = 0 & r_0 < r < R \\ V = \infty & r > R \end{cases} \tag{2.57}$$

here I also inserted a finite system size R, which is supposed to be larger than any other length scale of the problem.

Let us start by considering the continuum states for $E > 0$ and $l = 0$. The equation for the radial wave function can be solved in the different zones, giving

$$\begin{cases} u_0 = A \sin(k_+ r) & 0 < r < r_0 \\ u_0 = B \sin(kr + \delta_0) & r_0 < r < R \\ u_0 = 0 & r > R \end{cases} \tag{2.58}$$

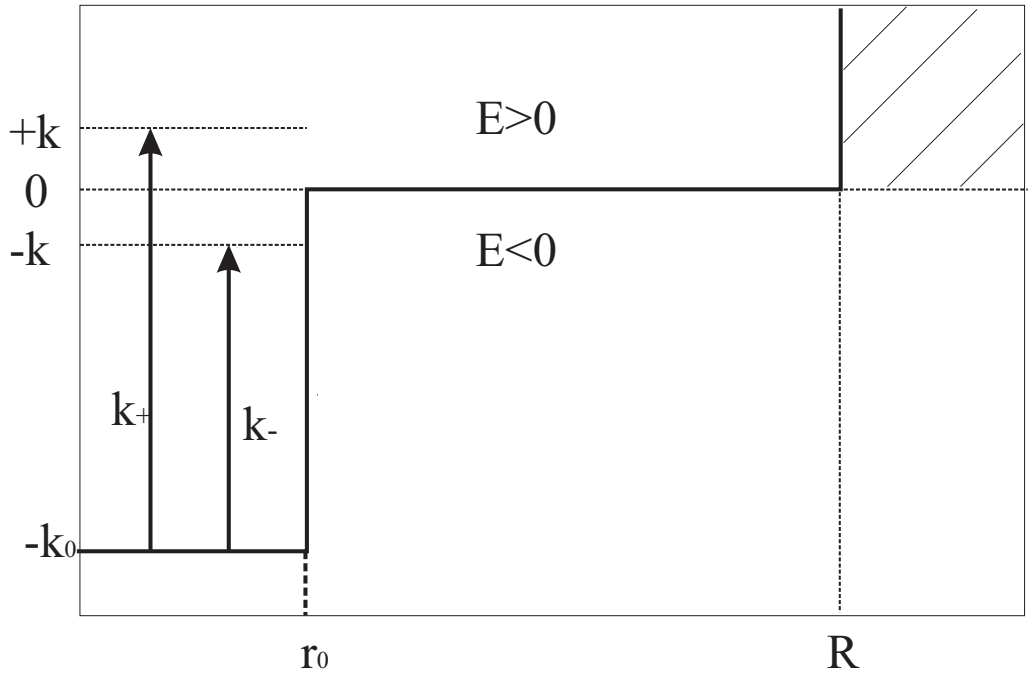

Figure 2.6: Square well potential with the related notations

where $k = \sqrt{2mE}/\hbar$, $k_0 = \sqrt{2mV_0}/\hbar$, and $k_+^2 = k_0^2 + k^2$. By imposing the continuity of the wavefunction in R, we get

$$\sin(kR - \delta_0) \rightarrow_{k\rightarrow 0} \sin(k(R-a)) = 0 \quad . \tag{2.59}$$

The limit follows from the very definition of a. This implies the quantization of k by

$$k_n = \frac{n\pi}{R-a} \quad . \tag{2.60}$$

If the interaction potential was not present, the previous expression with $a = 0$ would have given the energy of one particle in the box with size R. The presence of the second particle changes the energy, increasing it for positive a (repulsion) and decreasing it for negative a (attraction). Now we impose the continuity of the logarithmic derivative of the wave-function at r_0:

$$k \cot(kr_0 + \delta_0) = k_+ \cot(k_+ r_0) \quad . \tag{2.61}$$

Solving for $k \approx 0$, the following equation can be found for the behavior of the phase δ_0 at non-zero energy[34]

$$\frac{\tan(\delta_0)}{k} \approx -a - \frac{1}{2}a^2 r_e k^2 \quad . \tag{2.62}$$

The parameter r_e is the effective radius that, in the case of a square well potential, is approximately equal to r_0. Since the second term has a fixed sign, when the scattering length is found to be negative and small, a zero in the phase δ_0 is predicted for low energy [2]. This is the so-called Ramsauer-Townsend effect[35], which represents a serious issue when evaporatively cooling some atomic species (^{85}Rb and ^{39}K are two examples). Indeed, when the typical energy of the cloud approaches the Ramsauer-Townsend minimum, the system is no more able to thermalize and the evaporation becomes inefficient or stops completely. Let us go back to the continuity equation 2.61, for $k = 0$ it reads

$$\frac{1}{r_0 - a} = k_0 \cot(k_0 r_0) \quad . \tag{2.63}$$

Solving it for a, we get

$$a = r_0 - \frac{\tan(k_0 r_0)}{k_0} \quad . \tag{2.64}$$

A plot of this formula is on Fig.2.7: a divergence in the scattering length is predicted each time $k_0 r_0 = \frac{\pi}{2} + n\pi$.

To get some more insight we can consider the same problem but now for a very shallow bound state ($E < 0$). The solution to the radial wave equation, in this case, is:

$$\begin{cases} u_0 = A \sin(k_- r) & 0 < r < r_0 \\ u_0 = B e^{-kr} & r_0 < r < R \\ u_0 = 0 & r > R \quad . \end{cases}$$

[2] Actually, the expansion of the phase in series of k is no more appropriate at the position of the zero. Nevertheless, more accurate calculations still predicts its presence. Its position cannot be found just by the first two terms in the series.

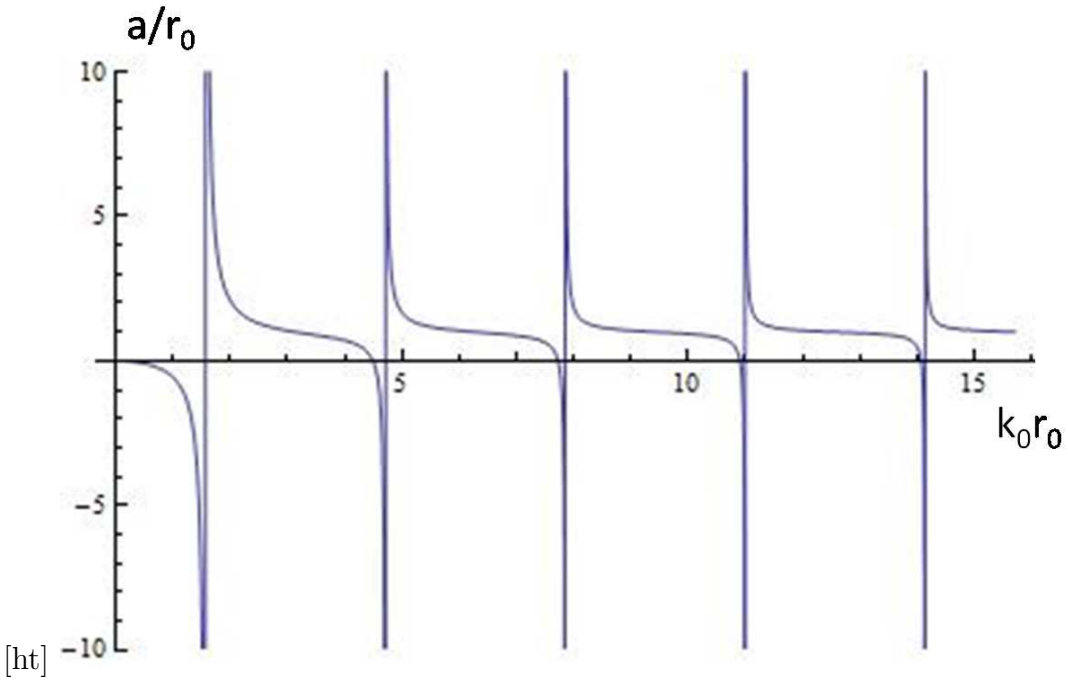

[ht]

Figure 2.7: Scattering length in units of r_0 as a function of the parameter $k_0 r_0$. A resonant behavior is apparent every time a new bound state is added to the potential.

The continuity of the logarithmic derivative of the wavefunction in r_0 leads to

$$-k = k_0 \cot(k_0 r_0) \quad . \tag{2.65}$$

In the limit of a very shallow bound state, $k \to 0$, the condition of Eq.2.65 has to connect to the one for $E > 0$, Eq.2.63. This is only possible if a diverges. This means that, each time a new bound state is added to the potential, the scattering length shows a divergence. When the bound state is about to show up, a is negative and large. When instead it is just appeared, a is positive and large.

2.3.2 Fano-Feshbach resonances

The simple picture, given by the analysis of the square well potential, applies also in practical situations, in which many molecular adiabatic potentials are present. For real cases, however, an analytical solution is usually not found. A resonant

behavior is found in the scattering length any time a new bound state is added to the interatomic potential. In practice, a new bound state can be added to the potential exploiting the presence of many different interatoimic potential curves due to collision into different spin channels. For large distances, those curves connect to the sum of the energies of the free colliding atoms. Such energies have a magnetic component that can be changed by applying an external magnetic field. Doing so, two of these potential curves can be shifted in energy with respect to each other (see Fig.2.8). Due to residual interactions (spin orbit couplings, dipolar interactions, etc.), the two potential curves are not completely independent. For this reason, whenever a bound state of one of the potentials is close to the dissociation threshold of the potential in which the collision takes place, the scattering length shows a resonant behavior.

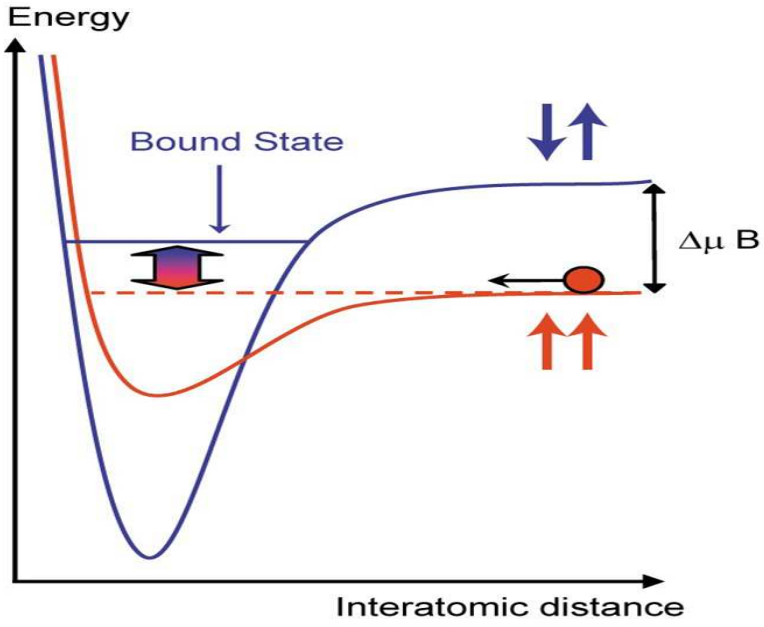

Figure 2.8: Sketch of the basic principle of a Feshbach resonance.

Those resonances are named Fano-Feshbach resonances and they are used in experiments to have control over the inter-atomic interaction, simply applying a uniform magnetic field on the atomic sample. Usually, the typical magnetic noise in

the lab can be of the order of a few tens of mG and, therefore, tuning the interactions on sharp resonances can be challenging. The resonances, in exceptional situations (experimentally identified for ^{39}K, ^{6}Li, ^{7}Li, Na, Cs), can be as wide as 10-100 G and they can take place at easily accessible values of the magnetic field. To understand what can lead to wide resonances, we can consider the coupling between the two states involved in the process. The initial state is a continuum state, which has a typical extension given by the De Broglie wavelength. We consider its coupling with a bound state of a molecular potential, whose wavefunction is typically contained within the range of action of the interaction potential. Since $\lambda_{DB} \gg r_0$ for the typical temperatures of our samples, the overlap between the two wave-functions (Frank-Condon factor) is typically very small. Anyway a significant tunneling of the wave function outside the interaction range can be present for the case of very loosely bound states. This can increase the coupling between the states and therefore gives rise to wide resonances.

Close to the resonance, the scattering length as a function of the applied magnetic field, is given by the formula

$$a = a_{bg}\left(1 - \frac{\Delta}{B - B_0}\right) \tag{2.66}$$

a_{bg} is the scattering length value far from the resonance, B_0 is the resonance position and Δ is the resonance width, which is defined as the distance between the resonance and the zero crossing of the scattering length. The ability to tune the scattering length to zero, and therefore to create a non interacting BEC, is measured by the quantity

$$\left.\frac{da}{dB}\right|_{a=0} = \frac{a_{bg}}{\Delta} \quad . \tag{2.67}$$

Therefore a small a_{bg} and a large Δ are desirable to get a high degree of tunability of the scattering length.

Chapter 3

Quantum interferometry

3.1 Two-mode atom interferometry

In this section is introduced the problem of a BEC in a double well potential in the two-mode approximation. It is also discussed its possible application in the field of atomic interferometry. We consider to have prepared a BEC in a harmonic trap and, by using some appropriate technique, we slice it in two halves by rising a potential barrier in the middle of it. If the barrier is high enough, the single particle Hamiltonian will have two low-energy levels which are close in energy and are separated from the other excited levels. The ground state will have a symmetric wave-function and the first excited level an anti-symmetric one.

The two-mode approximation consists in supposing that all other levels will have a very low population with respect to the two low-lying ones. This is valid if all the energy scales of the system (temperature, interaction energy, tunneling energy) are much lower than the separation from the other excited levels, separation that one which is of the order of the harmonic oscillator energy for the original trap. We note that this condition is much more stringent than the BEC transition, since usually at the transition $k_B T_c \gg \hbar\omega$. Given the two-mode approximation, the many-body

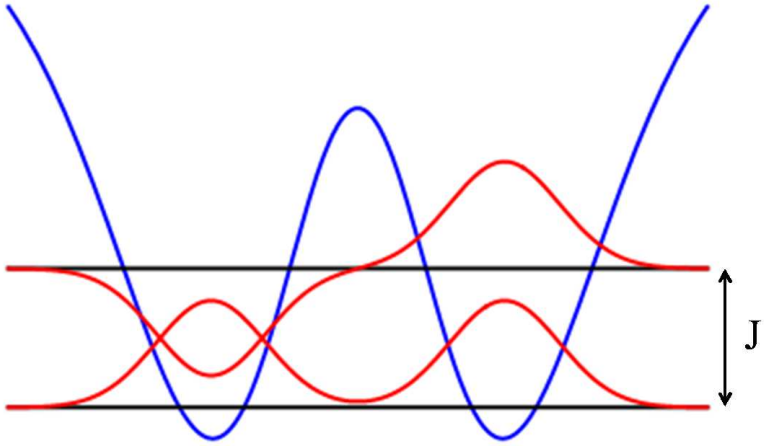

Figure 3.1: Sketch of the double well potential with its two low-lying eigenstates. Their energy difference is the single atom tunneling energy J.

wavefunction of the system can be described by using only the two low lying states

$$\widehat{\Psi} = \psi_g a_g + \psi_e a_e \tag{3.1}$$

here a_g (a_e) is the destruction operator for a particle in the ground (excited) state. We can now introduce the destruction operators of an atom into the left or right well localized wave-functions by

$$a_{l,r} = \frac{1}{\sqrt{2}}(a_g \pm a_e), \tag{3.2}$$

$$\psi_{l,r} = \frac{1}{\sqrt{2}}(\psi_g \pm \psi_e) \quad . \tag{3.3}$$

By plugging this form for the wavefunction into the Hamiltonian (Eq.2.34) the two-modes Hamiltonian is found

$$\widehat{H} = \frac{E_c}{4}(n_l(n_l-1) + n_r(n_r-1)) - \frac{E_J}{N}(a_l^+ a_r + a_r^+ a_l) \tag{3.4}$$

where $n_{l,r} = a_{l,r}^+ a_{l,r}$ are the number of atoms in the two sites and

$$E_c = \frac{8\pi\hbar^2 a}{m}\int |\psi_l, r|^4 d\mathbf{r} \tag{3.5}$$

$$E_J = N\int \psi_l^* \left(\frac{\hbar^2\nabla^2}{2m} - V(r)\right)\psi_r d\mathbf{r} \tag{3.6}$$

are the charging energy, proportional to the two-body interaction energy and the Josephson coupling energy, equal to N times the tunneling energy.

It is easy to see that the g, e basis is the natural one to diagonalize the tunneling term, since it contains only single particle operators. In the l, r basis, the interaction part is instead diagonal. An additional term is added to the Hamiltonian in the case in which the two wells are shifted in energy by an amount Δ, giving

$$\widehat{H} = \frac{E_c}{4}(n_l(n_l-1)+n_r(n_r-1)) - \frac{E_J}{N}(a_l^+ a_r + a_r^+ a_l) + \frac{\Delta}{2}(n_l - n_r) \tag{3.7}$$

for the complete Hamiltonian.

Let us focus on the case with no interaction ($E_c = 0$). In this case, if one prepares the BEC on the left side and if $\Delta = 0$, the system will undergo Rabi oscillations between the left and right well due to the tunneling term. The magnitude of the tunneling can be tuned by acting on the height of the barrier, so it is possible to stop the Rabi oscillations at any time. If we stop the oscillation, at a time for which the probability for the BEC to be on each of the two sides is 50 %, we realize a $\pi/2$ pulse or a 50-50 beam splitter for atoms. Let us now focus on the effect of the last term in the Hamiltonian. In the case in which both E_c and E_J are zero, the Δ term cannot change the populations on the two sides, since it is diagonal. Its only effect is to give a differential phase ϕ, which is increasing with time ($\phi = \frac{\Delta t}{\hbar}$), to the two parts of the wavefunction. An atomic interferometer is realized by a Mach-Zehnder scheme, composed by: a $\pi/2$ pulse, a phase accumulation, a second $\pi/2$ pulse and finally by the detection of the number of atoms on the two sides of the double-well. At the end of the sequence, the difference between the number of atoms on the two sides is given by

$$\langle n_l - n_r \rangle = n = \frac{N}{2}\sin(\phi) \tag{3.8}$$

in which N is the total number of atoms and it is supposed to be constant.

The measurement of the parameter ϕ is the goal of the interferometric measurement. Let us now estimate the sensitivity of the measurement. Given that one measures ϕ

m times independently, by applying error propagation formula, the following equation is found for the variance of ϕ:

$$\Delta\phi^2 = \frac{\Delta n^2}{m\left|\frac{dn}{d\phi}\right|^2} \quad . \tag{3.9}$$

Since we never used the interaction term, the atoms during the sequence are independent and the fluctuation on their relative number is supposed to be Poissonian $\Delta n^2 = \frac{N}{4}\sin^2(\phi)$. The result for the phase resolution is

$$\Delta\phi = \frac{1}{\sqrt{mN}} \quad , \tag{3.10}$$

which implies that, doing the experiment with N atoms, it is effectively as repeating N times the same measurement. This resolution is the best one achievable in non interacting interferometers and it is called the standard quantum limit (SQL)[36]. In the following section we will see how the picture changes by adding interactions.

3.1.1 Bloch sphere representation

By using the creation and destruction operators of the double well, it is possible to define three operators, given by

$$J_x = \frac{a_l^+ a_r + a_r^+ a_l}{2} \tag{3.11}$$

$$J_y = \frac{a_l^+ a_r - a_r^+ a_l}{2i} \tag{3.12}$$

$$J_z = \frac{a_l^+ a_l - a_r^+ a_r}{2} \quad . \tag{3.13}$$

From the commutation rules for the creation and destruction operators, one gets that these new operators follow the angular momentum algebra. The total angular momentum J^2 is found to be equal to $N/2(N/2+1)$. This means that the total momentum is conserved and the whole dynamics can be thought to happen on a sphere with fixed radius (the Bloch sphere). Apart from terms proportional to N,

the Hamiltonian, written using the angular momentum operators, is

$$H = \frac{E_c}{2} J_z^2 - 2\frac{E_J}{N} J_x + \Delta J_z \quad . \tag{3.14}$$

From this we see that the $\pi/2$ pulse can be represented by a rotation of $\pi/2$ around the x axis and the phase accumulation is nothing but a rotation around the z axis by an angle ϕ. To describe the evolution on the Bloch sphere, one just needs to calculate the mean value $\langle J_i \rangle$ of the three momenta and their spread $\langle J_i^2 \rangle - \langle J_i \rangle^2$ on the initial state. The state will be described as a disk centered on the mean value and with radius given by the spread. If the state is prepared without interactions in the ground state of J_x, the fluctuations will be equally shared between J_z and J_y (see Fig.3.2). This kind of initial state will lead to a phase resolution given by the SQL.

Let us now try to figure out the action of the non-linear term in J_z^2 on the initial state. In the upper hemisphere, the effect of J_z^2 is in the same direction as the one of J_z, while in the lower hemisphere the effects are opposite. Moreover, points further away from the equator are influenced the most. The initial circle, representing the coherent state, is therefore stretched, resulting in larger spread along the equator than along the rotation axis. This number squeezing in the initial state leads to higher sensitivity in the phase measurement,

$$\Delta\phi = \frac{\xi}{\sqrt{mN}} \tag{3.15}$$

where $\xi < 1$ is the squeezing parameter. The enhanced sensitivity, caused by squeezing, can be visualized in Fig.3.3.

The interferometric sequence, as I describe it, assumes that the non-linear term is negligible during the sequence. Its effect would be an interaction induced decoherence. The interferometric sequence needs therefore to be realized fast enough not to be influenced by the non-linearity. Usually the measured phase results from a coupling with a very weak external field, such that a long phase accumulation is

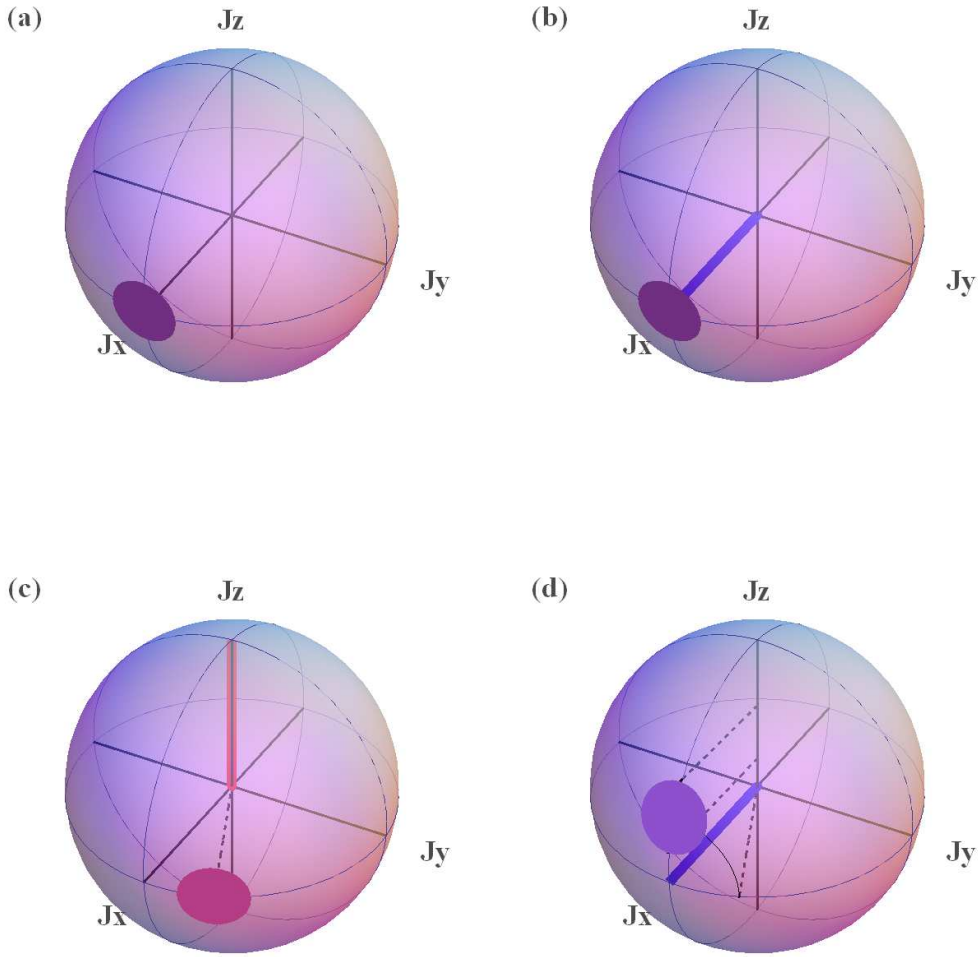

Figure 3.2: Representation of the interferometric sequence on the Bloch sphere: the initial state (a) is represented by a disk centered around the mean value of the momentum operators and with radius given by its spread. The first $\pi/2$ pulse (b) rotates the disk around its axis, it is followed by a phase accumulation (c) and the second $\pi/2$ pulse (d). The final measurement is sensitive to the projection of the disk on the z axis.

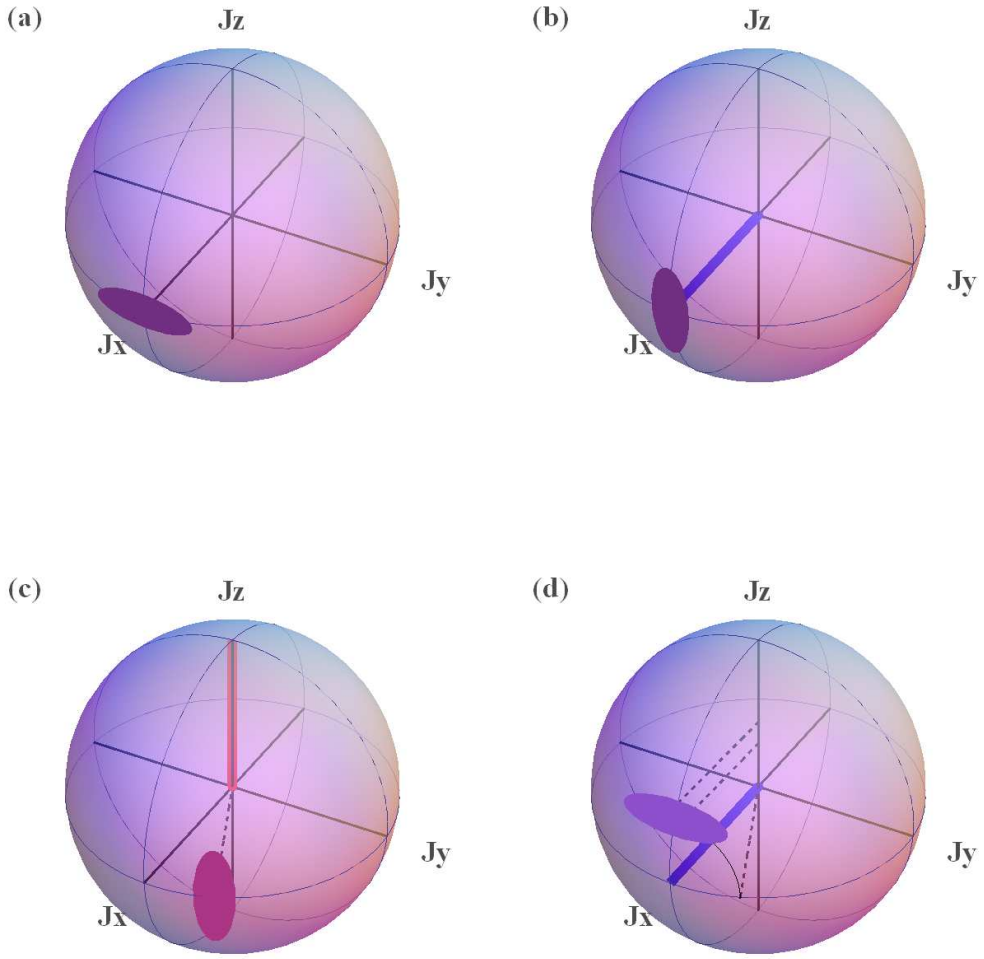

Figure 3.3: Representation of the interferometric sequence for a squeezed state on the Bloch sphere: the initial state (a) is represented by an ellipse centered around the mean value of the momentum operators and with axis given by its spreads. The first $\pi/2$ pulse (b) rotates the ellipse around its axis, it is followed by a phase accumulation (c) and the second $\pi/2$ pulse (d). The final measurement is sensitive to the projection of the ellipse on the z axis. The final resolution is enhanced due to the lower uncertainty on J_z

desirable. The use of a system with tunable interactions is therefore necessary, on the one hand, to exploit the interactions to create a squeezed state and, on the other, to reduce the interactions to zero during the interferometric sequence, allowing for long phase accumulation.

3.1.2 Entanglement and Fisher information

The resource exploited in order to beat the SQL in the example of the last section is actually entanglement. The system cannot be described any longer as an ensemble of independent particles but will be in an entangled state because of the introduction of an interaction term in the Hamiltonian. However, not all entangled states are actually able to lead to sub-shot noise sensitivity, but only a part of them[37]. Entanglement is a necessary condition but not sufficient. In order to distinguish useful entanglement, the tools of estimation theory are exploited. The interesting quantity we have to introduce is the Fisher information. Let us start by defining a parameter ϕ we want to measure and the generator of the translations of that parameter $\widehat{G}$ by

$$i\frac{d\psi}{d\phi} = \widehat{G}\psi \quad . \tag{3.16}$$

The measurement itself is performed by collapsing the wavefunction ψ onto the eigenstates of the measured quantity $|n\rangle$. The probability to measure n, given the true value of ϕ, is, therefore:

$$P(n|\phi) = |\langle n|\psi(\phi)\rangle|^2 \quad . \tag{3.17}$$

Under this assumptions we can write the Fisher information F as:

$$F = \int P(n|\phi)\left(\frac{d\log(P(n|\phi))}{d\phi}\right)^2 dn \quad . \tag{3.18}$$

The relevance of the Fisher information is related to the Cramer-Rao lower bound (CRLB)[38, 39], which sets the limit sensitivity in the measurement of ϕ after m

independent measurements to

$$\Delta\phi = \frac{1}{\sqrt{mF}} \quad . \tag{3.19}$$

In the case of independent particles, it can be proven that the Fisher information is additive

$$|\psi\rangle = \otimes_{i=1}^{N} |\psi\rangle_i \tag{3.20}$$

$$F(|\psi\rangle) = \sum_{i=1}^{N} F(|\psi\rangle_i) \quad . \tag{3.21}$$

In connection to the uncertainty principle, an upper bound for the Fisher information is given by:

$$F \leq 4\Delta^2 \widehat{G} \quad . \tag{3.22}$$

By using these properties of the Fischer information, we can derive the SQL and the ultimate limit to the sensitivity or Heisenberg limit (HL). If we deal with independent particles, the Fisher will have the following upper bound:

$$F(|\psi\rangle) = \sum_{i=1}^{N} F(|\psi\rangle_i) \leq N F_{max} \leq N\Delta^2_{max}\widehat{G} \quad . \tag{3.23}$$

The maximum uncertainty of an operator can be realized by using an equal superposition of its eigenstates with maximum and minimum eigenvalues

$$|\psi\rangle = \otimes_{i=1}^{N} \frac{|min_i\rangle + |max_i\rangle}{\sqrt{2}} \quad . \tag{3.24}$$

The value of $\Delta^2_{max}\widehat{G}$ in the single particle case is going to be a constant. The sensitivity limit therefore reads

$$\Delta\phi \propto \frac{1}{\sqrt{mN}} \tag{3.25}$$

which is the SQL. If instead we relax the independent particles assumption, we can only rely on the upper limit for the Fisher information. Proceeding as before, we end up searching the state with the maximum uncertainty of the $\widehat{G}$ operator, this

time in a many-body Hilbert space. If the operator is a single particle one, the maximum (minimum) eigenvalue is given by all particles being in the higher (lower) single particle eigenstate. The superposition of this two states is called NooN-state or, sometimes, a Schrödinger cat

$$|\psi\rangle = \frac{|min_1, min_2, ..., min_N\rangle + |max_1, max_2, ..., max_N\rangle}{\sqrt{2}} \quad . \tag{3.26}$$

The uncertainty $\Delta^2_{max}\widehat{G}$ in this case is N^2 times larger than in the single particle case, leading to the HL

$$\Delta\phi \propto \frac{1}{\sqrt{m}N} \quad . \tag{3.27}$$

In principle a NooN-state can be experimentally realized by driving the system into the ground state in presence of strong attractive interactions in a double well

$$|\psi\rangle = \frac{|N,0\rangle + |0,N\rangle}{\sqrt{2}} \quad .^{1} \tag{3.28}$$

The BEC is anyway not stable in such a situation[2]. A more feasible strategy is to use strong repulsive interactions to drive the system in a twin-Fock state

$$|\psi\rangle = \left|\frac{N}{2}, \frac{N}{2}\right\rangle \quad . \tag{3.29}$$

Thia state is characterized by an exactly half filling of both wells. The uncertainty for it is larger than the one given by the NooN state, nevertheless the scaling with N of the uncertainty of the phase measurement can be proven to be the same.

Such highly entangled states have anyway drawbacks, since they are more subject to any form of loss or decoherence than the normal product states. As an example we can imagine to have prepared a NooN state and, by some process (as three body losses or collisions with the background gas), one atom is lost from the double well.

[1] here, differently from the previous analysis, the mean occupation of the wells (the value of n_l, n_r) is indicated to describe the state instead of the single particle state.

[2] a more effective strategy to create a noon state that does not involve attractive interactions can be realized by the creation of a phase cat and subsequent application of a $\pi/2$ pulse[40].

It is in principle possible to get informations about the state of the system by using a suitable detector to trace the lost atom back to its original position in one of the two wells. The system therefore is forced to collapse in only that one well, losing its coherence.

Chapter 4

Experimental apparatus

In this chapter I describe the realized experimental apparatus, which comprises of a great part of my PhD work. The design of the apparatus had to take into account the crucial aspects of laser and evaporative cooling of potassium as well as the required conditions to perform high-precision interferometry. The main components of the apparatus are presented in Fig.4.1. The system is composed of three main vacuum chambers. In the first one, the atoms are collected from the background gas into a two-dimensional magneto-optical (2D-MOT) trap, producing an atomic beam. The atomic beam is directed to the second chamber where a three-dimensional magneto-optical trap (3D-MOT) is hosted. In the 3D-MOT, the sample is cooled to sub-Doppler temperatures. Once the atoms are prepared, they get transferred to a magnetic trap. Such magnetic trap is moved by mean of a motorized translation stage up to the third chamber (science chamber). In the science chamber the atoms gets trapped into a dipole trap and evaporative cooling performed employing a Feshbach resonance to increase the elastic collisional rate.

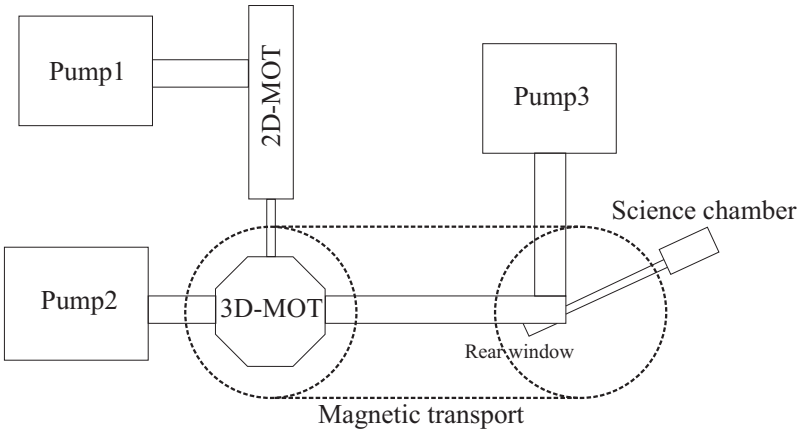

Figure 4.1: Simplified sketch of the main parts of the apparatus. The atoms from the 2D-MOT are collected into the 3D-MOT. Moving colis are used to transfer the atoms from the 3D-MOT chamber to the science chamber. The last vacuum pipe is not parallel to the magnetic coil motion, for this reason the last part of the atomic transfer has to be purely magnetic from the moving coils to the Feshbach coils. The distance between the coil's centers is about 10 cm. This allows for an extra optical access through the rear window.

4.1 Experimental design

A very long lifetime of the atomic sample is desired for high resolution interferometry, in order to achieve long phase accumulation. A very large optical access is also necessary, because of the particular implementation of a light-made double-well interferometer and of all-optical evaporation of the atomic sample. A large optical access will enable us to use many trapping beams as well as to implement high spatial resolution imaging.

In order to satisfy these conditions, we decided to use a scheme with three vacuum chambers (see Fig.4.2). In the passage from each chamber to the next one, a differential pumping stage reduces the pressure an thus it increases the lifetime of the atomic sample. The first cell hosts a two-dimensional MOT. A relatively high

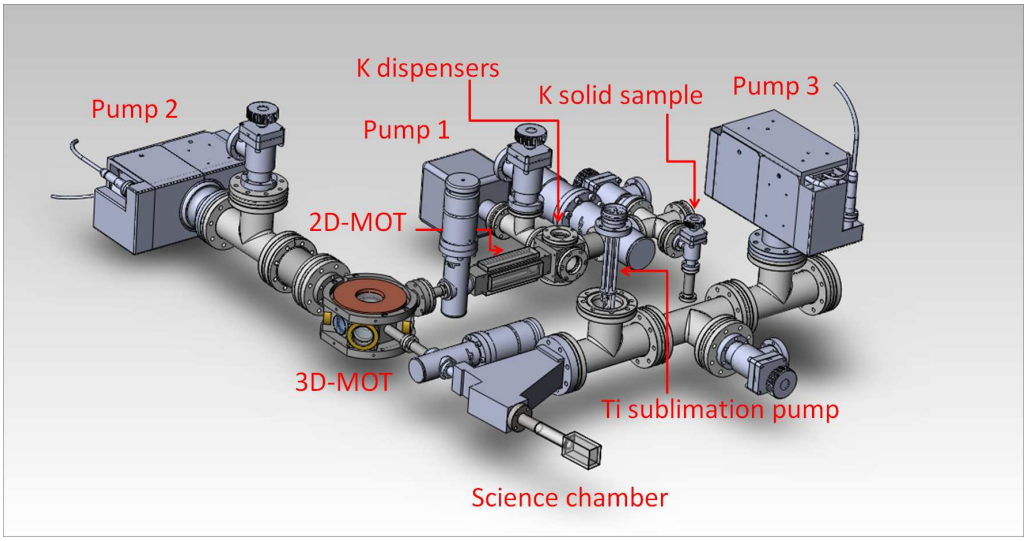

Figure 4.2: Overview of the vacuum system. The three chambers are indicated as 2D-MOT, 3D-MOT and science chamber. The position of the potassium solid sample and of the potassium dispensers is indicated. To make the sublimation pump visible, the vacuum pipe containing it was omitted from the drawing.

pressure of potassium vapor, of around 10^{-8} mbar, ensures a fast loading rate and thus a large atomic flux towards the second cell. In the second cell, large laser beams are used in order to trap a large number of atoms; here the pressure drops to around 10^{-9} mbar. The atoms are then transferred to the last chamber, using trapping coils mounted on a moving cart. The last chamber allows a very large optical access, due to its shape and to the absence of MOT beams for the cooling. The last differential pumping stage also allows to achieve pressures as low as 10^{-11} mbar.

4.2 Choice of the building materials

Since the interferometer will be performed with magnetic atoms, particular care was taken in order to reduce any magnetic field fluctuation or instability, in particular very close to the science chamber. For this purpose the main body of the optical

table, that holds the vacuum system, is a custom TMC realization made of the 304 low magnetic stainless steel alloy. The 316L alloy, characterized by an even lower magneticity, is used for the topmost and lowermost planes of the table.

The MOT chambers are realized in Ti-6Al-4V, for its low magneticity (four times lower than for steel) and high resistivity. High resistance materials allows for fast variation of the magnetic fields thanks to the rapid fall off of Eddie currents. Components that are close to the atoms, like vacuum chambers, pipes, valves and bellows through which the sample is passing during the transport, are realized in low magneticity stainless steel compounds like the SS304 or the SS316 compounds. For the vacuum connections towards the pumps the SS321 alloy is employed instead. The science cell itself is realized in glass and it is placed with its center 15cm away from the first metallic element (its own vacuum valve), realized in 316L stainless steel. The Feshbach coils, used to tune the interactions, are held by a fully plastic mount and kept in physical contact with the cooling water.

4.3 Vacuum pumps

In this section, I will justify the choices made for what concerns the pumping of the vacuum assembly and I will give indications of the achieved vacuum levels in the apparatus with their limitations. Finally, I will be report the measurements of the achieved atomic sample lifetime in the various vacuum sections, yielding the final confirmation of the achievement of low pressures. The sample lifetime is proportional to the inverse of the background pressure. A simple calculation based on the background collisions cross section yields a lifetime of the sample between 2 and 8 s (depending on the chemical composition of the background gas) for a pressure of 10^{-9} mbar.

The achievement of sufficiently low pressure values required a baking procedure

that eliminates condensed water laying onto the internal surfaces of the system and most of the hydrogen accumulated in the steel during its fusion process. We baked all the steel components separately in an oven for approximately one day at 400° C to eliminate most of the hydrogen. After the system was assembled we baked the 2D-MOT and 3D-MOT parts at 120° C for five days. The chosen temperature was limited by the sealing glue used for the vacuum windows. The science chamber section was added later on and separately baked. Since there was no glue on this section, the baking temperature was chosen to be 200° C; again the procedure lasted for five days.

In Fig.4.2, the position of the various pumps is depicted. The pumps used in the first two cells are Varian Diode Vaclon ionic pumps with different pumping speeds. These pumps are particularly indicated for pumping of active gases such as N_2, O_2, CO_2, H_2. Especially Hydrogen is supposed to be abundantly outgassed from the steel composing the vacuum chambers due to its fabrication process. For the pumping of the science chamber we chose, instead, a StarCell ion pump in combination with a Titanium sublimation pump (TSP). The StarCell achieves slightly lower pumping speeds for active gases than the Diode model but can pump much better noble gases as He and Ar or Methane. The pumping of active gases is provided by the Titanium sublimation pump in this case.

The current reading on the pumps provides an indication of the pressure in the first two vacuum chambers. The reading performed this way is limited by leakage currents of about 10 μA. This represents a limit pressure reading of about 10^{-7}-10^{-8} mbar. Both the pumps reports current readings comparable to their leakage currents. Close to the StarCell a Varian UHV-24p nude Bayard-Alpert type ionization gauge tube was placed. Its pressure reading is 7×10^{-12} mbar which is represents the lower detectable value. However, those readings are performed close to the pumps, the real pressure in the vacuum chambers has to be inferred from the

conductances and the outgassing rates.

The 2D-MOT section of the vacuum is pumped by a 20 l/s Varian Diode Vaclon ion pump. The effective pumping speed at the chamber decreases to 6.8 l/s due to the conductance of the connections (all the values are calculated for air). By calculating the outgassing of the various surfaces, we estimate an achievable pressure of 1.5×10^{-9} mbar. The conductance to the 3D-MOT chamber is negligible (0.03 l/s). During normal operation, the outgassing rate is deliberately increased by releasing potassium in the chamber, either by passing current through dispensers or by heating a solid sample. We measured the absorption of a laser beam tuned to the D2 resonance to estimate the partial pressure of potassium in the chamber. We estimated a partial pressure of 10^{-8} mbar, under the assumption that the atomic velocity distribution is in thermal equilibrium at room temperature.

For the 3D-MOT we used a 55 l/s Varian Diode Vaclon ion pump. The effective pumping speed at the chamber is estimated to be 17 l/s. The leading contribution to the outgassing comes from the sealing glue used for the windows. The nominal value for the outgasing of such a glue is 1.3×10^{-9} mbar$\times$l/(s$\times$cm^2). Such outgassing rate would limit the attainable pressure to 7×10^{-10} mbar, if we consider an exposed surface given by the total length of the sealings times an estimated 1 mm thickness. This pressure is compatible with the observed lifetime of the atomic cloud of 3-4 s.

For the science chamber we used a combined pumping system composed by a 55 l/s StarCell Vaclon ion pump and a three filaments TSP. The TSP was positioned in order to deposit Titanium on an area as large as possible. Its pumping speed is, in fact, directly proportional to the deposition area. We estimated a total pumping speed of 450 l/s by considering the nominal pumping speed for H_2 and the total area seen by the filaments. Such pumping is performed on a vast area, the conductance towards the final chamber is anyway dominated by the last section of glass pipe. Considering only this conductance, the estimated pumping speed at the final position

of the atoms is only 5 l/s. The same considerations holds for the StarCell. If we assume the outgassing rate of spectrosil, the special glass the science chamber is composed of, to be similar to the one of ordinary glass (10^{-12} mbar$\times$l/(s$\times$cm^2)), we get an achievable pressure of 10^{-11} mbar. Therefore, our pumping strategy consisted, first of all, in achieving high pumping speed at the conjunction of the glass pipe to the main body of the vacuum system. This way we could have a high differential vacuum with respect to the rest of the apparatus. For the pressure to be good in the glass chamber we than had to rely on the low outgassing rate of the materials employed. The measured lifetime of the atomic cloud in the science chamber, for atoms held in a quadrupole magnetic trap, was 80 s, confirming the validity of the approach.

4.4 Cooling laser system

The conditions the laser system needs to satisfy are dictated from the experience of previous experiments on laser cooling of potassium. First of all K, like all other alkaline metals, has an hyperfine structure. The main consequence of it the hyperfine structure is the presence of two sublevels in the $^2S_{1/2}$ ground state, labeled by the value of the total angular momentum $F = 1, 2$[41] . The $F = 2 \rightarrow F' = 3$ transition of the D2 line from $^2S_{1/2}$ to $^2P_{3/2}$ shows the largest dipole moment, and therefore is the most suitable for cooling.

Out of resonance transitions are stronger in potassium than in other alkalis due to the narrow hyperfine structure of the excited level, single frequency cooling results, therefore, in a very fast accumulation of the atoms in the uncoupled ground state. To prevent it, one needs to implement a repumping laser tuned to the $F = 1 \rightarrow F' = 2$ transition.

In order to give an estimation of the depumping rate, we can consider the effect

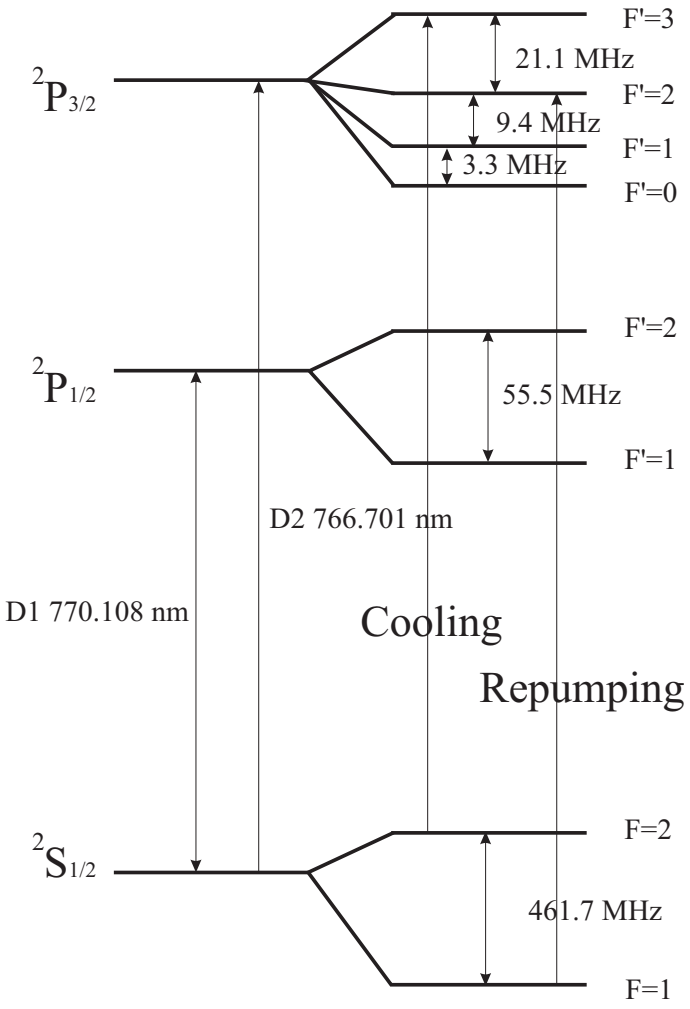

Figure 4.3: Scheme of the relevant atomic levels of ^{39}K. The assumed zero detuning transitions for the cooling and repumping lights are also indicated.

of a laser tuned in resonance with the cooling transition. We will take a random polarization, since this is the typical situation for the resultant field seen by the atoms in a MOT, and we will consider the atoms to be initially in F=2. In such a situation, for low saturation, after an absorption-reemission cycle the atoms will end up in F=1 with a probability equal to $1.5(4)\times10^{-3}$ for ^{39}K (^{41}K). For comparison, in the same conditions for ^{87}Rb, such probability would be 1×10^{-5}. These numbers means that, if one considers a typical scattering rate given by $\Gamma/2$, almost all the atoms will be found in the F=1 state after only 35 μs. In typical operating condi-

tions, power broadening and out of resonance operation increase the depumping rate even more. For this reason the role of the repumping beam becomes comparable to the one of the cooling laser. Therefore, during the typical operation of the MOT, the repumping and cooling lasers have the same power. High intensity and large beams are both desirable to increase the velocity capture range of the MOTs and the maximum trapped atom number. These requirements points to large power in both the repumper and cooling laser. We decided, therefore, to employ 4 master oscillator power amplifiers (MOPA).

The laser system for both the MOTs is derived from a single master laser, a Toptica DL Pro 780. This laser is very stable but provides only 50 mW at our working wavelength. The laser is thus amplified by 4 MOPAs. Each of these amplifiers is able to provide up to 2 W of laser power with an injection lower than 50 mW. The spectral characteristics of the injected light are retained after amplification but the spatial mode of the laser beam deteriorates. Spatial mode filtering is thus needed and it is performed by injection of the laser beams into optical fibers.

The different light frequencies used in the experiment are obtained from the master laser's one by the use of a number of acousto-optical modulators (AOMs). The hyperfine splitting that separates the cooling from the repumping transition is only 462 MHz. The distance between the two lines can, therefore, be covered by a double-pass AOM, so that the same laser source can be used for both.

The whole laser system is presented in Fig.4.4. The depicted 200 MHz AOMs are operated in double pass to achieve frequency control in a bandwidth of around $\pm$50 MHz per AOM without changing the beam alignment. The 80 MHz modulators are instead used to control the laser power. Acting on the RF power sent to the modulator itself the efficiency of the AOM, and therefore the output power, can be controlled. This technique gives us the possibility to decrease the laser power in a few μs down to 10^{-3} of its initial value. The complete switching off of the light is

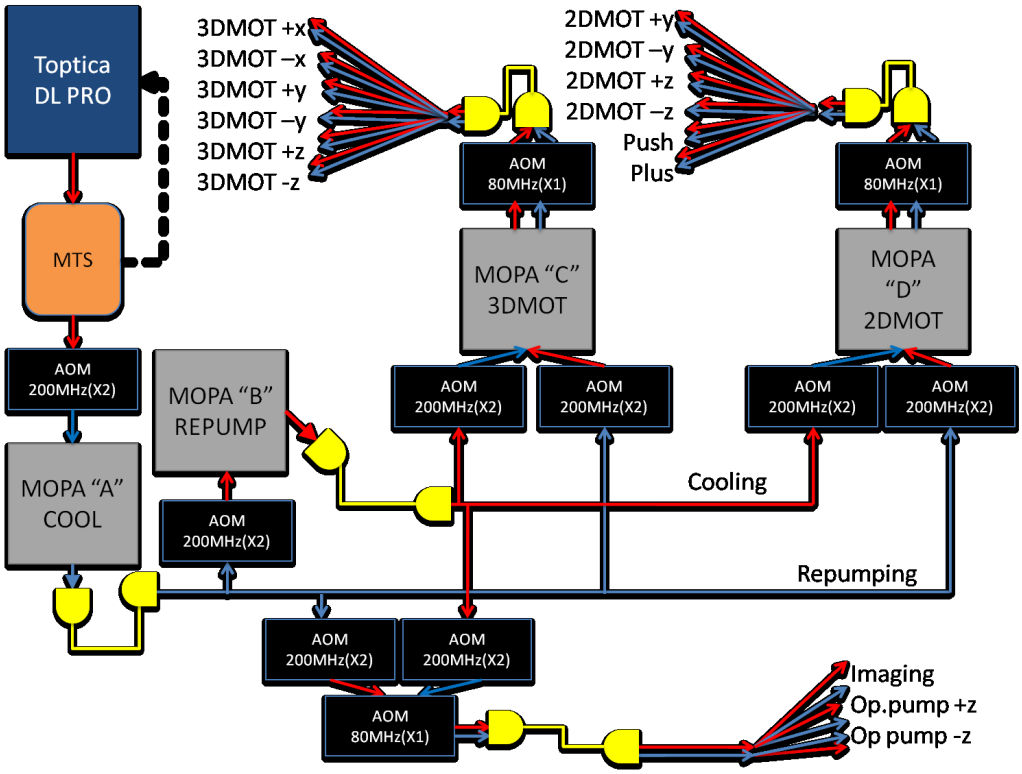

Figure 4.4: Laser setup for the cooling beams. The light from the DL-Pro master laser is used to perform spectroscopy using the modulation transfer technique (MTS). The obtained error signal is used to stabilize the master laser frequency. The red (blue) line indicate a laser frequency which is close to the cooling (repumping) transition of the D2 line of ^{39}K. All the MOPA amplifiers and AOMs are indicated. The yellow lines represents spatial mode cleaning by injection into optical fibers.

achieved by far slower (of the order of hundreds of μs) mechanical shutters placed in front of the fibers.

4.4.1 Laser locking

In order to lock a laser on an atomic transition, an error signal has to be generated and fed to a PID controller acting in some way on the laser frequency. The actuator we use is a piezo-electric material in contact with the grating that provides the

second mirror of the external cavity of the laser. The error signal generation can result from a wide variety of spectroscopic techniques. The technique we use is the modulation transfer spectroscopy[42, 43]. This is a pump-probe technique that is known to give very flat baselines and stable locking point. Here I give a simple description of the generation of the error signal in a two-level system and discuss the possible complications of an intrinsically multilevel system like for K. For convention I will call the detected laser beam "probe" and the other one "pump", even if the powers of the two beams are roughly equal.

The pump beam is passed in an electro-optical modulator (EOM) before entering the vapor cell with the atoms. The EOM consists in an optical element whose index of refraction $n = n_0 + \delta n(V)$ depends on the applied voltage V on it. By modulating such voltage at a given frequency ω_m, the output electric field E will be:

$$E = E_0 \sin(\omega_c t + \delta \sin(\omega_m t)) = E_0 \left(\sum_{n=0}^{\infty} J_n(\delta) \sin(\omega_c + n\omega_m)t + \sum_{n=1}^{\infty} (-1)^n J_n(\delta) \sin(\omega_c - n\omega_m)t \right) \quad . \tag{4.1}$$

$\delta = kl\delta n$, with l the optical path length, is the modulation depth and J_n is the Bessel function of order n. Usually $\delta < 1$, such that the field can be described as a strong carrier at ω_c with two weak sidebands at $\omega_c \pm \omega_m$. Such modulated pump beam is aligned collinearly with an unmodulated probe beam propagating in the opposite direction through the vapor cell. Due to nonlinear response of the vapor, a modulation appears on the probe beam. We can describe the process as four-wave mixing. The carrier and one of the sidebands of the pump combine with the probe's carrier to generate a probe sideband through the $\chi^{(3)}$ third order susceptibility. On a fast photodiode, the beat note between the probe carrier and its sidebands at ω_m can be monitored. The amplitude of the beat note is zero exactly on resonance and shows a nice dispersive behavior, both in the in-phase and in-quadrature components of the electric field. The process is usually efficient on closed transitions, it is Doppler free

and almost independent of the linear absorption term. The signal offset is therefore very stable against fluctuations in power, polarization or temperature.

In our experiment, the EOM has a modulation frequency of 21 MHz and we measured the sidebands strength to be 30 % of the carrier. Since the excited state hyperfine splitting is of the order of the modulation frequency, we expect the multi-level nature of the transition to complicate the picture a little. We observe, in fact, a complicated behavior of the signal with the polarization of the two beams; moreover, the zero-crossing of the dispersive signal is offset from the absorption resonance by about 30 MHz and the lineshape is clearly asymmetric as can be seen from Fig.4.5. The locking point is very stable and the signal has a very flat baseline. The behavior with polarization tends to favor the real transitions when the two polarizations are circular and opposite, while the cross-overs are favored when the polarizations are the same.

4.4.2 Master-oscillator-power-amplifier

We have built 4 home-made master oscillator power amplifiers (MOPA), in order to provide the laser power needed for the experiment. Each MOPA consists of an Eagleyard Photonics GaAs tapered amplifier (TA) held on a custom mount. Each mount includes input and output collimators as well as a Peltier element and a negative temperature coefficient resistor (NTC) to stabilize the temperature. The power output is usually set to about 1.2 W for the terminal MOPAs (C and D in Fig.4.4) and to 700 mW for the intermediate ones (A and B). The output beam from the chip is strongly astigmatic. In order to shape the beam mode we first placed the output collimator in order to collimate the beam in the direction of stronger divergence. Then we employed a cylindrical lens to collimate the other direction. The beam is then sent to a fiber for mode cleaning. The optimization of the coupling into the fibers was highly non trivial since the mode shape and its

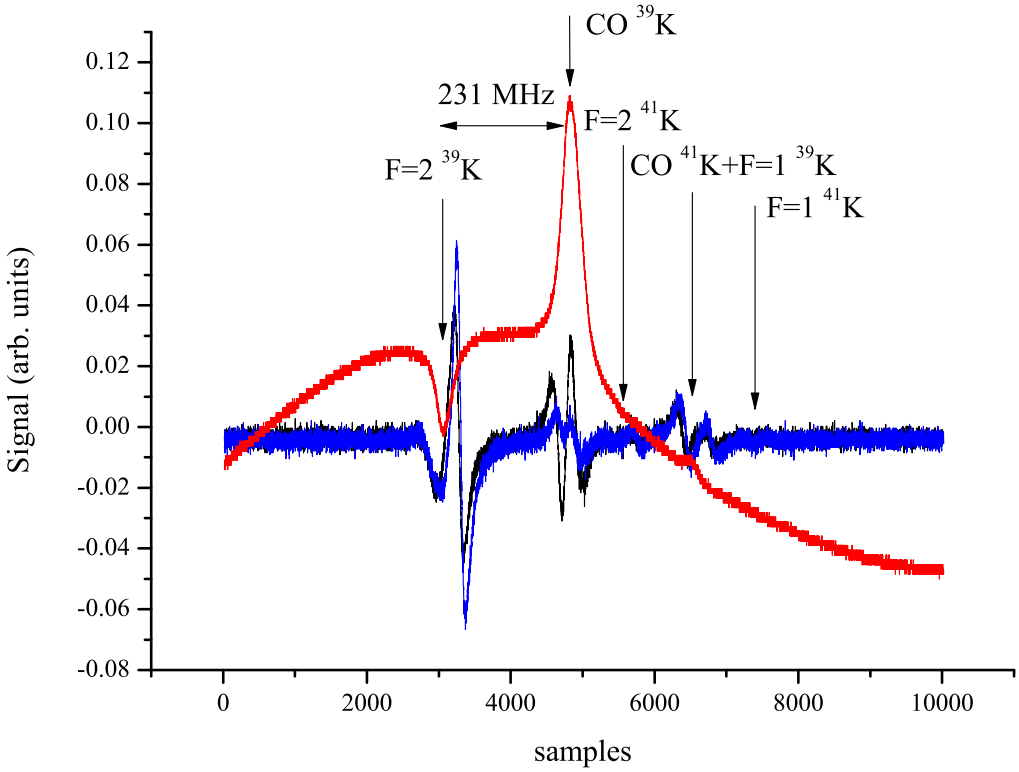

Figure 4.5: Spectroscopy signal as acquired from the measurement of the probe power with a fast photodiode while a voltage ramp was applied on the laser piezo. The DC signal (red) shows the broad Doppler resonance and some sub-Doppler features due to the pump and probe interplay. The features are assigned to the various K transitions, only the lower state is reported since the excited state structure is completely unresolved, CO stands for crossover. The crossover is characterized by an increased absorption due to optical pumping processes. The black and blue curves are demodulated signals after passing through a lock-in amplifier for different polarization. For opposite circular polarization (blue), the real transition signal is enhanced, while when the polarizations are circular but equal (black), the crossover is enhanced. For both the measurements the lock-in phase delay was optimized to get the maximum signal on the F=2 transition on which we perform the locking.

collimation changes with the power and the beams are absolutely non-Gaussian (see Fig.4.7). After a tedious optimization we could get up to a 50 % transmission on

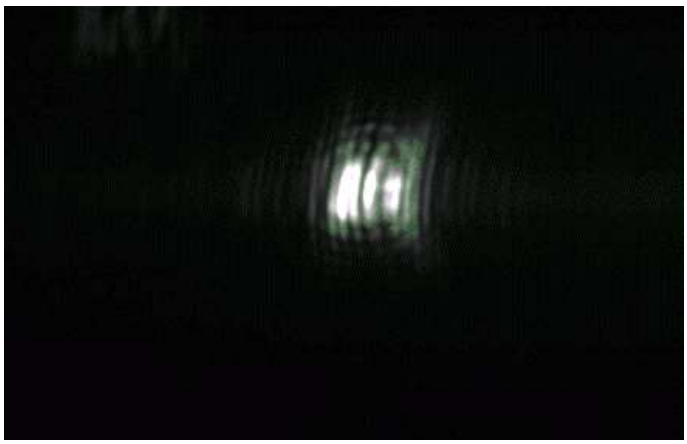

Figure 4.6: MOPA beam profile as seen after collimation. The spontaneous emission has a different divergence, as can be seen from the horizontal tails of the beam. The main beam presents interference fringes. Since these are different for the various MOPAs, an independent optimization for each beam is necessary. The beam waist in the image is about 500 μm.

such fibers. Due to an additional passage into an AOM for the terminal MOPAs, this sets the total available power for each of the MOTs to 400 mW.

4.4.3 High-power optical fibers

Since the employed power is rather high and polarization maintaining is required, we decided to implement high power NKT PM-15 photonic crystal fibers. The guiding core of such fibers is made of properly arranged holes into the glass mantle, such that the maximum laser power is in a non-absorbing region. Moreover, the coupling efficiency into the fibers for the MOPA is only 50 %. Therefore, half of the power will be dissipated in the cladding. In order not to damage the fibers, we employed the SMA-905 coupler at the fiber entrance. This coupler is specialy designed for

high power operation and devotes the initial section of the fiber to the removal of cladding modes.

Anyway, we experimentally verified that the polarization maintainance of such fibers is much more efficient for longer wavelengths. For operation with a 1064 nm high power (30 W) laser the power fluctuations were around 1 % and the operation was very stable on long time scales. For the cooling lasers at 767 nm and with only 1 W, instead, the fluctuations were as large as 10 % and periodic readjustment was required.

4.5 Magnetic field coils

Different coils are used in the experiment, each of them had to be designed considering the operational requirements as well as the experimental constraints. The design of the coils was carried out by simulating the magnetic field produced by them using the RADIA package for Wolfram Mathematica[44]. The first coil arrangement is the one used for the 2D-MOT. For two-dimensional cooling and trapping, one needs to create a homogeneous field along the axis of the 2D-MOT (z axis) with zero field along the axis. Such a field configuration can be realized using 4 rectangular coils with the long side parallel to z, with the coil's axes (x, y) orthogonal with respect to each other and to the z axis. The current has to be opposite for coils facing each other for magneto-optical trapping. If the magnetic field lines are pointing inside the cell for one pair of coils, they have to point outside the cell for the other one. In this way the magnetic field gradient generated by one pair sums with the one generated by the other one along the coil's axes x and y; while it subtracts to zero along the 2D-MOT axis z.

The remaining coils are all made of circular pairs. If the current circulates in opposite directions in the two coils, they provide a given magnetic field gradient along

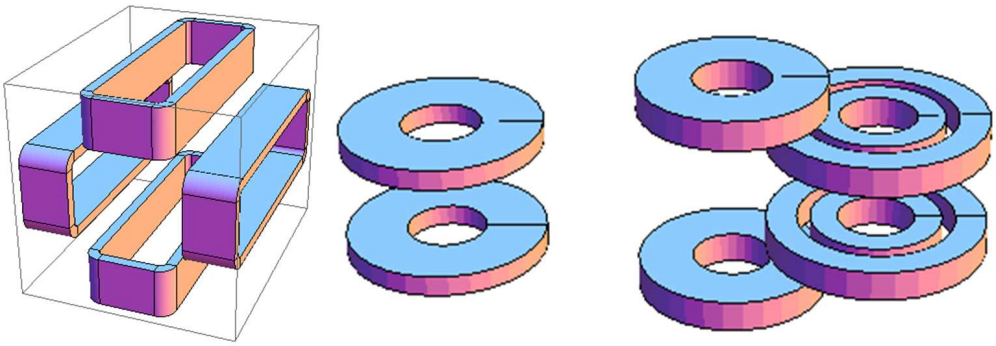

Figure 4.7: Design of the magnetic field coils. On the left the 2D-MOT rectangular coils, the atomic beam passes thought the center. On the right the rest of the magnetic field coils are presented in real scale between each other (only their distance was modified for convenience). The largest pair are the Transport coils, that moves the atoms towards the right of the picture from the 3D-MOT coils to the Feshbach/Gradient coils.

their axis, and half of that in the radial direction. If the current, instead, circulates in the same direction, they provide a constant magnetic field at the center. The 3D-MOT coils provide the magnetic field gradient for the 3D-MOT. The Transport coils are used for transferring the atoms from the 3D-MOT chamber to the science chamber. The Gradient and the Feshbach coils are mounted in a concentric way and they provide the needed magnetic fields in the science chamber. The names Gradient and Feshbach are only a convention. They are chosen since the Gradient is the one that generates the highest gradient when used in Anti-Helmholtz configuration, while the Feshbach is the one that creates the most homogeneous field at the center when used in Helmholtz configuration. A relay system allows to change the direction of the current in one of the coils of both pairs. This way we are able to use both the Gradient and the Feshbach in Helmholtz or Anti-Helmholtz[1] configuration. For

[1]the terms Helmholtz and Ant-Helmholtz are improperly used here just for easiness of explanation. The geometrical configuration of the Feshbach coils is close to the Helmoltz one, while the

example, the Feshbach coils have a larger radius and are, therefore, able to capture atoms from further away than the Gradient. Is thus useful to employ the Fesbach coils in Anti-Helmoltz configuration to transfer atoms from the Transport coil to the science chamber.

The building of the magnetic coils was home-made with exception of the 2D-MOT coils, that were realized by a local company (LEF). We used a 3.35×1.42 mm isolated copper wire held together by a special epoxy glue: Duralco NM25. This glue was chosen for its low magneticity and its good thermal conductivity. The distance from the atoms is the most critical parameter, since the gradient produced in the center of a pair of coils with opposite current and distance d decays as d^4 for distances larger than the coil radius. This is especially true for the Transport coils since they have to be far, in order to enclose other pairs, and they cannot be too heavy due to the recommended limit on the momentum torque on the moving cart. In order to reduce the distance between those coils we employed a building technique aimed at the reduction of the axial dimensions of the coils and at increase their homogeneity.

In normal spiral winding techniques, the winding of n vertical layers results in coils as high as n+1 layers. Since typically we have 2-6 vertical layers, removing the extra layer makes an appreciable difference. Our solution to do it was to wind each layer independently and to assemble them afterwards. The winding has to be reversed from one layer to the next and the electrical connections have to be to the inner conductor and to the outer one alternately. Such assembly results in a series of the various layers with the current circulating always in the same direction. The coils used for magnetic trapping required active water cooling. Their coil mount had therefore to be realized in order to provide a good thermal conduction from the coil to the water. The main parameters of all the coils can be found on Tab.4.1.

Gradient coil is close to the Anti-Helmholtz.

	Internal size mm	Nrad	Nax	Distance mm	γ/I G/(cm A)	B(0)/I G/A
2D-MOT	37x132	4	7	61	1.6	-
3D-MOT	56 ϕ	30	4	61	4.6	-
Transport	55 ϕ	27	6	107	2.7	-
Gradient	54 ϕ	15	6	49	4.6	11.2
Feshbach	111 ϕ	17	6	49	2.4	13.1

Table 4.1: Main characteristics of the used coils. For the 2D-MOT the coils are of rectangular shape and there are 4 of them, all the others are circular and come in pairs. $Nrad$ is the number of windings in the radial direction and Nax the number of layers along the coil axis. The distance is indicated between the closer surfaces of the conjugated pairs. γ is the axial magnetic field gradient generated when current is run with opposite sign in the coils. $B(0)$ is instead the central field obtained by passing current with the same sign in both the coils.

The 2D-MOT coils have an elongated rectangular shape. In order to cancel the magnetic gradient along the 2D-MOT axis we chose to use 2 pairs of coils, as explained before. we were actually able to trap atoms in an elongated 3D-MOT in the 2D-MOT chamber by using only one pair of coils. By adding the second pair, trapping of atoms was no more observed. The peculiarity of the 3D-MOT magnetic field is the very fast switching off (on the order of 100 μs) due to the high resistivity of the 3D-MOT chamber. Both the 2D-MOT and 3D-MOT coils are mounted on aluminum mounts. The 3D-MOT coils mount is also cut along a radius to prevent the formation of Eddie currents. The Transport coils are mounted on an aluminum structure attached to the moving cart, such structure is cut along a radius of the coils. Water is run inside the Transport coil's mount to keep the coils cold and the thermal conduction is enhanced by the application of epoxy glue between the coils

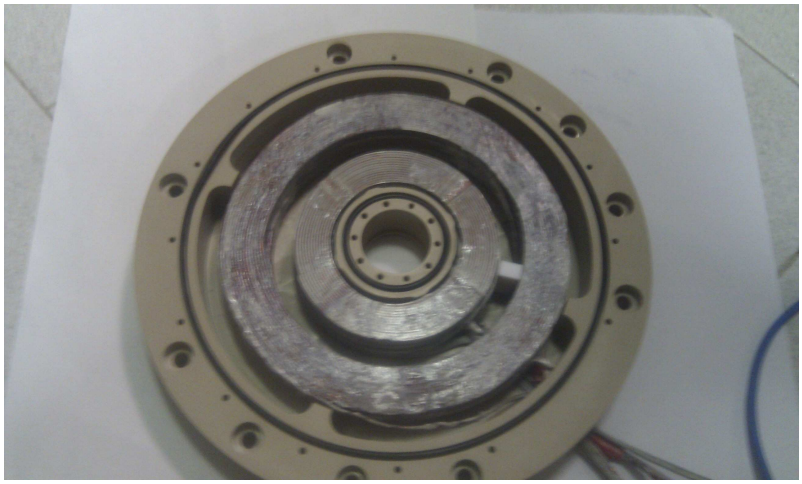

Figure 4.8: View of the Gradient (smaller) and Feshbach (larger) coils inside the plastic mount. Once the cap is closed, water is inserted through a hole in the cap and fills the empty spaces. The coils are supported 1.5 mm away from the mount internal surfaces to enable water to pass below and above the coils.

and the mount. The Gradient and Feshbach coils (Fig.4.11) are concentric and kept inside the same plastic mount. Water is continuously run inside the mount and the coils are in physical contact with the cooling water.

4.6 Potassium samples

The potassium vapor can be released into the apparatus by either four current-driven dispensers, located in the rear of the 2D-MOT chamber, or by heating a solid sample.

During the first two years of operation of the apparatus we used only the dispensers, due to their stability and convenience of operation. Since each dispenser contains only 3.7 mg of potassium their use is limited. The lifetime of a dispenser, at our operational current, was about one year. The result is that, at the moment, two dispensers are completely used up. In order to preserve the other two, we decided

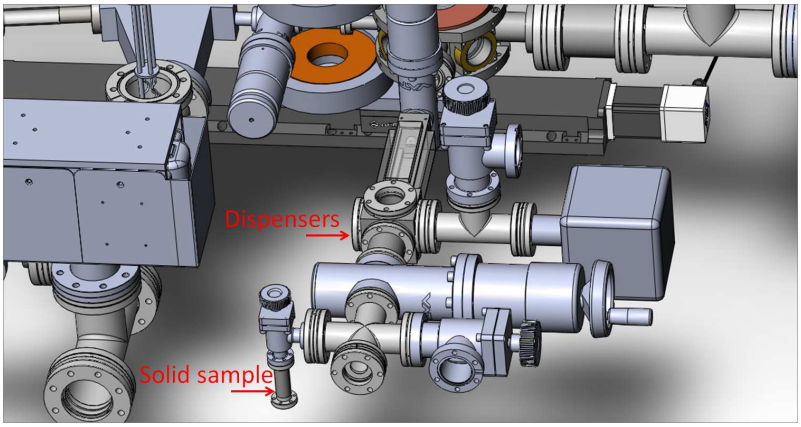

Figure 4.9: Close up on the region of the apparatus where the potassium samples are located. Four current driven dispensers K/NF/17/FT10+10 from SAES getters are located inside the cube at the terminal part of the 2D-MOT chamber. Current is run into the dispensers via a vacuum feed-through. The solid sample was heated up to 200° C in order for the oxide layer to melt and potassium to be released. In normal operation only the rear window is heated to 40° C in order not to deposit potassium on it. A vacuum valve allows to isolate the solid sample zone in order to replace it or to insert other elements.

to exploit the solid sample source. Such sample consists of 5 g of natural abundance potassium. In order to break the oxide layer, that formed on the surface of the metal, and to deposit potassium all around the 2D-MOT cell, we heated up the whole vacuum chamber at 80° C and the solid sample at about 200° C for a week. After that we could recover the same flux obtained using the dispensers. Heating was no more necessary, since potassium was deposited on all surfaces of the cell.

After the potassium release, we noticed that the rear window of the vacuum chamber was covered by a metallic layer. We decided, therefore, to keep the window hotter than the rest of the chamber. This is the only heated surface during the standard operation of the apparatus. Its temperature is kept at 40 °C. We have worked for around one year using this method and we did not notice any change

in the normal operating parameters. No further heating of the solid sample was necessary. We noticed anyway that the pressure reading on the vacuum pumps was increased with respect to the dispensers operation. Even though the reading is not reliable due to leakage currents, this indicates that the dispensers are cleaner sources. This is probably due to the directionality of their emission, resulting in a higher fraction of the emitted gas to be captured by the 2D-MOT with respect to the solid sample operation.

4.7 2D-MOT

The four beams used for the 2D-MOT are derived from a single optical fiber. The spectrum of the light coming out of the fiber is monitored with a Fabry-Perot cavity. This spectrum consists mainly of the two repumper and cooling lights, separated by Δ_G, the ground state hyperfine splitting. additional sidebands are present at ω_R+Δ_G and ω_C-Δ_G, with ω_G, R the repumping (cooling) frequency, which are generated by nonlinear effects inside the gain medium of the MOPA amplifier. These sidebands are anyway far detuned (about 400 MHz) with respect to the atomic transitions, such that their effect can normally be neglected.

The initial beam has a waist of 0.7 mm. For the radial trapping we applied a $\times$12.5 standard telescope followed by a $\times$5 cylindrical telescope on two beams, resulting in 9 mm and 44 mm for the vertical and horizontal beam waists respectively. The two beams are circularly polarized and retroreflected after passing through the vacuum chamber. The retroreflection results from total internal reflection on two right triangular base optical prisms. This way the ellipticity of the beams is conserved after reflection. Careful machining is required for the retroreflecting prisms. The right angle edge has to be sharp and the angle between the reflecting surfaces very close to 90° to avoid the formation of a dark region at the middle of

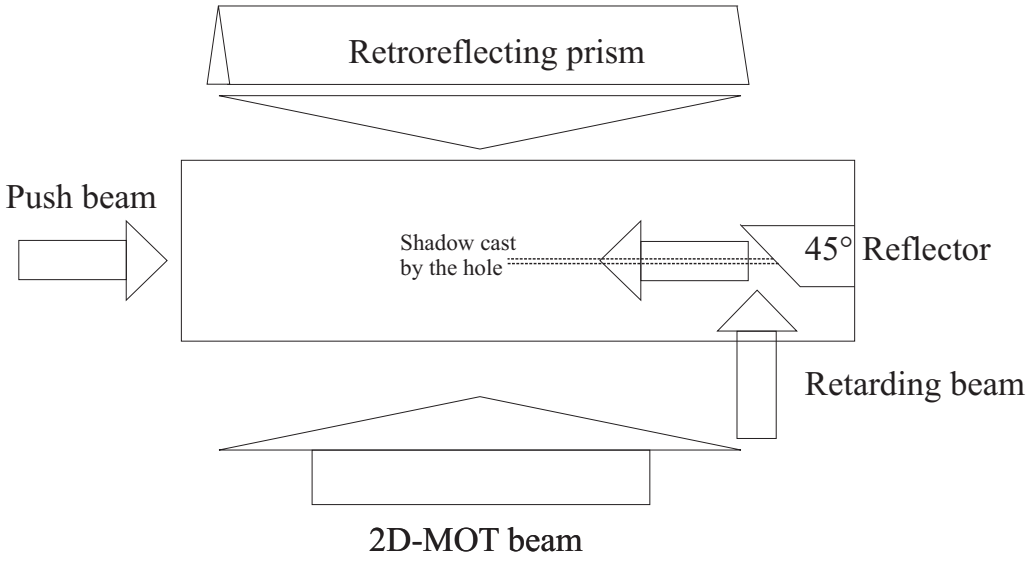

Figure 4.10: Scheme of the 2D-MOT. The main 2D-MOT beams have an elongated shape and are retroreflected via total internal reflection on 2 prisms. Only one cooling direction is shown in the drawing, the other one would be through the plane of the image. The push beam comes from the left side and the retarding beam is inserted from below the chamber, reflects on a 45° mirror inside the vacuum and propagates towards the left side. On this beam a shadow is created due to the hole at the center of the mirror through which the atoms are passing.

the beam.

The two dimensional MOT is operated in the $2D^+$ configuration[45] employing two additional laser beams along the atomic beam direction. The "push" beam, propagating in the direction of the atomic propagation and the "retarding" beam, propagating in the opposite direction. These beams have a waist of 5 mm, resulting from the application of a $\times 7.5$ telescope on the initial beam. The retarding beam is inserted into the vacuum chamber from below and it is retroreflected by a mirror at 45° inside the vacuum chamber. The metal substrate of the mirror was gold coated for high reflectivity. Furthermore, an extra MgF_2 coating was realized on top of the gold one to avoid deposition of potassium. The mirror has a 1.5 mm diameter hole at

its center through which the atomic beam is ejected. For this reason, the retarding beam carries the shadow of the hole at its center. For atoms outside the shadow, the resulting radiation pressure is balanced in all directions. Once the atoms are cooled down radially and therefore, spend most of their time at the center, the radiation pressure imbalance pushes them towards the 3D-MOT chamber. This configuration implies a longitudinal pre-cooling in addition to the radial one. The resulting atomic beams are slower and can be trapped more efficiently by the 3D-MOT.

4.8 3D-MOT

As in the 2D-MOT case, the 3D-MOT beams are derived from a single bichromatic beam containing both cooling and repumper. We use six independent beams for the 3D-MOT. From the initial 0.7 mm waist we apply $\times 25$ telescopes and we circularly polarize every beam. The resulting waist is 17.5 mm. We experience power losses of around 10 % due to the 2" mirrors at 45° used for steering the beams (18mm effective radius) and to the 4 cm diameter vacuum windows. In compense, we achieve a rather homogeneous illumination of the collection region. The atomic cloud spans the full region covered by the beams because of light-assisted collisions. These collisions are responsible for repulsive forces inside the cloud that limit the achievable density. Once the density reaches the limit value, further collection of atoms causes the MOT size to grow, eventually reaching the beam size. Because of this effect the total number of atoms collected critically depends on the MOT beams allignement.

4.9 Science chamber

In the science chamber we perform optical trapping using two dipole trap beams. We also employ a single probe beam resonant with the atomic transition for absorption

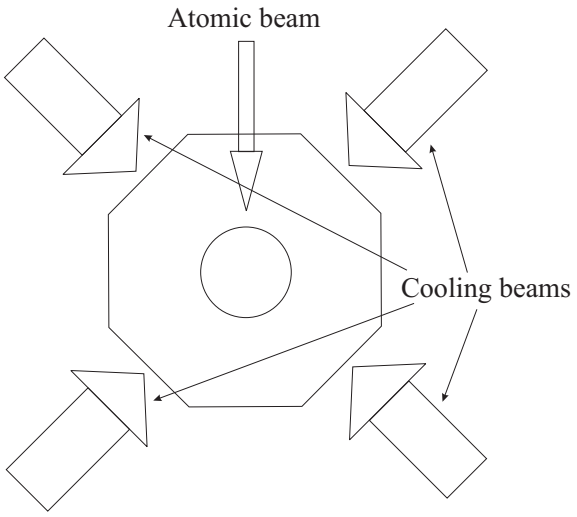

Figure 4.11: Scheme of the 3D-MOT. Atoms are coming from the 2D-MOT (up in the drawing) and trapped by the MOT beams, here the beams are not retroreflected, differently from the 2D-MOT case. The horizontal plane is shown in the drawing, an extra couple of beams are used for cooling in the vertical direction (through the plane of the image).

imaging. The beam propagates orthogonally to the largest side of the cell in order to allow for large numerical aperture of the imaging lens. The beam is used for imaging and also for optical pumping and has a waist of 7 mm with 1 mW total power.

At the moment, we use an aspheric lens with 40 mm focal length and 1" diameter to collect the imaging light. Such a lens has a nominal numerical aperture NA of 0.3, the design limit is 0.7. The design of a higher resolution imaging system is being carried out. The first lens is part of a $\times 2.5$ telescope. For this reason the pixel size is supposed to be the limiting resolution factor. The pixel size of our camera is 6.45 μm, therefore the effective pixel size is 2.6 μm. A typical imaging procedure consists of a 300 μs repumping pulse that changes the atomic internal state to the F=2 hyperfine state. Subsequently (100 μs later) the imaging pulse with only the

cooling light is switched of for another 100 μs and the light is collected by the ccd camera.

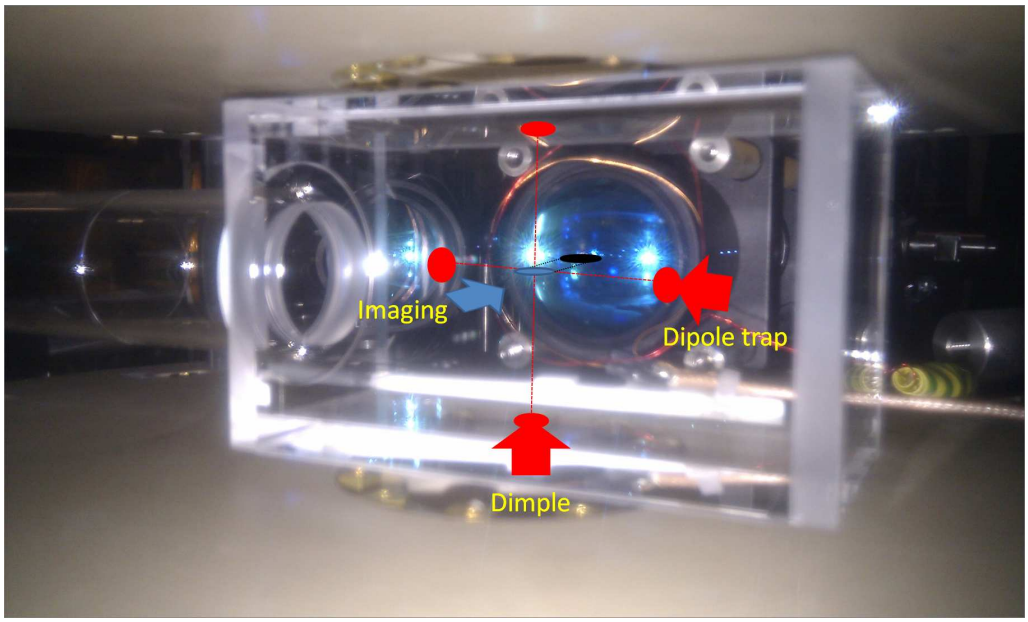

Figure 4.12: Picture of the science chamber inside the coil mounts. The beam paths of the dipole trap lasers and the imaging beam are indicated. the dipole trap beam crosses the cell at 45° with respect to the cell frontal side. Collection lens for the imaging and radio frequency antennas are also visible on the rear.

4.10 Magnetic transport

We use a moving cart to transport the atoms from the 3D-MOT chamber to the science chamber. the atoms are trapped in the quadrupole field generated by the transport coils. The coils are mounted on the moving platform (Aerotech pro115-600 linear stage). The moving platform can reach velocities up to 350 mm/s. The acceleration ramp is optimized minimizing the heating of the atomic cloud. The time-velocity ramp of the transport sequence comprises of a linear acceleration ramp, a constant velocity travel, and a linear deceleration ramp. The acceleration during

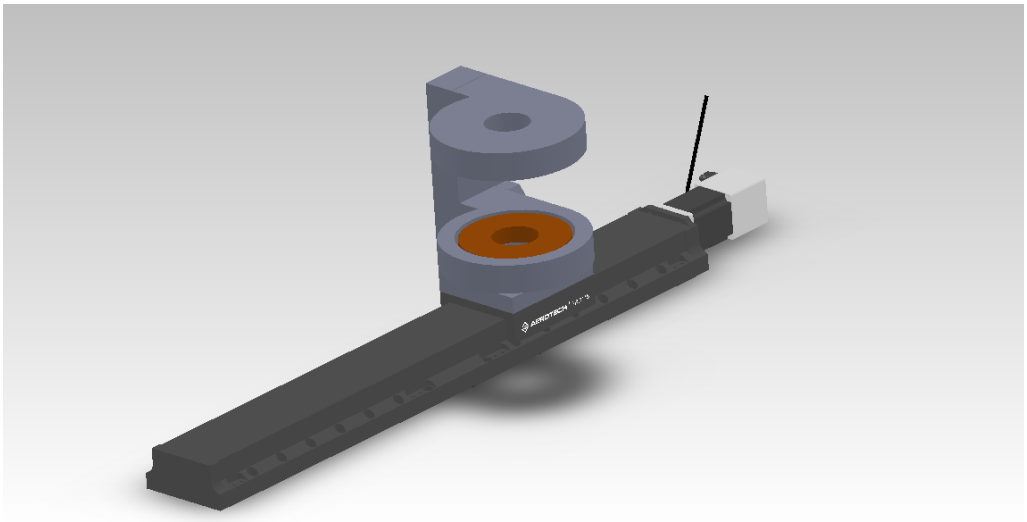

Figure 4.13: 3D model of the moving platform holding the transport coils

the ramps is 800 mm/s^2 and the constant speed section is traveled at 260 mm/s. The total traveled distance is 540 mm, in a total time of 2.4 s. This time adds to the time that is needed for the magnetic field ramps used in the transfer of the atoms from the 3D-MOT coils to the Transport coils (200 ms) and from the Transport to the Feshbach coils (500 ms). The magnetic transfer times were optimized by minimizing the heating of the cloud.

4.11 Radio-frequency antennas

During atomic preparation, radio frequency radiations can be used in order to manipulate the atomic spin state. For this purpose two radio frequency (RF) antennas were built. For low frequency operation, up to 50 MHz, a low inductance single loop antenna was assembled. A 50 Ω resistor in series with the antenna provides the impedence match to the output impedence of the generator. The low frequency antenna can drive transitions between atomic states belonging to the same hyperfine level (F=1 or 2) but with different m_F projection. For higher frequency operation

we assembled a single loop antenna with, in series, a 50 Ω resistor and a variable capacitor. The capacity was tuned in order to minimize power reflection in a frequency range of 400-500 MHz. This antenna can be used in order to change the F quantum number from 1 to 2 or vice-versa. Typical RF power used on these antennas is 1-3 W.

4.12 Trapping lasers

Two laser beams, the main dipole trap beam and the dimple beam (Fig.4.12), are used for optical trapping. The main dipole trap beam is derived from a IPG-photonics YLR-100-LP-AC ytterbium fiber laser. This laser can provide up to 100 W of laser power at a central wavelength λ=1064 nm, with an emission linewidth of 2 nm. We typically operate this laser at around 30 W output power due to strong photo-association losses caused by the wide emission (see Sec. 6.4.1). The laser is coupled into an AOM for power control, sent to a system of lenses and focused onto the atoms. The optics used for the beam preparation are made in fused-silica for its low absorption coefficient. On the last focusing lens we arrive with a 10 mm waist. The last lens has a focal length of 300 mm,. The beam waist at the focus was measured to be 25 μm, substantially larger than the 10 μm Gaussian beam estimation. This is due to deterioration of the beam quality after the AOM and by spherical aberrations on the focusing lens. The use of a small waist is necessary in order to achieve three dimensional trapping with a single beam and to enhance the atomic collisional rate during the accumulation of the atoms in the trap. The use of a crossed dipole trap is not straight-forward for this laser because of the large spectrum. The laser's spectrum largely exceeds the hyperfine splitting of the ground state. For this reason, Raman transitions, in which a photon is absorbed from one beam and emitted into the other, are allowed and can lead to heating of the sample.

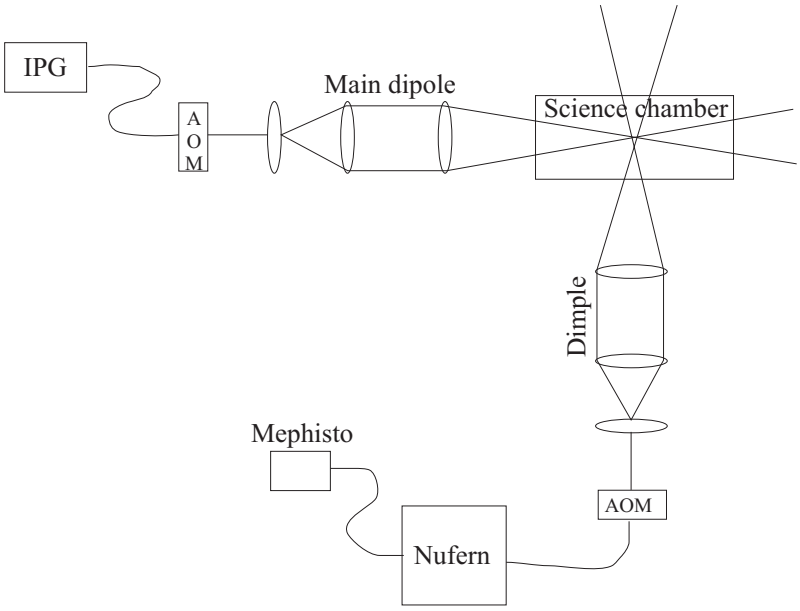

Figure 4.14: Simplified optical scheme used for the trapping beams. The main dipole beam is horizontal, but is not in fact orthogonal to the science chamber side as it may seem from the picture. In reality it crosses the cell at an angle of 45°. The dimple beam comes from below.

The dimple beam is generated from a Nufern ytterbium fiber amplifier seeded by an Innolight Mephisto S S200 NE. The amplifier can provide up to 10 W laser power. The optimized operation of the dimple trap requires only 200 mW. This beam, as the previous one, is sent to an AOM for power control, optically manipulated and focused onto the atoms. The laser waist at the atoms position is about 70 μm. Due to its low trap depth, the dimple laser does not influences the atomic distribution before the last stages of evaporation. Its purpose is mainly to increase the trapping frequency, and consequently the collision rate, once the main dipole trap depth is too weak to sustain the evaporative cooling. The laser is however switched on at the beginning of the evaporation sequence and its power is kept constant.

Chapter 5

Sub-Doppler laser cooling

In this chapter, I describe the main experimental procedures related to laser cooling. In the first section, I give an overview of sub-Doppler cooling on atoms with narrow hyperfine structure, related to the recent achievement of sub-Doppler cooling on the potassium bosonic isotopes[46]. Thereafter I describe the various operation of the 2D and 3D-MOT and the preparation of the atomic cloud.

5.1 Laser cooling, the special case of potassium

Sub-Doppler laser cooling of potassium was never achieved before because of its small hyperfine splitting and the lack of a closed cooling transition. Let us discuss the main problems of cooling in presence of a narrow hyperfine splitting and a high density of the cloud. While in principle, the lowest achievable sub-Doppler temperatures are independent of the laser detuning δ [47], the experiments with large density samples are performed at large detunings, $\delta \gg \Gamma$. This requirement arises from the need of keeping the scattering rate of photons by individual atoms low, in such a way that spontaneously emitted photons may not disturb the cooling process [48].

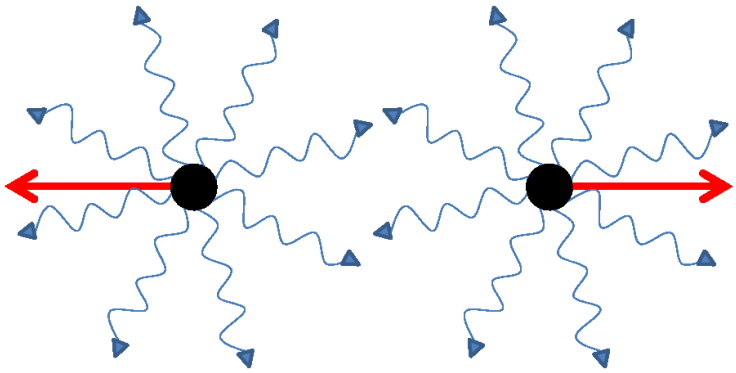

Figure 5.1: Net effect of the multiple scattering. Two atoms are scattering off photons at a rate $\Gamma/2\frac{s}{s+1}$ during the cooling process. In an opically thick sample their average distance is short such that those photons one emits might be reabsorbed by the other one determining heating and an effective repulsive force between the two.

The way spontaneously emitted photons linders the cooling is via rescattering of them by other atoms. The optical thickness of the cloud

$$d = \sigma n l = \frac{3\lambda^2}{2\pi} \frac{I/I_s}{1 + I/I_s + 4\delta^2/\Gamma^2} nl, \tag{5.1}$$

where σ is the scattering cross section and l is the average linear size of the cloud, represents the probability of absorption of a photon inside the cloud. When d becomes of the order of 1, or larger, the fluorescence photons emitted at the center of the cloud as a result of the cooling process itself, are likely to be reabsorbed on their way out. This causes many issues when working with dense samples ($n > 10^9$ atoms/cm^3). First of all, rescattering generates an effective repulsive force which limits the achievable density (see Fig.5.1). Moreover the reabsorbed photons effectively increase the diffusion coefficient in momentum space D_p, causing the equilibrium temperature to increase. In principle, by increasing the detuning δ, the thickness d can be reduced and the cooling becomes more efficient. However, most atomic systems cannot be modeled as simple two-level ones since they feature a hyperfine structure like the

one in Fig. 5.2 that is relevant for instance to Na, K and Rb. In this case, it is commonly thought that δ must also be smaller than the main hyperfine splitting Δ, since otherwise the presence of the other excited states would turn the sub-Doppler mechanism into a heating one. A problem therefore arises when trying to cool a dense sample in presence of a narrow hyperfine structure, since the increase of δ needed to reduce rescattering is limited by the hyperfine splitting. As a matter of fact, in the case of the bosonic K isotopes, where $\Delta \approx 2 - 3\Gamma$, a clear sub-Doppler cooling has not been experimentally observed so far.

To understand better the issues of cooling in presence of a narrow hyperfine structure, I performed detailed calculations. In Fig.5.2 a calculation of the cooling force for various detunings is reported. The picture indicates the presence of different detuning zones with different behavior of the cooling force. The interesting ones are the ones for which the cooling force is opposite to the atomic velocity. This is true in the full velocity range only in the "green" zones (zone I). These are located either very close to resonance, where heating from photon reabsorption might be large, or for $\delta \gg \Delta$, where however the velocity capture range of the process becomes very low due to the large detuning. The conclusion one might draw is that efficient cooling for high density in potassium is not achievable.

5.1.1 Cooling forces for a narrow hyperfine structure

The calculations of the cooling forces are performed by solving the optical Bloch equations (OBE) of the multilevel atomic system. I have considered a 1D geometry and a $\sigma^+ - \sigma^-$ polarization configuration of the laser fields. The Bloch equations are solved using an adapted version of the code of ref. [49, 50]. This code solves the steady state equation for the density matrix

$$0 = \frac{i}{\hbar}[H + kvJ_z, \rho_{at}] + \gamma\rho_{at} \tag{5.2}$$

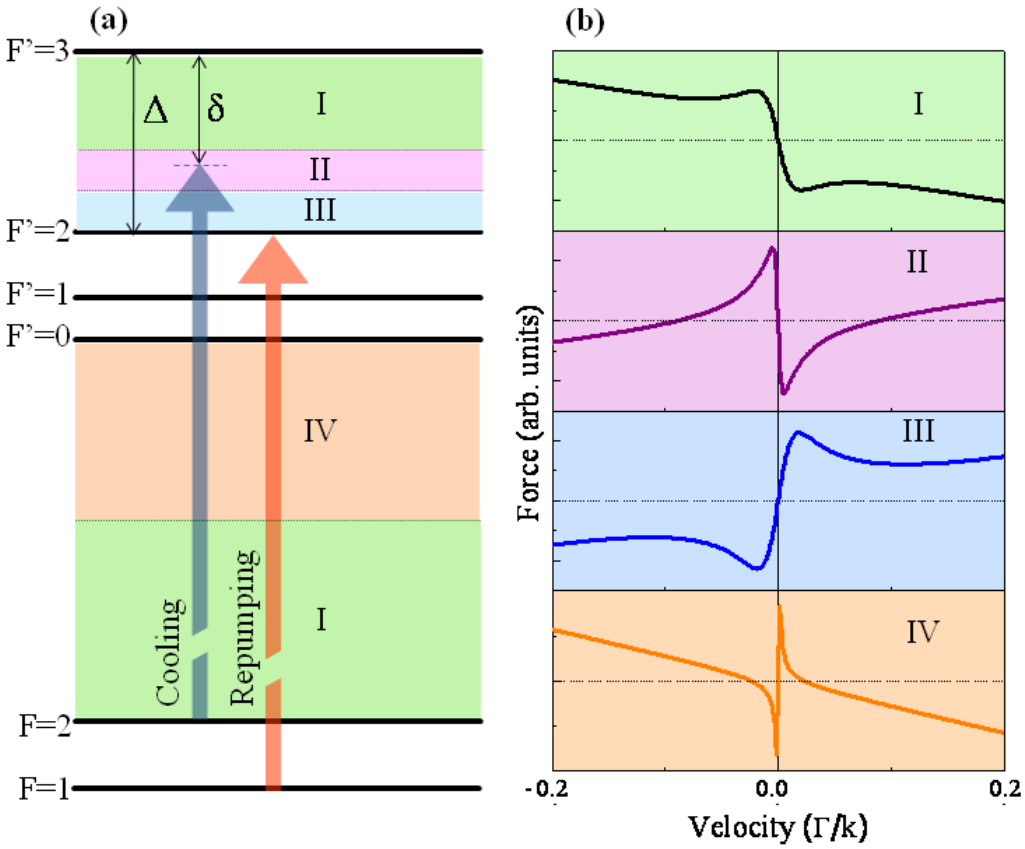

Figure 5.2: Working regions for sub-Doppler cooling of bosonic potassium. a) Level scheme including the relevant hyperfine splitting Δ and the cooling laser detuning δ. b) Calculated cooling forces vs the atomic velocity in the various regions of (a). Doppler cooling only takes place in regions I and IV, while sub-Doppler cooling is active only in regions I and II. Zones in between the F'=2 and F'=0 levels are not reported.

in which ρ_{at} is the internal atomic state density matrix (the code is written in the semiclassical approximation), γ represents coupling of the levels by spontaneous emission, while H represents the dipolar coupling of the various levels induced by the laser fields. The inertial rotation term experienced by the atoms in the rotating frame (see Sec.2.1.2) is also added. Once the density matrix as a function of the atomic velocity is found, the cooling force is calculated by

$$F = \nabla Tr\left(H\rho_{at}\right) \quad . \tag{5.3}$$

From the results of the calculations, 4 different cooling zones can be distinguished by the sign of the force as a function of the atomic velocity. My criterion to distinguish the zones was the following: to determine the sign of the force in the low velocity region I calculated it for $v = \sqrt{\frac{2E_R}{m}}$, while for the high velocity region I took the sign at a velocity $v = \sqrt{\frac{k_B T}{m}}$, with T=1 mK. This temperature was chosen to be of the order of the measured temperature in our MOT at the beginning of the cooling. Changing this choice for the velocity at which to perform the check can influence the exact position of some of the zones but not the qualitative description. Once we have the two signs we can assign zone I to the - - combination[1], zone II to the - + one, zone III to + + and zone IV to + - (see Fig.5.2 for typical examples of the force behavior in the different zones).

To investigate whether these considerations about the cooling zones are peculiar of potassium or if they are more general, I calculated the zones positions for different values of the parameter Δ/Γ. In Fig.5.3 are reported the calculated positions of the various working zones of the cooling process for the hyperfine structure of ^{39}K by artificially changing Γ. We see that for $\Gamma > \Delta$, the zones merge and disappear. The cooling can ,in this case, be performed for any detuning. This is in agreement

[1]a - means that the force is opposite to the atomic velocity, determining friction, a + instead determines acceleration of the cloud to higher velocities. The sign in the low velocity regime is given first

with experiments performed on Sr[51], in which sub-Doppler cooling is performed for $\Gamma > \Delta$. As one can notice from the graph, the lines become horizontal for large hyperfine splitting Δ, effectively predicting the presence of the zones even in the case of large hyperfine structures. In a typical MOT operation, however, the kind of orientational cooling one has in the pure $\sigma^+ - \sigma^-$ configuration of the cooling beams polarizations coexists with Sysiphus cooling. The latter cooling mechanism dominates at large detuning[25]. The relevance of such cooling zones is therefore restricted to the case $\Gamma \lesssim \Delta$.

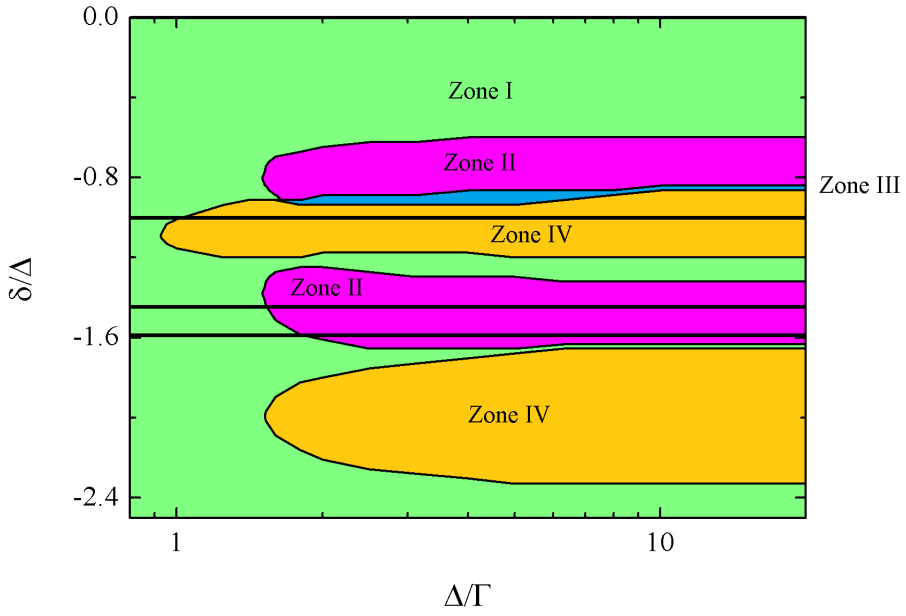

Figure 5.3: Behavior of the cooling zones by changing Γ artificially. Black horizontal lines indicates the position of the atomic levels. In zone I (green) Doppler and sub-Doppler forces can be exploited. Zone II (purple) allows sub-Doppler cooling only after pre-cooling. In zone III (Blue) the force cannot determine any cooling. Finally in zone IV (orange) Doppler cooling can be performed while sub-Doppler cannot. We see that the zones disappear as soon as $\Delta < \Gamma$. The zones show also a nontrivial power dependence. The graph was calculated for $I = I_s$.

Let us try to understand the physical origin of the cooling zones. The zones are a manifestation of the fact that, when a laser is tuned in between two atomic levels, its detuning will be positive for one transition and negative for the other. What happens if the detuning from one of the two levels is much smaller than the detuning from the other is clear, but for intermediate values the situation can be more complicated. Let us consider the situation of only two levels contributing to the force and let us try to estimate the flipping point for the Doppler force. Recalling eq.2.14, and assuming that the total force will be given simply by the sum of the two forces originated by the coupling with the two levels, we have:

$$\alpha_1 - \alpha_2 = \hbar k^2 \Omega^2 \Gamma \left(-\frac{\delta}{(\delta^2 + \Gamma^2/4)^2} + A \frac{\Delta - \delta}{((\Delta - \delta)^2 + \Gamma^2/4)^2} \right) = 0 \tag{5.4}$$

for the detuning that determines the flipping point of the Doppler part of the force, and thus the separation between zone I and zone II. By Δ, I have indicated the energy difference between the two levels and the parameter A is the ratio of the Clebsh-Gordan factors for the two transitions contributing to the cooling. The solution of this equation for large detuning $\delta \gg \Gamma$ is

$$\delta = -\frac{\Delta}{1 + \sqrt[3]{A}} \tag{5.5}$$

Giving $\delta = -0.64\Delta$ for the F'=3 and F'=2 excited levels of the D2 line of potassium. The full simulation prediction is -0.6Δ. For the sub-Doppler part of the force, we can repeat the same argument but using eq.2.23 in order to calculate the flipping point and thus the border between zone II and zone IV.

$$\alpha_1 - \alpha_2 = \hbar k^2 \Gamma \left(-\frac{\delta}{(\delta^2 + \Gamma^2/4)} + B \frac{\Delta - \delta}{((\Delta - \delta)^2 + \Gamma^2/4)} \right) = 0 \tag{5.6}$$

The parameter B is calculated as follows:

$$B = \frac{CG_2 CG_1^R}{CG_2^R CG_1} \tag{5.7}$$

In which CG stands for Clebsh-Gordan coefficient of the two levels (1 is the red detuned one and 2 the blue detuned one) the superscript R indicate the Raman coupling described in chapter 2. The solution to eq. 5.6 for large detuning is:

$$\delta = -\frac{\Delta}{1+B} \tag{5.8}$$

giving $\delta = -0.9\Delta$ for the same transition considered before. Again in good agreement with the value provided by the full simulation, namely -0.84Δ. The systematic shift towards the blue of both boundaries with respect to the simple estimation can be ascribed to the presence of the other levels strengthening the contribution of the blue detuned part of the forces.

5.1.2 Sub-Doppler laser cooling of potassium

In most experiments the cooling is performed in zone I. In the potassium case, in order to decrease rescattering effects by increasing detuning we are forced to work in zone II. The very high initial temperature of the cloud (on the order of a mK) disfavors direct cooling in this zone because of the heating of the hotter atoms that can be determined by the behavior of the force for large velocity. In this case a pre-cooling can allow to keep all the atoms inside the velocity region in which the force is opposite to velocity and achieve efficient cooling. This is the first ingredient of our cooling strategy and it consists of the application of a linear ramp on the cooling parameters. From an initial condition of low detuning (zone I) and high power, to favor Doppler pre-cooling, we go to a final optimized condition for sub-Doppler cooling, with δ in zone II and low intensity (details are given in Sec.5.4.3).

The second ingredient is the application of a dark molasses scheme, in which the low repumping beam intensity causes the atoms to occupy preferentially the F=1 ground state, with only a small fraction of them in the F=2. The F=1 is a dark state for the cooling light and therefore atoms in this state cannot absorb the rescattered

cooling photons. This expedient allows to suppress heating from multiple scattering events. In Fig.5.4, the effect of the repumping beam intensity is shown. For large density the repumping intensity has to be kept very low (on the order of $0.01 \times I_s$) in order to achieve low temperatures. For low density, instead, the repumping power is not important. In potassium, thanks to the narrow hyperfine structure an effective depumping rate of the cooling transition is present. The realization of a dark molasses is therefore easier than in other systems. In atomic systems with large hyperfine splitting, the implementation of a dedicated depumping beam is necessary to operate the dark molasse[48].

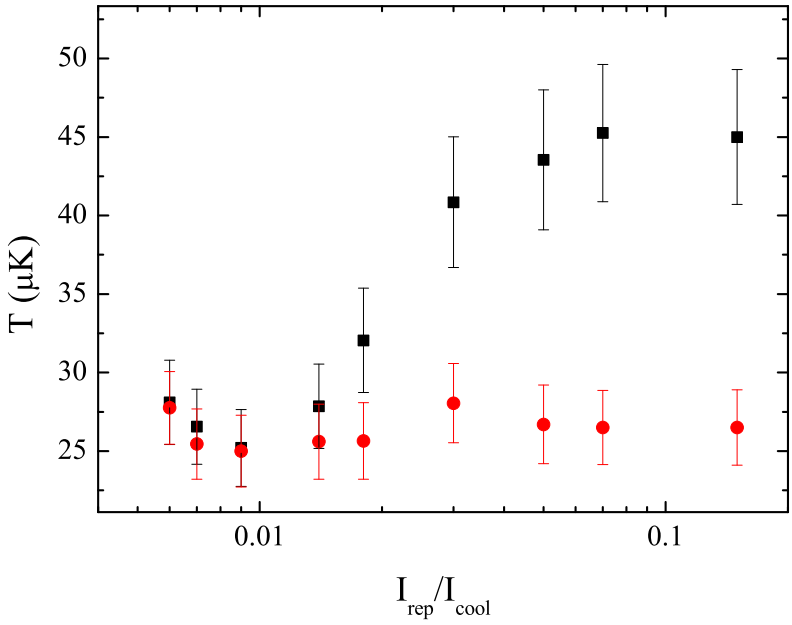

Figure 5.4: Effect of the repumping/cooling power ratio on the achieved temperature for ^{39}K. For the red dots the density was 8×10^8 atoms/cm^3, while for the black squares it was 4×10^{10} atoms/cm^3. In the last case, extra heating caused by rescattered photons can be reduced allowing atoms to stay in the dark F=1 state

We applied this technique to the two bosonic potassium isotopes with similar results, the achieved temperatures are shown in Fig.5.5. The best achieved temper-

atures are the lowest reported values up to now for laser cooling of these two atoms, and are around 25(50) μK for ^{39}K (^{41}K). The agreement with the theory is satisfactory even though the experiment is performed in a 3D-MOT while the theory is carried out in 1D. In conclusion, by the application of a dark molasses scheme and an adiabatic ramping of the cooling parameters, we were able to demonstrate sub-Doppler cooling of potassium. The cooling is efficient even very close to resonance and at high densities thanks to the lossy nature of the cooling transition employed.

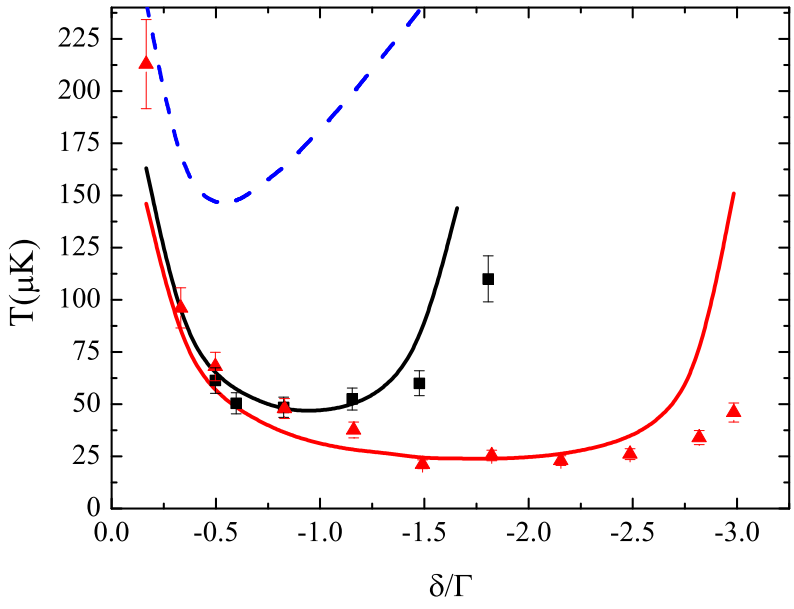

Figure 5.5: Measured temperatures for ^{39}K (red triangles) and ^{41}K (black squares), by using the dark molasses plus ramping technique described in the text. Calculated temperatures (lines) vs the cooling laser detuning. The dashed line is the prediction of Doppler theory.

5.2 Imaging techniques

Before discussing the MOT operation and the operational parameters I describe our imaging techniques which we used to determine the atomic sample parameters. Different imaging techniques are used in order to measure the physical parameters of the atomic samples. In the 3D-MOT chamber usually fluorescence imaging is employed, while in the science chamber the main applied technique is absorption imaging.

5.2.1 Fluorescence imaging

In the 3D-MOT chamber, the imaging is performed by switching on the MOT beams at full power, for a very short time τ, and collecting the light emitted by the atoms with a lens placed outside the chamber. The image of the sample is thus reproduced onto a CCD camera with a magnification of 0.31. The magnification was measured comparing the position of the cloud in free fall with Newton law and assuming g=9.81 m/s^2.

The total power emitted by the atoms driven by a laser field, detuned from the resonance by δ and with intensity I, is given by

$$P = N\frac{\Gamma}{2}\frac{I/I_s}{1+I/I_s}\frac{1}{1+4\delta^2/\Gamma_{eff}^2}\hbar\omega \tag{5.9}$$

where $\Gamma_{eff} = \Gamma\sqrt{1+I/I_s}$ is the power broadened line-width. The saturation intensity has to be determined experimentally since neither the cooling light nor the atoms are polarized. We estimated it to be about 4 times larger than the nominal value. Nevertheless, due to the the very high intensity employed (on the order of $30I_s$), we can always consider the transition fully saturated ($I/I_s \gg 1$). Due to the high density of the sample, sometimes out-of-resonance imaging has been utilized to get reliable measurements.

The light is emitted randomly in all directions and only a fraction $\frac{\Omega}{4\pi}$ is collected by the imaging lens. The solid angle Ω is estimated to be 4×10^{-3} srad. In order to avoid exposure of the CCD to the room light, we have placed an interferometric filter in front of it. We have calibrated the power response of the CCD and the filter by shining a laser beam of known power. The signal on a single CCD pixel camera is found to be

$$S = \alpha G P \frac{\Omega}{4\pi} \tau \tag{5.10}$$

the prefactor α=8.4×10^{15} $\frac{counts}{Ws}$ is the result of the calibration. G is the gain of the camera, which can be set by the operator. The number of atoms is then found by inverting the previous expressions and integrating the signal over the whole CCD. The size of the cloud is found by fitting the CCD image with a 2D gaussian function. For the CCD camera we use a Stingray F-145B/C from Allied Vision Technology.

5.2.2 Absorption imaging

Imaging in the glass cell is performed by shining a laser on the atoms and by recording the image of the absorbed beam $I_{out}(\mathbf{r})$ onto the CCD. A subsequent image is taken without atoms, the intensity in this case is indicated as $I_{in}(\mathbf{r})$. We infer the cloud density from the ratio of the two images via the Beer-Lambert law for the absorption. For this imaging system we always work with $I/I_s \ll 1$. In this case, the column density of the atomic cloud can be obtained as

$$n_{2D}(\mathbf{r}) = \frac{\ln(I_{in}(\mathbf{r})/I_{out}(\mathbf{r}))}{\sigma} \tag{5.11}$$

where σ is the scattering cross section for the imaging light, which can be expressed as

$$\sigma = \frac{3\lambda^2}{2\pi} \frac{1}{1+\frac{4\delta^2}{\Gamma^2}} \quad . \tag{5.12}$$

The atomic parameters are then extracted from the images by fitting the density distribution with the theoretical profile.

5.3 2D-MOT flux characterization

The 2D-MOT flux was measured by recording the fluorescence signal of the atomic beam. The velocity distribution of the atoms was also measured by switching off the 2D-MOT and measuring the time of flight delay of the fluorescence signal [52]. The results are reported in Fig.2.6. The 2D-MOT can provide a total integrated

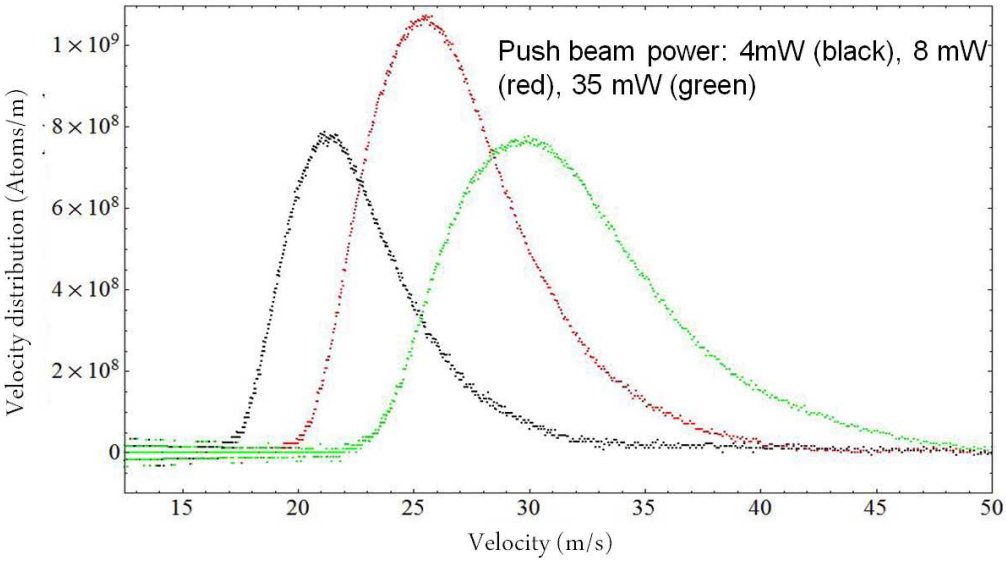

Figure 5.6: 2D-MOT atomic beam axial velocity distribution as measured from time of flight delay of the fluorescence signal. Acting on the push beam power the average velocity of the beam can be changed. The integrated flux can be as large as 2×10^{10} atoms/s. The average velocity of the beam can be as low as 25 m/s. High flux and low velocity are desirable in order to maximize the capture rate of the atomic beam by the 3D-MOT.

flux up to 2×10^{10} atoms/s with a low average velocity of around 25 m/s. The low velocity is desired in order to be able to capture the atoms into the 3D-MOT.

	δ_C/Γ	δ_R/Γ	I_{main}/I_s	I_R/I_C	I_{push}/I_s	I_+/I_s	$\gamma(G/cm)$
2D-MOT	-5.7	± 0	35	0.8	13	5	13

Table 5.1: Experimental parameters used for the 2D-MOT operation. δ_C is the detuning of the cooling light from the cooling transition $F = 2 \rightarrow F' = 3$. δ_R is the detuning of the repumping light from the repumping transition $F = 1 \rightarrow F' = 2$. I_{main} is the intensity of the main beams for the transverse cooling; I_C (I_R) is the cooling (repumping) beam's intensity; I_{push} is the intensity of the push beam; I_+ is the intensity of the additional retarding beam; γ is the magnetic field gradient.

5.4 3D-MOT operation and further cooling procedures

The 3D-MOT operation is broken down into its main components, each of them has its purpose and it is optimized for a specific goal. The whole sequence was optimized extensively during the second year of my PhD (see also[53]). The first building block is the loading from the 2D-MOT atomic beam. In this part, we are mostly concerned about atom number and loading time. The second part (compressed MOT) maximizes the density of the sample. Finally, the molasses sequence, is optimized to achieve the lowest temperature of the atomic sample.

5.4.1 3D-MOT loading from the atomic beam

In Fig.5.7 a typical instance of the 3D-MOT loading is depicted. The relevant experimental parameters for the loading are listed in Tab.6.2. The maximum achieved number of atoms is close to 3×10^{10}. The initial loading rate compared to the measured total 2D-MOT flux gives a capture efficiency of about 65 %. The curve shows a clear saturation after about 2-3 s. Since the measured lifetime of the

	δ_C/Γ	δ_R/Γ	I_{tot}/I_s	I_R/I_C	$\gamma(G/cm)$
Loading	-3	-3.3	35	0.8	11

Table 5.2: Experimental parameters used during the 3D-MOT loading. I_{tot} is the total intensity of the 3D-MOT beams.

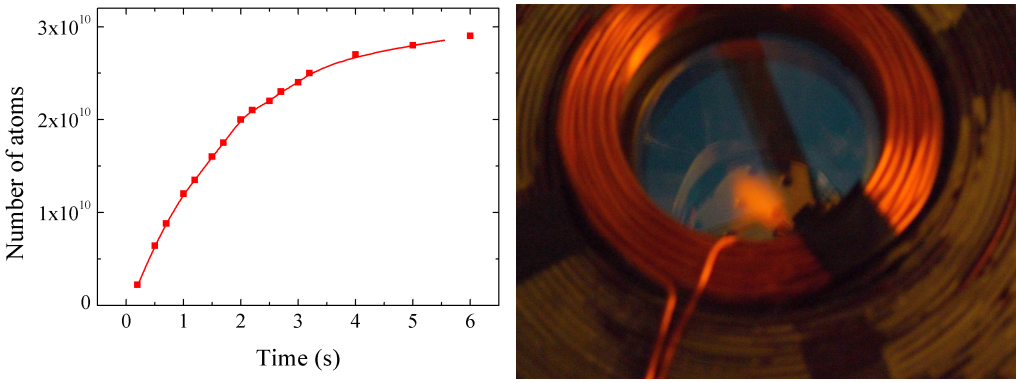

Figure 5.7: Picture of the atomic cloud as seen by naked eye from above the 3D-MOT cell (right). Loading curve of the 3D-MOT trap (left). The achieved maximum number of atoms is about 3×10^{10} atoms after 6 s. In the normal operation, we limit the loading time to 5 s. The initial slope corresponds to about 1.3×10^{10} atoms/s. If we compare to the total flux provided from the 2D-MOT beam, the capture efficiency can be calculated to be 65 %.

cloud in this cell is only 4 s, we ascribe this saturation to background collisional losses. Immediately after the loading, we have measured the atomic density and the temperature to be 1.8×10^{10} atoms/cm^3 and 2 mK respectively. The achieved phase space density is, therefore, 4.6×10^{-9}. The loading of the 3D-MOT, together with the evaporation, is one of the most time consuming parts of the experiment. In order to increase the repetition rate, a very high loading rate is therefore desirable. The MOT loading is optimized to provide high atom number in the lowest possible time. The phase space density ρ is however too low to load efficiently in the magnetic

trap. We have therefore to compress the MOT and to perform sub-Doppler cooling in a molasses scheme. In tab 6.2 the main experimental parameters are reported.

5.4.2 Compressed-MOT

During the Compressed-MOT (C-MOT) the cloud gets compressed by the effect of the cooling light. To achieve the maximum compression we have to decrease the repumper power and increase the laser detuning. Although this procedure might seem counterintuitive, it is determined by the fact that the density in the MOT is limited by light assisted collisions (see Fig.5.1) which prevents the atoms to get too close. To increase the density, we have thus to decrease the photon scattering rate.

This is done in a first sudden change of the MOT parameters (the new parameters are kept constant for 5 ms) followed by an adiabatic linear ramp (10 ms duration), to the final values. The compressed state is a non equilibrium one, if kept for too long,

	δ_C/Γ	δ_R/Γ	I_{tot}/I_s	I_R/I_C	$\gamma(G/cm)$
initial values (kept for 5 ms)	-3.7	± 0	35	0.5	15
adiabatic ramp (10 ms long)	-3.7 to -6.2	± 0	35	0.5 to 0.02	15

Table 5.3: experimental parameters used during the C-MOT.

it leads to atom losses from the cloud. For the chosen time the losses were about 25 %. The number of atoms at this point is 1.8×10^{10}, the density has increased to 1.7×10^{11} atoms/cm^3 and the temperature is 2 mK. the phase space density ρ is thus 4.2×10^{-8}.

5.4.3 Molasses and sub-Doppler cooling

The molasses sequence is the most critical and the most important part of the cloud preparation. First of all, a fine tuning of the stray magnetic fields to zero is necessary

in order to achieve low temperatures. We have indeed verified that a field of about 1 G prevents us to reach sub-Doppler temperatures. Another subtle point is the power balance of the beams which has to be optimized for this phase, since the nulled magnetic field does not provide any longer the trapping force. The cooling is done by adiabatically increasing the detuning from zone I to zone II of the sub-Doppler force and, at the same time, ramping down the intensity. The ramp is 10ms long. The results are given in Fig.5.8, in which is also reported a comparison to the case without the ramp.

	δ_C/Γ	δ_R/Γ	I_{tot}/I_s	I_R/I_C	$\gamma(G/cm)$
initial values	-0.7	-2.7	18	0.01	0
adiabatic ramp (10 ms long)	-0.7 to -2.5	-2.7	18 to 1	0.01	0

Table 5.4: experimental parameters used during the molasses cooling.

In the two cases, the achieved temperature is similar but substantial atom losses are observed if the ramp is not performed. The atom lost with the ramping strategy were only 10 %. Without the ramp, the cloud shows a bimodal distribution in velocity space (fig.5.9). The reported efficiency in fig.5.8 refers to the central peak of the velocity distribution. We interprete this bimodal structure to be originated from the nature of the cooling force in region II, the hotter tails have been effectively accelerated by the cooling force. The expansion of the hot part is not consistent with an expansion from $v = 0$, since the force, and therefore the cloud, is not equilibrated.

The final number of atoms is thus 1.65×10^{10}, the density is also lower than in the C-MOT due to the free expansion of the cloud. By performing a measurement of the diffusion of the cloud in the molasses beams we have found that the cloud reaches the diffusing regime in about 3 ms. Before entering the diffusive regime, the cloud expands almost ballistically. We can estimate its size after the initial free

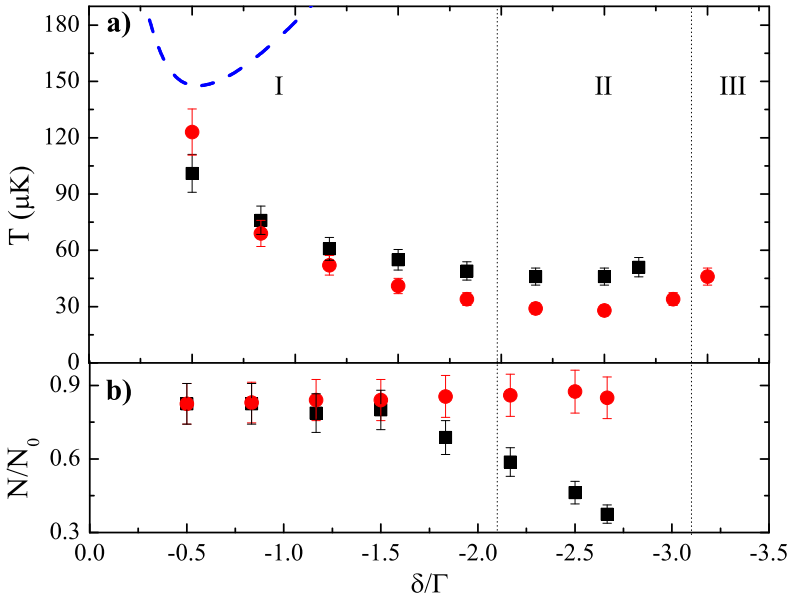

Figure 5.8: Reached temperature and atom number efficiency of the molasses sequence as a function of the final detuning. Black squares are without ramp and red triangles are with ramp. The blue dashed line is the Doppler theory.

expansion by the law

$$\sigma^2(t) = \sigma_0^2 + \frac{k_B T}{3m} t^2 \tag{5.13}$$

with σ_0=1.9 mm and T=2 mK[2] Eq.5.13 gives σ=2.21 mm. After the initial ballistic expansion, the cloud expands in a viscous media (the molasses) in a diffusive way. We have measured the diffusion constant to be D=0.35 cm^2/s. The final size σ can then be calculated from

$$\sigma^2(t) = \sigma_0^2 + 2Dt \quad , \tag{5.14}$$

giving σ=2.32 mm. This increase in the size corresponds to an overall density drop

[2]in the formula the temperature is divided by three to take into account that T is decreasing during the expansion. We assume a linear dependence of the temperature on time and a final temperature negligible with respect to the initial one. The result then comes from integration of $\frac{d\sigma}{dt} = \frac{2k_B T(t) t}{m}$. To verify that the final temperature was low I measured the reached temperature after 3 ms to be 70 μK.

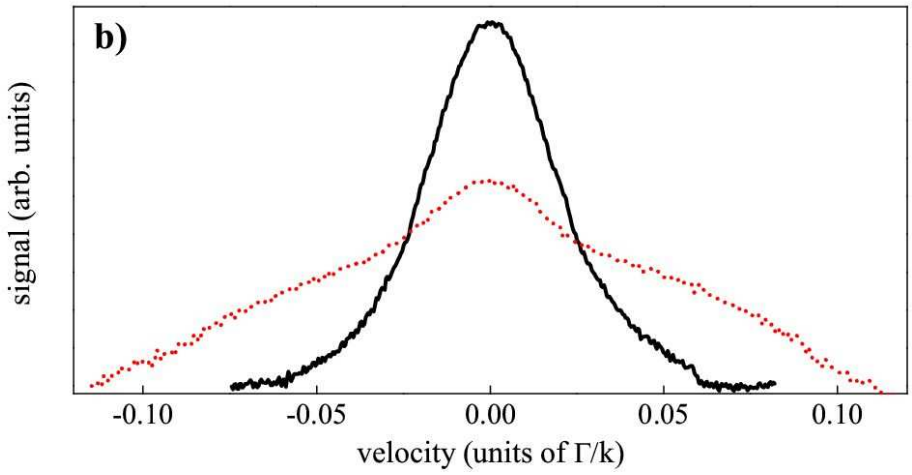

Figure 5.9: Typical instance of the velocity distribution of the atomic cloud with (black) and without (red) the ramping strategy.

of a factor 1.8, consistent with the measured density after the molasses. We notice that the size increases mostly during the initial part of the cooling ramp. The length of the sequence, therefore, does not influences the final size so much. The final density is 8×10^{10} atoms/cm^3 and ρ is 1.5×10^{-5} for the optimized temperature of 25 μK.

Chapter 6

Bose-Einstein condensation of ^{39}K

In this chapter I describe the implementation of the remaining steps necessary for the realization of the BEC. I start by revising the possible routes to BEC for ^{39}K. The main problem is the negative background scattering length (as for ^{85}Rb), that leads to the Ramsauer-Townsend minimum in the collisional cross section (see Sec.2.3.1).

A clever way to overcome this problem was the implementation of sympathetic cooling with ^{87}Rb. This technique relies on the good scattering properties of ^{87}Rb and on thermalization with ^{39}K. A big problem of this technique is, however, the very high degree of complexity of the experimental apparatus, because of the two species operation. In addition, the need of having a much larger number of Rb atoms than the number of K atoms, limits the attainable condensed atom number. Finally, the, usually, long preparation time (on the order of a minute) of the BEC makes this not the best choice if high repetition rate is required.

Another condensation strategy consists in the employment of Feshbach resonances in order to change the scattering properties of the gas, allowing for singles species operation. Interaction tuning cannot be performed in a magnetic trap due to the spatial variation of the magnetic field. The gas needs therefore to be transferred to an optical dipole trap. The achievement of efficient evaporative cooling by means

of a Feshabch resonance was already demonstrated and exploited for the realization of K BECs[54, 55]. It was, however, employed in combination with sympathetic cooling and never as a stand-alone technique.

We chose to follow this last strategy. To transfer the atoms to the science chamber, we need, initially, to trap them into a magnetic trap. The atoms will then be found in a magnetic trap in the science chamber and RF evaporation can be performed. The atoms are afterwards transferred into a dipole trap in which Feshbach assisted evaporative cooling down to qiuantum degeneracy will be realized. A fundamental choice is the one regarding which Feshbach resonance to exploit and which magnetic energy level is the most convenient to work with. In Fig.6.1 is depicted the magnetic field dependence of the atomic energy and of the scattering length.

We tried two different strategies: the first one required an initial preparation of the atomic sample into the F=2, m_F=+2 magnetic sublevel in order to exploit its large magnetic dipole moment for magnetic trapping and possibly RF evaporation. Once in the dipole trap, the atoms were transferred to the F=1, m_F=+1 absolute ground state and evaporative cooling performed around 400 G. The second strategy consisted in keeping the atoms from the beginning into the F=1, m_F=-1 magnetic sub-level and perform evaporative cooling in the dipole trap around 40 G. I will briefly describe the details of the two strategies as well as the main results obtained with them.

The advantage of the first strategy consists of exploiting the F=2, m_F=+2 state magnetic moment in order to achieve higher density and collision rate with a fixed magnetic gradient (which is limited by the maximum current provided by the coil's power supply). This, in principle, leads to the possibility of RF evaporative cooling in the magnetic trap. This evaporative cooling reached its limit for temperatures around 100 μK due to the Ramsauer-Townsend effect (see the next section). This choice presents many hinders. First of all, our atomic cloud after molasses cooling

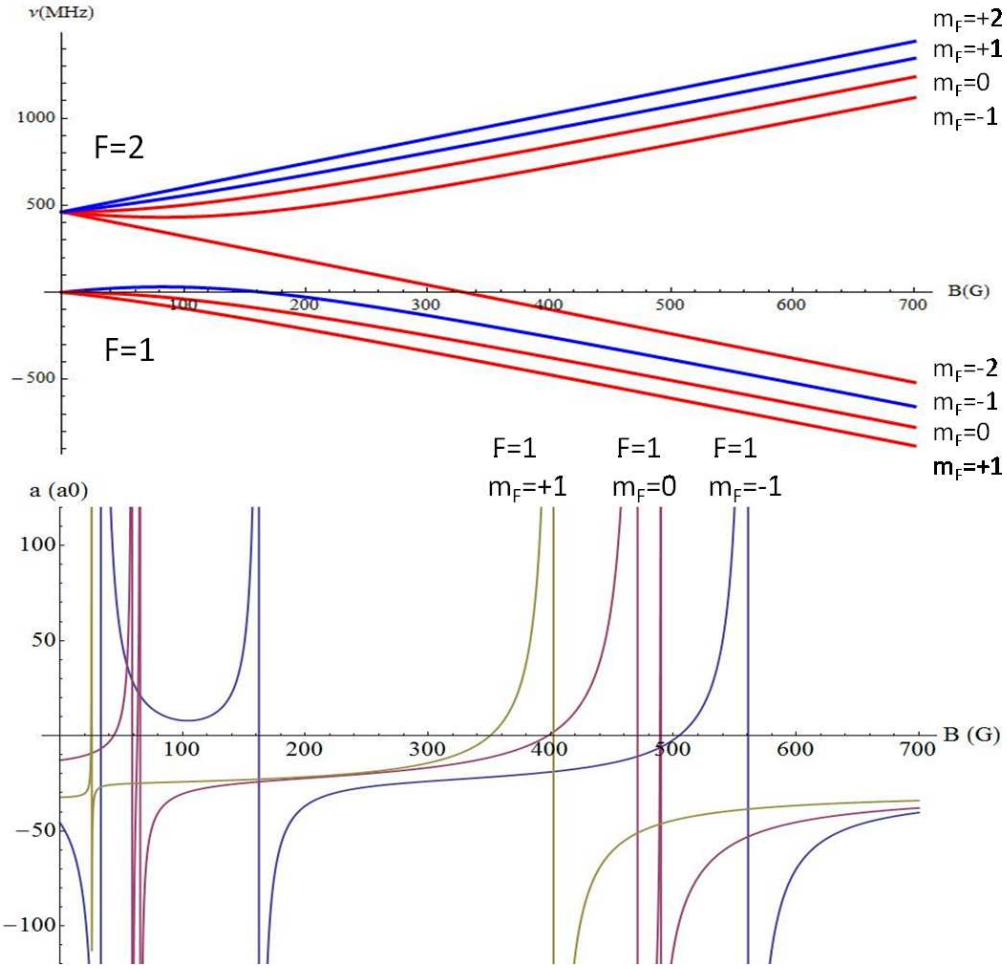

Figure 6.1: Magnetic field dependence of the energy of the various ground state magnetic sublevels of ^{39}K (upper panel). The blue lines corresponds to trappable states at low field. The states are labeled by the value of F and m_F at low field. For fields higher than 50 G a partial Paschen-Back picture would be more appropriate (J is still a good quantum number while F is no more). On the lower panel, the dependence of the s-wave scattering length versus magnetic field is depicted for the three magnetic sublevels with F=1: m_F=1 (yellow-green), m_F=0 (purple), m_F=-1 (blue).

mainly consists of atoms in the F=1 state because of the dark molasses scheme, which is part of our sub-Doppler cooling procedure[46]. In order to prepare the atoms in F=2, m_F=+2 state, optical pumping is therefore needed. We performed optical pumping on the atomic sample after molasses cooling. However, we experienced a substantial heating of the sample (about a factor two in temperature) and only partial (70 %) atomic orientation. Once the atoms are in the dipole trap, they must be transferred to F=1, m_F=+1 via a radio frequency transition. This was possible even though, due to the high temperature of the gas, the efficiency was not high. We could not get more than 50 % of the atoms in the desired state. The untransferred atoms were acting as a thermal load on the main cloud, leading to inefficient evaporative cooling. The last problem was that, due to the duration of the sequence and to the employment of a high magnetic field Feshbach resonance, a substantial heating of the magnetic field coils was present, causing drifts in the magnetic field at the position of the atoms. We obtained a BEC wth around 10^4 atoms in the condensate using this strategy. The evaporative cooling time was 30 s (10 s for the RF evaporation plus 20 s for optical evaporation) and thermal effects on the coils affected the experimental stability.

In order to increase the atom number and improve the experimental stability we decided to work from the beginning with atoms in the F=1, m_F=-1 state. This state cannot be easily optically pumped. Approximately 33 % of the initial atoms in the MOT will populate this state. The rest of the atoms will populate high field seeking states and will, therefore, be ejected from the magnetic trap. The lower magnetic moment diminishes the achievable density. Therefore RF evaporation is inefficient in this case. The advantages are that the state is magnetically trappable at low field and that it has a very convenient low field Feshbach resonance centered at 34 G and 50 G wide. Neither optical pumping nor RF transfer is therefore needed and the heating of the coils can be minimized. This technique allowed for a larger

number of condensed atoms and a higher repition rate of the experiment. The final condensed atom number by this strategy was around 10^5 and the evaporative cooling was performed in about 10 s.

6.1 RF evaporation and Ramsauer-Townsend minimum

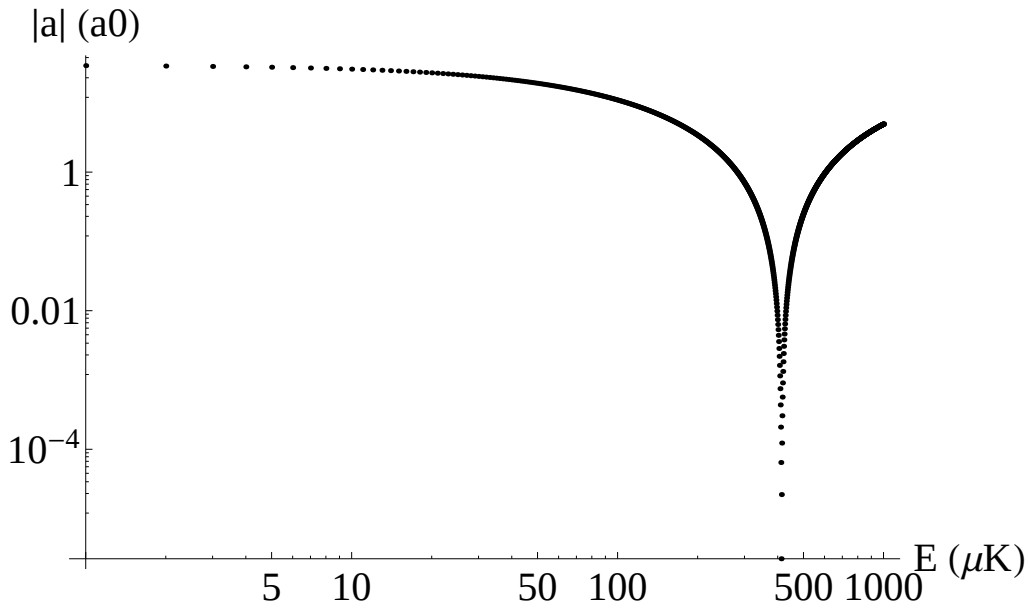

Figure 6.2: Calculation of the scattering cross section as a function of the collision energy in the center-of-mass frame for two atoms colliding in the $F = 2, m_F = +2$ state[56]. The reported value is an "effective" scattering length $a = \sqrt{\sigma/(8\pi)}$. The data shown the Ramsauer-Townsend effect which reduces the collisional cross-section to almost zero at an energy of 400 μK.

In this section the results of the RF evaporation for the F=2, m_F=+2 state are presented. The RF evaporation ramp was divided in steps. In each step the frequency was reduced by a factor two with respect to the initial value and the du-

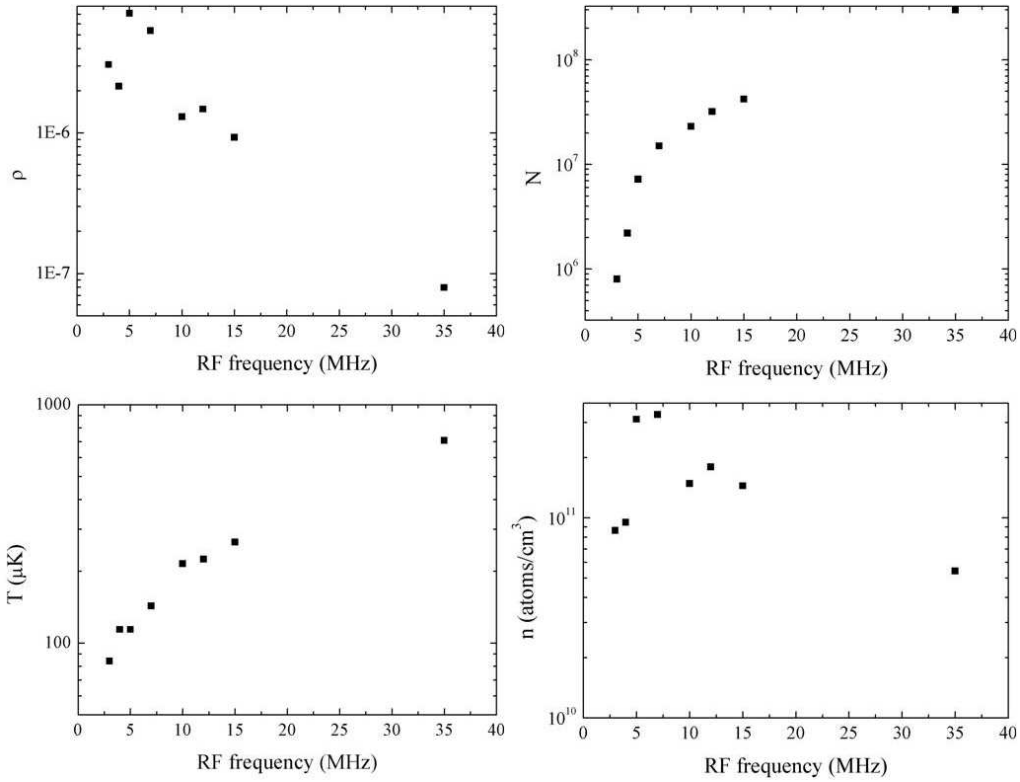

Figure 6.3: Results of the RF evaporative cooling for atoms in the $F = 2, m_F = +2$. The evaporation stops around 100 μK.

ration of each step was optimized by maximizing the achieved phase space density. The resulting ramp was linear and lasted 20 s, during which the atoms were held in a quardupole trap with a magnetic field gradient of 276 G/cm along the vertical direction. In Fig.6.2 is reported a numerical calculation[56] that shows the scattering cross section for two atoms in the F=2, m_F=+2 state as a function of their collisional energy in the center-of-mass frame. The calculation shows the presence of the Ramsauer-Townsend minimum around 400 μK. For this reason, we expect that, for similar temperatures, the thermalization will be inhibited and the RF evaporation will stop. This is shown clearly by the results of the evaporative cooling in Fig.**??**. For temperatures of the sample around 100 μK, the evaporation efficiency goes to zero, meaning that, reducing the RF frequency, more atoms are lost without

increasing the phase space density. In order to continue the evaporative cooling, the atoms are transferred to the optical trap. In the following sections, the details of the experimental sequence for atoms in F=1, m_F=-1 are described for which RF evaporation was not performed.

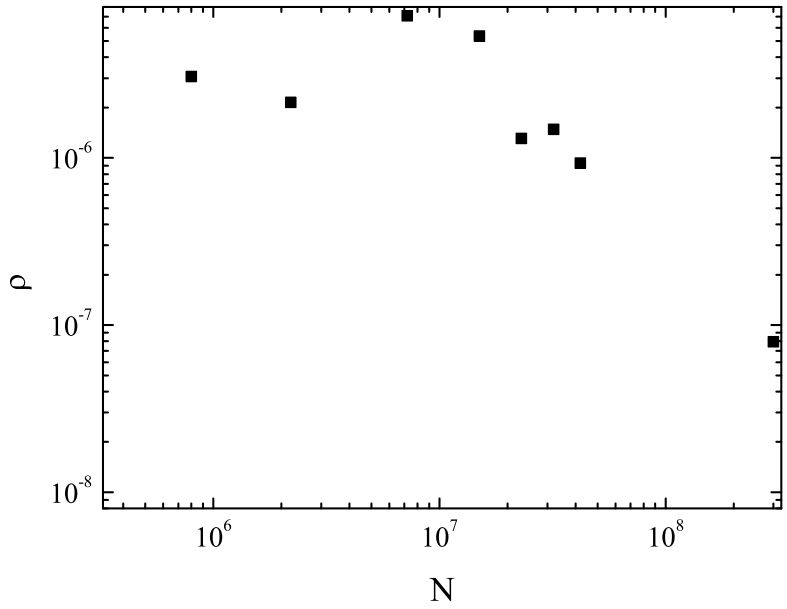

Figure 6.4: Phase space density versus number of atoms for the RF evaporation. The efficiency goes to zero at the end of the evaporation.

6.2 Magnetic trap loading

Once the sample has been cooled in the molasses, we switch on abruptly a quadrupole trap in which we load the atoms. Only the low field seeking atoms get trapped in this way. Since the majority of the atoms populates the F=1 hyperfine state, the trapping efficiency will be about 1/3. The magnetic field gradient γ at the switching on has to be chosen in order to maximize the phase space density of the cloud. If the gradient is too high, the cloud will receive too much potential energy and heat up. If, on the contrary, the gradient is too low, the cloud will lose density. Since our

cloud is big (high potential energy) and cold, the optimum value of the magnetic gradient is going to be small and the magnetic energy may be comparable to the gravitational energy. In the following, I will calculate the optimal gradient in the presence of gravity. In the initial situation we have a cloud with temperature T, with a given size σ. Its density will be, therefore:

$$n_i(x,y,z) = \frac{N}{(2\pi)^{3/2}\sigma^3} e^{-\frac{x^2+y^2+z^2}{2\sigma^2}} \quad . \tag{6.1}$$

The gain in potential energy due to the switching on of the magnetic trap will be given by

$$U = \langle \frac{\mu_B}{2} B \rangle = \frac{\mu_B \gamma}{2} \int \sqrt{\frac{x^2+y^2}{4} + z^2} n_i(x,y,z) d^3x \quad . \tag{6.2}$$

This integral gives the result

$$U = 17.34 \frac{\mu_B \gamma N \sigma}{2(2\pi)^{3/2}} \tag{6.3}$$

The total energy of the cloud at this point will be $E = U + K_i$. Here K_i is the initial kinetic energy given by $K_i = \frac{3}{2} N k_B T$. After a certain time the cloud will come to an equilibrium in the trap. Since the trap has a potential, which depends linearly on the distance to the center, the virial theorem gives, for the final kinetic energy, $K_f = \frac{E}{3}$. From the final kinetic energy we can find the final temperature T_f as

$$T_f = \frac{2K_f}{3k_B N} = \frac{T}{3} + \frac{17.34 \mu_B \gamma \sigma}{9 k_B (2\pi)^{3/2}} \quad . \tag{6.4}$$

The final central density $n_f(0)$ in the magnetic trap can be estimated by the equation

$$N = 2\pi n_f(0) \int e^{-\frac{\mu_B \gamma / 2 \sqrt{r^2/4 + z^2} + mgz}{k_B T_f}} r dr dz \tag{6.5}$$

the result of the calculation is:

$$n_f(0) = \frac{N}{32\pi} \left(\frac{\mu_B \gamma}{2 k_B T_f} \right)^3 \left(\left(\frac{2mg}{\mu_B \gamma} \right)^2 - 1 \right)^2 \quad , \tag{6.6}$$

which makes sense only if $\gamma > \gamma_{min}$, with γ_{min}=11.4 G/cm being the minimum required gradient in order to hold the cloud against gravity. We can now calculate

the final phase space density as

$$\rho_f = n_f(0)\lambda(T_f)^3_{dB} = \frac{\mu_B^3\gamma^3h^3\left(\left(\frac{2mg}{\mu_B\gamma}\right)^2-1\right)^2 N}{512\sqrt{2}\pi^{5/2}m^{3/2}\left(\frac{k_BT}{3}+0.122\gamma\mu_B\sigma\right)^{9/2}} \quad . \tag{6.7}$$

By comparing this formula with

$$\rho_i = n_i(0)\lambda(T)^3_{dB} = \frac{Nh^3}{(2\pi)^3\sigma^3m^{3/2}(k_BT)^{3/2}} \quad , \tag{6.8}$$

we can calculate their ratio α to be

$$\alpha = \frac{\rho_f}{\rho_i} = 0.02\frac{(\mu_B\gamma\sigma)^3\left(\left(\frac{2mg}{\mu_B\gamma}\right)^2-1\right)^2(k_BT)^{3/2}}{\left(\frac{k_BT}{3}+0.122\gamma\mu_B\sigma\right)^{9/2}} \quad . \tag{6.9}$$

The maximum value of α is obtained for $\gamma \gg \gamma_{min}$ and it is α_{max}=3.26. This means that, if the switching on is done properly, ρ can increase (of course this calculation does not consider atom losses). This is caused by the change in shape of the trapping potential, from parabolic in the MOT to linear in the quadrupole. By maximizing α with respect to γ we find the result of Fig.6.5.

For large values of T/σ the optimized value of γ follows a linear dependence given by γ(G/cm)=0.812 T(μK)/σ(mm), that can be found in the limit $\gamma \gg \gamma_{min}$. When the optimum value of γ becomes of the order of γ_{min}, there is a deviation from the simple linear dependence. The value of α obtained for the optimized value of γ also decreases when we get closer to γ_{min} as is shown in fig.6.6.

In our case, the size of the cloud is 2.35 mm and the temperature 25 μK, the calculation gives, for the optimized value of γ, 30 G/cm and, for the phase space density increase, α=1.1. We notice that, obtaining an even lower temperature in the molasses, ρ will decrease once we load the cloud into the magnetic trap. In other words, the gain in phase space density derived from further cooling is lost in the loading of the magnetic trap. The maximum achievable phase space density after loading (considering a cloud cooled down to T=0 before loading) scales like

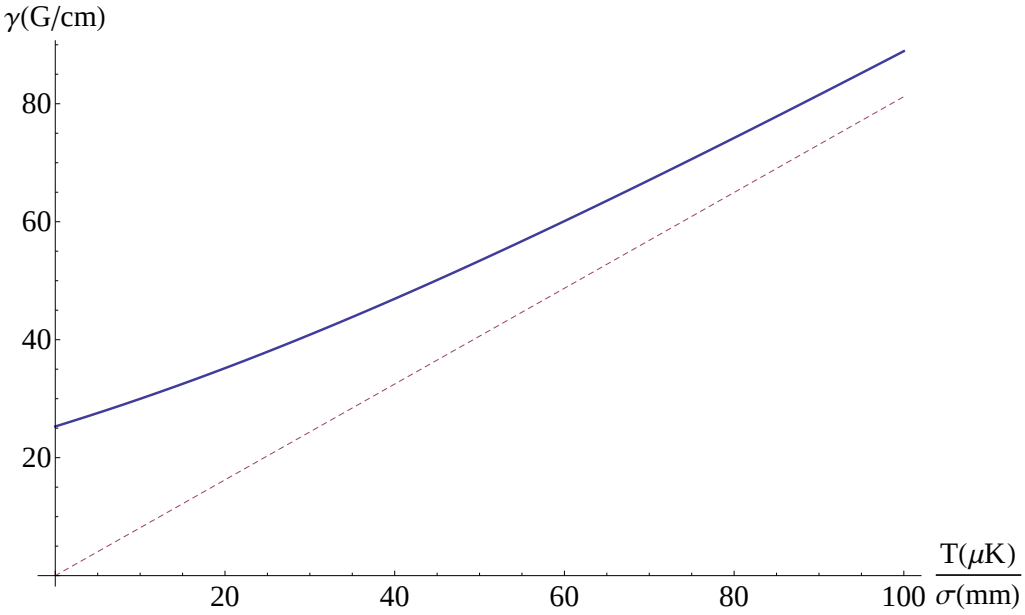

Figure 6.5: Optimized value of γ with respect to T/σ in order to maximize the phase space density of the cloud in the quadrupole. Calculation with (blue solid) and without (red dashed) gravity.

$\sigma^{-9/2}$. The size of the cloud σ is mainly limited by light-assisted collisions in the C-MOT. This represents the limiting factor of the system up to this point. In order to decrease the cloud size, a dark-MOT scheme has to be implemented. The number of atoms loaded into the magnetic trap is 3.8×10^9, the temperature is measured to be 55 μK, the density is 1.8×10^{11} atoms/cm^3 and ρ is 10^{-5}.

6.3 Transfer efficiency

Once the cloud is trapped into the magnetic trap, we ramp up the magnetic field gradient adiabatically to the maximum value of 164 G/cm. The size of the cloud decreases by a factor 1.8 and its temperature increases by a factor 3.1. The coils are then moved towards the glass cell with the motorized translation stage. We do

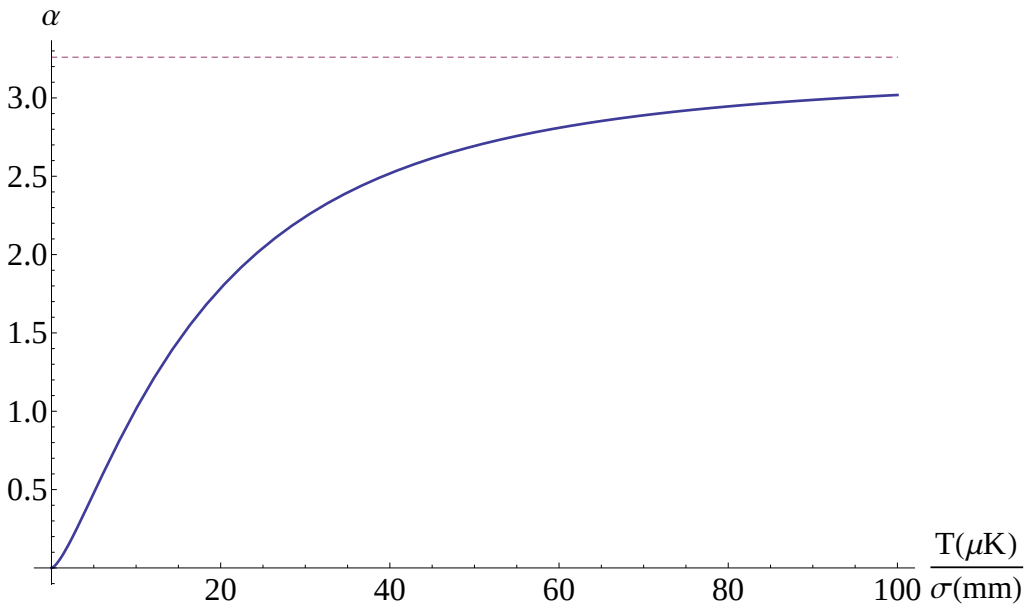

Figure 6.6: value of α obtained for the optimized value of γ as a function of T/σ

not experience any heating due to the transport apart from the adiabatic heating, probably because we transfer a relatively hot cloud. The state F=1, m_F=-1 that the atoms occupy during the transport, has an intrinsic finite trap depth of about 1.5 mK due to the nonlinear magnetic moment of this state. Any increase in the temperature, therefore, causes losses of the higher energy atoms and, possibly, an effective evaporative cooling. This has a considerable effect only if the truncation parameter is 10 or lower i.e. if the temperature is 150 μK or higher.

We tried to characterize the performances of our transport scheme in terms of the fraction of the initial atom number that effectively reaches the glass cell. The first loss mechanism is due to collisions with the background gas. To estimate it we measured the lifetime $\tau(x)$ of the sample at every point during the transport to the glass cell. To do so, we moved the cloud to the desired position, we kept it there for a variable time, and finally we moved it back to the MOT chamber, in which we measured the remaining number of atoms in the trap.

	δ_C/Γ	δ_R/Γ	I_{tot}/I_s	I_R/I_C	$\gamma(G/cm)$
MOT loading	-3	-3.3	35	0.8	11
C-MOT	-3.7	± 0	35	0.5	15
compression ramp	-3.7 to -6.2	± 0	35	0.5 to 0.02	15
Molasses	-0.7	-2.7	18	0.01	0
cooling ramp	-0.7 to -2.5	-2.7	18 to 1	0.01	0
Quadrupole loading	/	/	0	/	30

Table 6.1: Experimental parameters used throughout the preparation of the cloud.

	N	T	n	ρ
		μK	atoms/cm^3	
Loading	3×10^{10}	2000	1.8×10^{10}	4.6×10^{-9}
C-MOT	1.8×10^{10}	2000	1.7×10^{11}	4.2×10^{-8}
Molasses	1.65×10^{10}	25	8.1×10^{10}	1.5×10^{-5}
Quadrupole	3.8×10^{9}	55	1.8×10^{11}	1×10^{-5}

Table 6.2: Final resume table for the cloud preparation up to this point. N is the atom number, n is the peak density and ρ is the phase space density.

The lifetime in the MOT chamber is only 4 s. The lifetime in the science chamber, instead, can reach 80 s. The lifetime in the intermediate region remains of the order of a few seconds up to the science chamber's pumping region. The results of the lifetime measurement are presented in Fig.6.7. It is interesting to notice that the lifetime increases significantly at about 200 mm from the 3D-MOT chamber and then lowers again. In this position, a vacuum valve determines a larger distance of the atomic sample from the apparatus walls. The increase in lifetime cannot be explained just by a lower background pressure, since the lifetime decreases in both directions towards the vacuum pumps, while is reasonable that the pressure

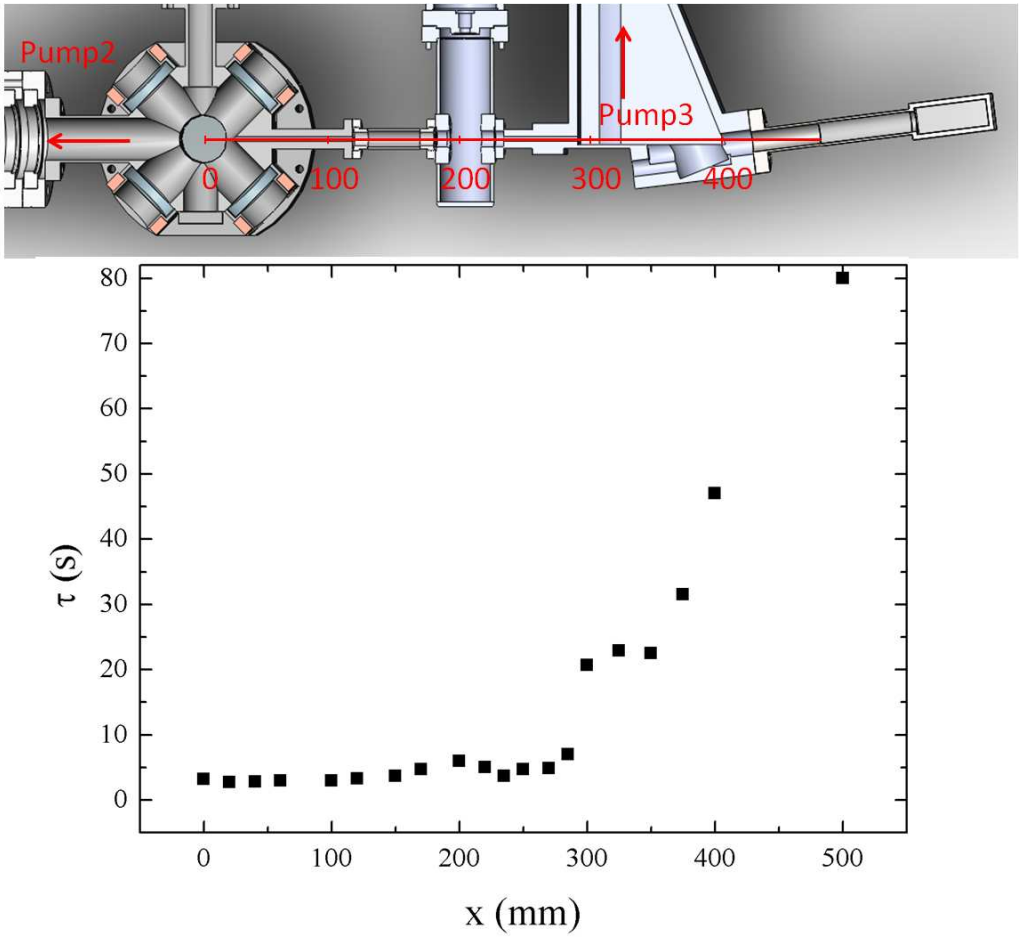

Figure 6.7: Measured value of the lifetime τ as a function of the trap position x (black squares). On the top a cut view of the inside of the vacuum system is presented.

would decrease closer to the pumps. We do not have a clear explanation for this observation. The preparation of the cloud in the MOT chamber takes about 400 ms, in order for the compression ramp to be adiabatic. The losses during preparation are about 13 %. By interpolating the measured lifetime and estimating the losses during the movement of the cloud as

$$\frac{\Delta N}{N} = \int_0^{t_f} \frac{dt}{\tau(x(t))} \quad , \tag{6.10}$$

we get an overall additional loss of 32 % . Where $x(t)$ is the time trajectory of the

moving cart. In total, the loss due to lifetime amounts to 41 % of the initial atom number. The number of atoms measured in the last chamber is, however, only 21 % of the initial atom number. An additional loss of about 50 % can be explained by the cloud passing, somewhere during the transport, very close to an obstacle (one of the vacuum system's walls). Given the magnetic gradient in the trap and the temperature of the cloud, such a loss would be consistent with an obstacle at a distance of 1.5 mm from the center of the trap. Since the atoms lost by such an occurrence are the most energetic ones, the atomic loss can determine cooling after thermalization of the cloud.

6.4 Dipole trap loading from magnetic trap

Once in the final cell, the cloud gets compressed even more to the maximum gradient of about 276 G/cm. The measured cloud parameters at this point are N=8×10^8, T=250 μK, n=4×10^{11} atoms/cm^3, ρ=2.3×10^{-6}. Due to the high temperature, some evaporative cooling due to the compression and the finite depth of the state can be responsible for additional losses (truncation parameter η=6).

For the main dipole trap laser, we used a multimode 100 W IPG laser, while the dimple trap was obtained from a single mode beam derived from a 10 W Nufern fiber amplifier (see Sec. 4.12). The main dipole trap laser (horizontal) has a waist W_0=25 μm and its power is P=30 W. Its depth is therefore 1.4 mK. The vertical dimple laser has a waist of 70 μm and its power is 200 mW, giving additional 3.5 μK. The truncation parameter is only determined by the main dipole trap along the horizontal direction, since the losses are mainly along gravity. Collisions are crucial for the loading of the dipole trap. We decided to employ a very deep trap, in order for the mean energy of the atoms to increase once they fall inside the dipole. This, in turn, increases the collision rate and keeps the atomic energy higher than

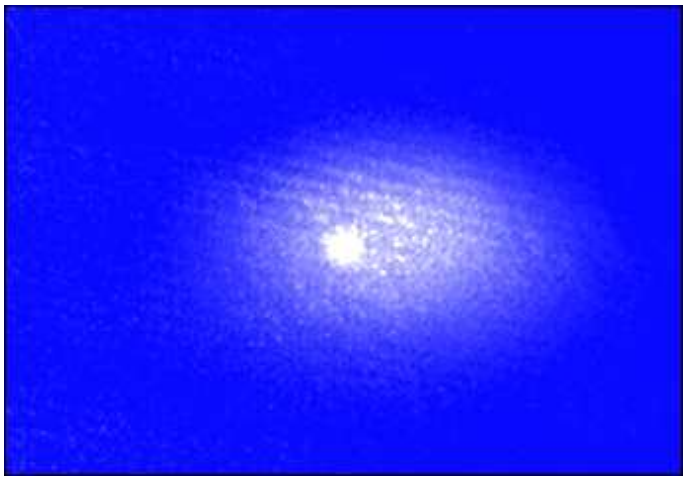

Figure 6.8: Absorption image of the cloud in presence of both magnetic and optical trapping. The absorption signal increases at the position of the dipole trap due to atomic accumulation into it. The imaging is performed on the plane orthogonal to the dipole trap beam.

the Ramsauer-Tawnsend minimum. We ramp up the dipole trap lasers to full power in 1 s and we wait in the combined magnetic and dipole trap for additional 2 s, to give the time to the cloud to thermalize and accumulate in the deep dipole trap. We then switch off the quadrupole trap abruptly and collect the remaining atoms in the dipole trap. We do not perform neither RF evaporative cooling in the quadrupole nor adiabatic decompression of the trap, since the collision rate is too low in the magnetic trap to determine an efficient evaporation. We estimate a collision rate at the center of about 38 Hz but, due to the Ramsauer-Townsend minimum, the rate is energy-dependent and reaches almost to zero in the tails of the thermal distribution. Evaporative cooling requires redistribution of atoms at different energies in order to be efficient and is, therefore, affected by the lack of collisions at higher energies. The cloud parameters, just after switching off the magnetic field, are: N=1.4×10^7, T=220 μK, n=5.1×10^{13} atoms/cm^3 and ρ=1.4×10^{-4}. We ascribe the increase in phase space density to the dimple effect and to plain evaporation of the hot part of

the cloud at the release of the magnetic trap.

6.4.1 Light induced losses

when we use high intensity in the trapping beams, we experience severe loss rates for atoms in the dipole trap. Due to the main dipole trap laser's large spectrum, these losses are likely to come from photo-association processes involving two atoms and two photons. The two free atoms are associated into a molecular state via a Raman transition. In this process, the binding energy of the molecule gets converted into kinetic energy and the molecule itself is lost from the trap. In Fig.6.9 I report the measured lifetime of the atomic sample in the dipole trap, as a function of the trapping beam power.

The photo-association process involves 2 photons and two atoms. The time constant τ is therefore proportional to $(nP^2)^{-1}$. Since the trapping frequencies are proportional to $\sqrt{P}$ and $n_0 \propto \frac{1}{\bar{\omega}^3}$, the dependence of τ on P is expected to be $\tau \propto P^{-3.5}$, in agreement with the results of the fit. As we see from the data, the lifetime increases very rapidly by decreasing the power. Therefore this kind of losses will be negligible after the first part of the evaporative cooling. These losses are important, however, during the loading of the dipole trap from the magnetic trap. At this stage, the incoming rate of atoms into the dipole trap (see Fig.6.8 for an image of the density distribution) is small due to the low collision rate in the magnetic trap. Once the atoms are in the dipole, they are rapidly lost due to the short lifetime. This is the main limitation to the number of atoms captured in the dipole trap. To overcome this limitation a single mode high power laser beam needs to be implemented.

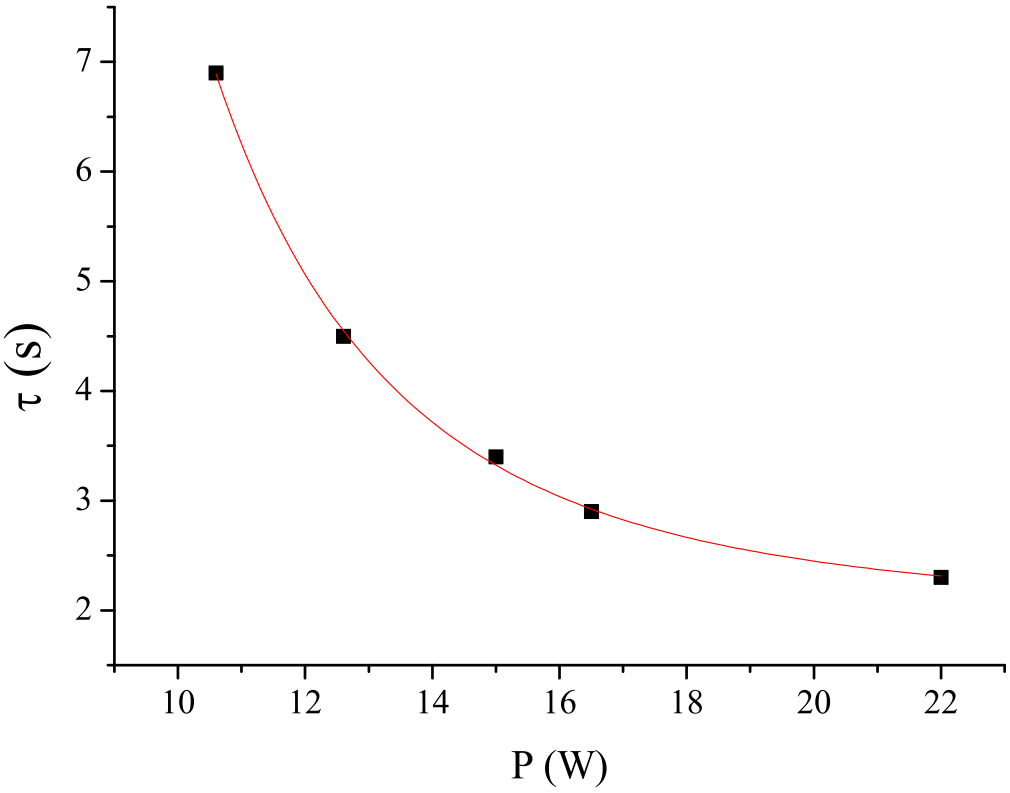

Figure 6.9: Measured value of the lifetime τ as a function of the laser power (black squares). The red line is a fit to the function τ=$a + bP^c$, the best fitting value of c is -3.7±0.2

6.4.2 Feshbach resonances and field calibration

An accurate knowledge of the magnetic field at the position of the atomic sample is required. This is necessary to know the exact positions of the Feshbach resonances and therefore to have a good estimation of the scattering length. The absolute value of the resonances and their characteristics are taken from[57] (see Fig.6.10). We calibrated the magnetic field by inducing RF transitions between the F=1, m_F=-1 and the F=1, m_F=0 hyperfine states and comparing the resonance frequencies to the Breit-Rabi formula. The measurements were done at magnetic fields for which the BEC in the m_F=0 state is unstable, so that the signal was actually atom losses

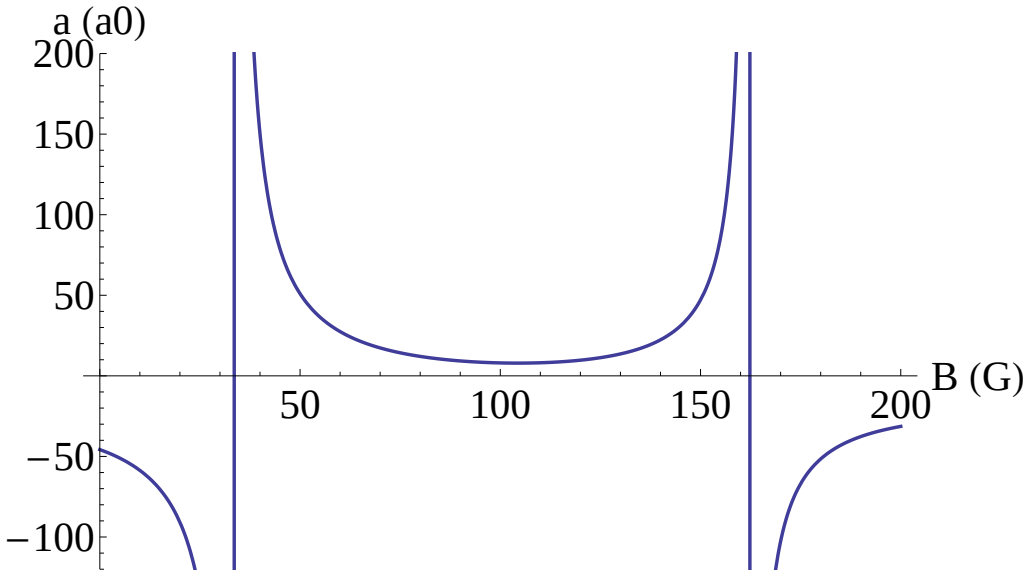

Figure 6.10: Value of the scattering length versus magnetic field for collisions between two atoms in the F=1, m_F=-1 state. Two Feshbach resonances are visible. Evaporative cooling in the dipole trap is performed close to the low field one around 45 G.

from the initial cloud. The objective of the calibration was to obtain the conversion factor to go from the applied current to the magnetic coils, to the generated magnetic field at the position of the atoms. This factor is found to be (12.62±0.03) G/A. The calibration is consistent with zero field at zero current within 100 mG.

6.5 All-optical evaporation of the atomic sample

Once the atoms are trapped in a purely optical potential, the scattering length is suddenly changed to 75 a_0 and the power in the main dipole trap beam is slowly reduced in order to perform evaporative cooling. The optimization of the evaporation ramp is performed by splitting the ramp in linear pieces. Each piece reduces the power by a factor 2 and the duration of each of them is optimized in order to

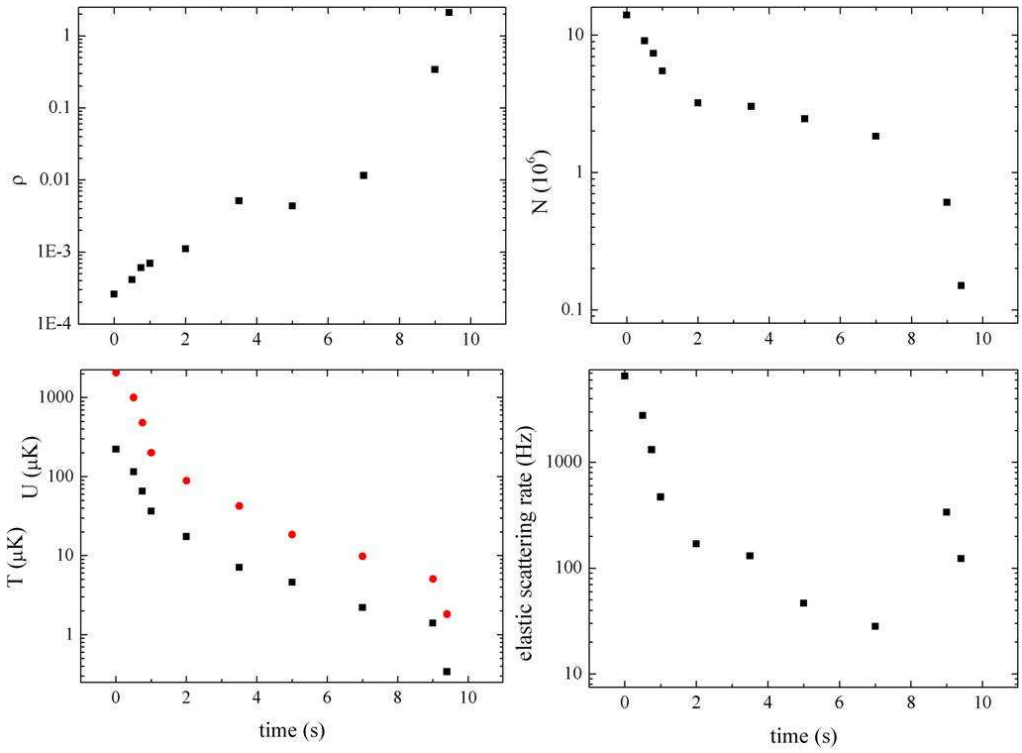

Figure 6.11: Sample parameters versus time during the evaporation ramp.

maximize the evaporation efficiency at each step. The resulting ramp, as well as the behavior of the main experimental parameters, is presented in Fig.6.11. The evaporation rate at the beginning is faster in order to avoid the photo-association losses, It slows down at intermediate times, and it speeds up again at the end thanks to the trapping frequency increase caused by the dimple. The effect of the dimple is apparent in the sudden increase of the density in the last two stages of the ramp. In the initial and final stages, the efficiency is reduced due to losses caused by photo-association processes and by three-body processes, respectively.

Finally, Fig.6.12 gives the achieved phase space density versus the number of atoms. The evaporative cooling efficiency is directly related to the slope of the graph. We clearly see the effect of the initial and final losses on the initial and final efficiency. The efficiency of the evaporation as a whole is 2. In the intermediate section, the

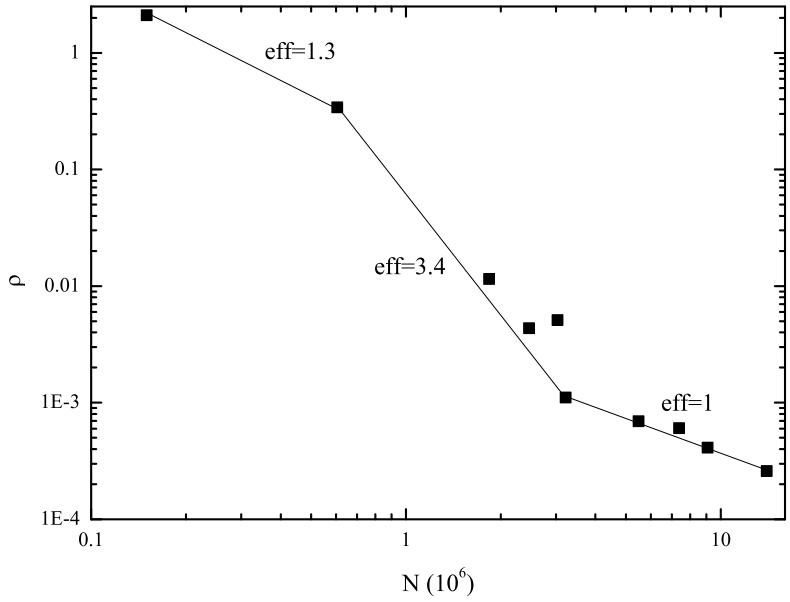

Figure 6.12: Phase space density versus number of atoms during the evaporation.

maximum achieved efficiency is around 3.4. At the end of the evaporative cooling we get a pure BEC of 1.5×10^5 atoms. This atom number is of the same order as what is realized by sympathetic cooling methods for ^{39}K. The whole sequence requires 20 s however, in comparison to the 60 s required in the other case.

6.6 A tunable Bose-Einstein condensate

We measured the condensate parameters by fitting absorption images like the ones in Fig.6.13. In case of images like the one on the lower left, we employed a bimodal fit by the sum of a Bose-enhanced thermal distribution plus a Thomas-Fermi distribution.

$$n(x,y) = \frac{N_{th}}{2\pi\zeta(3)\sigma_x\sigma_y} g_2 \left(e^{-\frac{(x-x_0)^2}{2\sigma_x^2} - \frac{(y-y_0)^2}{2\sigma_y^2}} \right) + \\ + \frac{5N_0}{2\pi R_x R_y} \left(1 - \left(\frac{x}{R_x}\right)^2 - \left(\frac{y}{R_y}\right)^2 \right)^{3/2} \theta \left(1 - \left(\frac{x}{R_x}\right)^2 - \left(\frac{y}{R_y}\right)^2 \right) \quad (6.11)$$

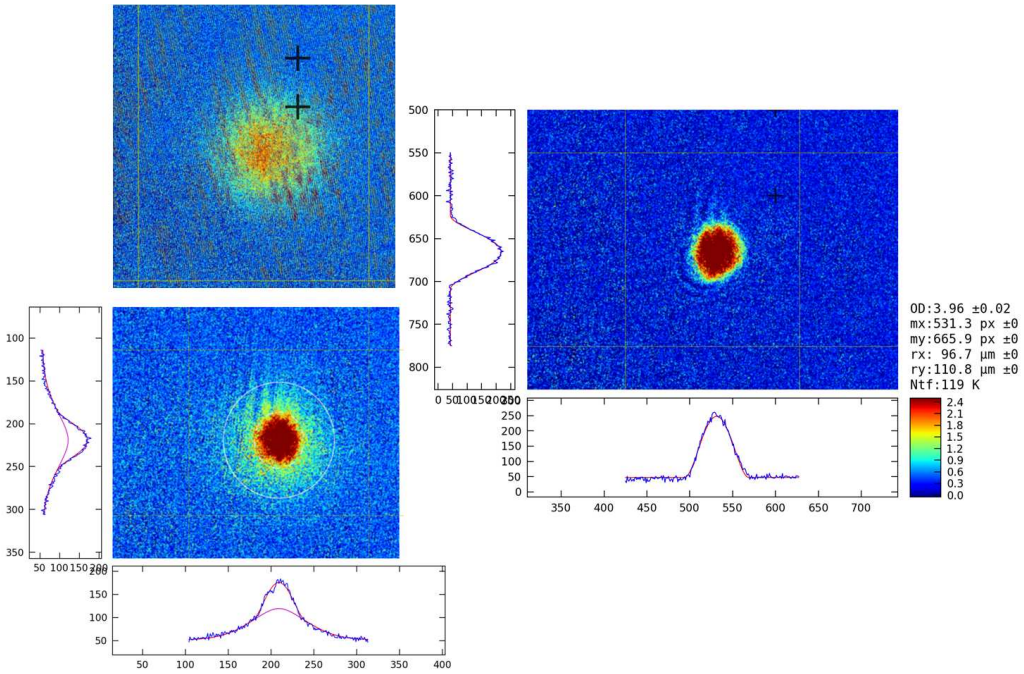

Figure 6.13: Absorption images and the corresponding atomic density profiles of the thermal cloud (upper left), the bimodal cloud (lower left) and of the pure BEC (right).

in which ζ is the Riemann zeta function, $g_2(x) = \sum_1^\infty \frac{x^i}{i^2}$, and θ is the Heaviside theta function. In cases like the one on the top left (purely thermal), or the one on the right (purely condense), the fit was was done by comparing the data with only one of the two functions. From the fit we infer the values of the atomic parameters: N_{th} (N_0) is the number of thermal (condensed) atoms, $\sigma_{x,y}$ are the $e^{-1/2}$ sizes of the thermal cloud, and $R_{x,y}$ are the Thomas-Fermi radii of the condensate. If the image is taken after a long time-of-flight t, such that the thermal size is much larger than the in-trap size, the measurement of the σs provides access to the system temperature by $\sigma^2/t^2 = k_B T/m$. In Fig.6.14 is reported a measurement of the condensed fraction (N_0/N_{th}) of the sample versus temperature. Absorption images are acquired at various evaporation stages. From a single picture we get the condensed fraction as

well as the temperature.

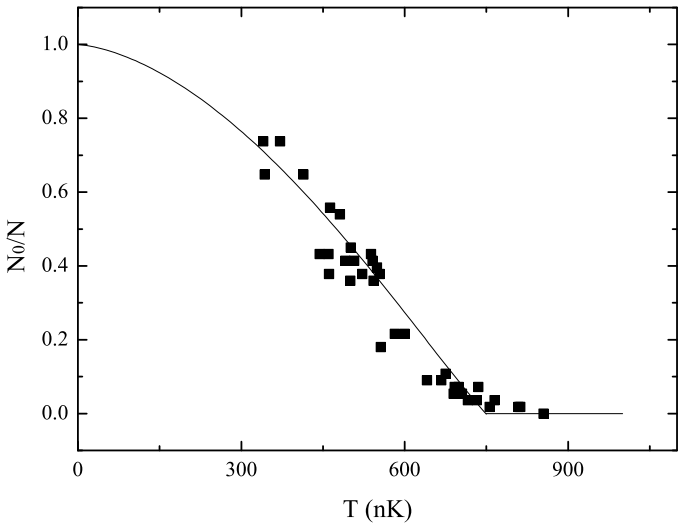

Figure 6.14: Condensed fraction as a function of temperature. The temperature is measured by the fit of the thermal part after time-of-flight. The solid line is the theoretical curve for a critical temperature of 750 nK. For this measurement the number of atoms in the pure condensate was 5×10^4. The lowest measured temperature was around 300 nK, further evaporation resulted in too low signal on the thermal fraction to get a reliable temperature measuremet.

The critical temperature is extracted from the temperature at which $N_0 > 0$. A fitting function of the form $(1-(T/T_c)^3)$ is also reported on the graph for comparison. The fitting function dependence on T is actually $(1-\alpha T^2)$, since the data are taken in different evaporation stages. Because of this, the trapping frequencies are not constant. The evaporation is performed by reducing the power in only one of the trapping beams. This changes two of the three trapping frequencies, proportionally to $P^{1/2}$. The critical temperature $k_B T_c = 0.94\hbar\overline{\omega}N^{1/3}$ is linear in the average trapping frequency $\overline{\omega}$. Therefore the critical temperature is proportional to the trapping beam power to the power 1/3 ($T_c \propto P^{1/3}$). The trap depth U_0 is proportional to the power. Since the evaporation is performed with a fixed truncation parameter

η, this means that $P \propto T$. This, finally, implies that $T_c \propto T^{1/3}$ during the ramp. From this considerations follows the choice of the fitting function. The measured T_c is an indication of the critical temperature at the evaporation stage at which the transition takes place. Due to the progressive reduction of the trapping frequency, the critical temperature decreases, further evaporating the sample[1].

A first test of the interaction tuning on our system was the measurement of the K_3 coefficient for three-body losses (See Sec.2.2), across the two Feshbach resonances of Fig.6.10. The results are presented in Fig.6.15. To get the K_3 coefficient we measured the time evolution of the number of atoms in the trap for different magnetic fields. We compared the measurements with the law[58]:

$$N(t) = \frac{N_0}{(1 + AN_0^{4/5} K_3 t/a^{6/5})^{4/5}} \quad , \tag{6.12}$$

which is valid for an interacting condensate. A is given by $A = 7 \times 10^{-4} \left(\frac{\bar{\omega} m}{\hbar}\right)^{12/5}$. In absence of Efimov physics[59, 60] the K_3 coefficient scales, close to the Feshabch resonance, as a^4, while it reaches a background value far from resonance. I also report atom losses caused by a special Feshbach resonance of a mixed channel nature. These are the red data in Fig.6.15. Recently, experimental evidences for a universal behavior of Efimov-physics have been reported by many groups[60]. ^{39}K represents an exception in this respect. We are performing more refined measurements of K_3 to investigate the possible violation of universal behavior for the Efimov three-body physics in potassium.

[1] in principle, also the progressive loss of atoms from the trap can modify the critical temperature, the dependence is anyway much weaker and the losses are not substantial

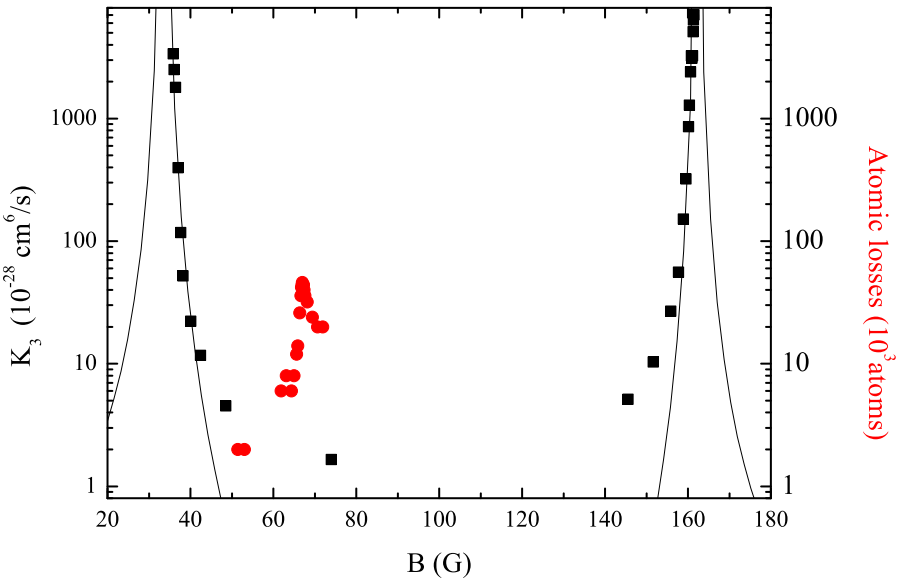

Figure 6.15: Measured K_3 coefficient for three-body losses across two Feshbach resonances in the F=1, m_F=-1 atomic state (black squares). Measured atomic losses in correspondence of a mixed resonance (red dots). The resonance is mixed in the sense that the entrance collisional channel is s-wave, while the output one is p-wave. The solid line is the expected behavior like $K_3 \propto a^4$ of the K_3 coefficient in absence of Efimov effects close to resonance. Far from resonance, K_3 reaches a background value of about 10^{-28} cm^6/s. is worth noticing that the scattering length does not go lower than 10 a_0 in between the resonances, therefore the true background value is probably not reached.

Chapter 7

Towards quantum interferometry

In this chapter I summarize the design of a few key components of the future interferometer based on entangled BECs. Beside the design of an ultra stable double-well interferometer based on optical potentials, I have also performed a numerical study of the coherence of a weakly interacting BEC in a double-well at finite temperature. Finite temperature effects can be exploited in order to perform thermometry in situations in which standard time-of-flight techniques are not reliable.

7.1 Thermal effects on the coherence of a BEC in a double well

In this section I calculate the effect of the finite temperature on the BEC in the double well. The coherence loss due to the finite temperature can give measurement of the temperature of the sample even at very low temperatures, for which standard time-of-flight is inefficient [61]. Moreover, in Ref.[18], the finite temperature was the main limit to the obtainable squeezing. Is therefore interesting to investigate its effect in details.

7.1.1 Theoretical modeling

In the two mode approximation, the double well Bose-Hubbard Hamiltonian (BH) is (see Sec.3.1):

$$H^{BH} = \frac{E_c}{2} J_z^2 - \frac{2E_j}{N} J_x \quad . \tag{7.1}$$

By using E_j as the energy scale and defining $\gamma = E_c/E_j$, the Hamiltonian becomes:

$$H^{BH} = \frac{\gamma}{2} J_z^2 - \frac{2}{N} J_x \quad . \tag{7.2}$$

we can write this on the base of the eigenstates of J_z, indicated as $|j, m\rangle$

$$\begin{aligned} H^{BH}_{m,m'} = \frac{\gamma}{2} m^2 \delta_{m,m'} - \frac{1}{N} \Big(& \sqrt{(j-m'+1)(j+m+1)}\,\delta_{m',m+1} + \\ & \sqrt{(j+m'+1)(j-m+1)}\,\delta_{m',m-1} \Big) \quad . \end{aligned} \tag{7.3}$$

Numerically diagonalizing this Hamiltonian we get its eigenvalues E_i and eigenstates $|i\rangle$. With them we can compute thermal averages of any observable A as:

$$\langle A \rangle = \frac{\sum_i \langle i|A|i\rangle e^{-\frac{E_i}{T}}}{\sum_i e^{-\frac{E_i}{T}}} \tag{7.4}$$

in which the parameter T is equal to $k_B T/E_j$. In the classical analogue of the above model we consider two separated BECs in the two wells with number of atoms n_l, n_r and phases ϕ_l, ϕ_r. The form of the classical Hamiltonian is:

$$H^{BH,class} = \frac{\gamma}{2} \frac{n^2}{4} - \sqrt{1 - \frac{n^2}{N^2}} \cos\phi \tag{7.5}$$

in which n is the difference in the number of atoms in the two wells $n = n_l - n_r$ and $\phi = \phi_l - \phi_r$ is the phase difference for the two BECs in the two wells. The classical form of the Hamiltoninan can be obtained from the quantum one, recalling the definition of the angular momentum operators (see Sec.3.1.1), and applying the substitution $a_j = \sqrt{n_j} e^{-i\phi_j}$ for $j = l, r$. The classical Hamiltonian can be used to compute classical thermal averages as

$$\langle A \rangle = \frac{\int_{-N}^{N} \int_{-\pi}^{\pi} A e^{\frac{-H^{BH,class}}{T}} dn d\phi}{\int_{-N}^{N} \int_{-\pi}^{\pi} e^{\frac{-H^{BH,class}}{T}} dn d\phi} \tag{7.6}$$

I will compare the results of the Bose-Hubbard Hamiltonian with the ones given by the quantum phase model (QP)[62, 63], whose Hamiltonian is:

$$H^{QP} = -\frac{\gamma}{2}\frac{d^2}{d\phi^2} - \cos\phi \quad . \tag{7.7}$$

This Hamiltonian can be obtained in many ways from the Bose-Hubbard one. We can start by linearizing the classical Hamiltonian $H^{BH,class}$ for $n/N, \phi/(2\pi) \ll 1$, obtaining the classical version of the quantum phase

$$H^{QP,class} = \frac{\gamma}{8}n^2 - \cos\phi \simeq \frac{\gamma}{8}n^2 + \frac{\phi^2}{2} - 1 \quad . \tag{7.8}$$

This can be used, like $H^{BH,class}$7.6, to get classical results. This Hamiltonian can be approximated by the one of an harmonic oscillator in the variables n and ϕ. Quantizing such an Hamiltonian one gets to H^{QP}. The exact quantization rule can be found by calculating the following commutator

$$[J_z, J_y] = -iJ_x \tag{7.9}$$

$$\left[\frac{n}{2}, \frac{N}{2}\sin\phi\right] = -i\frac{N}{2}\cos\phi \quad , \tag{7.10}$$

where, in the second line, I made use of $n/N \ll 1$. Taking the first order in ϕ of the above expression, one gets to the conclusion that, under these approximations, $n/2$ and ϕ can be regarded as conjugated quantities ($[\mathrm{n}/2, \phi] = -i$). The proper quantization of the classical Hamiltonian in the phase space consists, therefore, in $n/2 \to -i\frac{d}{d\phi}$. The quantum phase Hamiltonian H^{QP} can be discretized on the phase space and diagonalized to provide thermal averages of the form 7.4.

The observable I want to compute is the coherence factor α . This represents the averaged contrast of the interference fringes obtained by releasing the BEC from the trap and letting it interfere after time-of-flight (the average is intended over many experimental realizations)[64]. The many-body wavefunction of the system, in the coordinate basis, is (see Sec. 3.1)

$$\widehat{\Psi}(x) = \psi_l(x)a_l + \psi_r(x)a_r = \psi\left(x - \frac{d}{2}\right)a_l + \psi\left(x + \frac{d}{2}\right)a_r \quad , \tag{7.11}$$

where d is the distance between the wells. The last equality follows from the fact that the two wells are perfectly symmetric. In momentum space the above expression looks like

$$\widehat{\Psi}(p) = \psi(p) a_l e^{-i\frac{pd}{2}} + \psi(p) a_r e^{i\frac{pd}{2}} \quad . \tag{7.12}$$

From this expression we can compute the density in momentum space $n(p)$. This quantity is experimentally accessible by a measurement of the spatial distribution of the atomic cloud after time-of-flight

$$n(p) = \left\langle \widehat{\Psi}^{+}(p)\widehat{\Psi}(p) \right\rangle = |\psi(p)|^2 \left\langle N + 2\cos(pd) J_x - 2\sin(pd) J_y \right\rangle \quad . \tag{7.13}$$

We can always work with $\langle J_y \rangle$=0, by redefinition of the condensate phase origin. The above expression describes an interference pattern given by $2\cos(pd)\langle J_x \rangle$. The contrast of such pattern is $\alpha = \left\langle \frac{2J_x}{N} \right\rangle$. By employing the same conversion rules used to find the Hamiltonians of the different models and their classical analogues, the following expressions for α are found:

$$\alpha^{BH} = \left\langle \frac{2J_x}{N} \right\rangle \tag{7.14}$$

$$\alpha^{BH,class} = \left\langle \sqrt{1 - \frac{n^2}{N^2}} \cos\phi \right\rangle \tag{7.15}$$

$$\alpha^{QP} = \alpha^{QP,class} = \langle \cos\phi \rangle \tag{7.16}$$

7.1.2 Parameter regions

Three parameters regions are distinguished. The first one is the Rabi regime, or non-interacting regime, obtained when $E_c \ll E_j/N^2$ or equivalently $\gamma \ll \frac{1}{N^2}$. In the second regime, called Josephson regime $1 \gg \gamma \gg \frac{1}{N^2}$. Finally, in the Fock, or highly interacting regime $\gamma \gg 1$. The QP model is supposed to be in agreement with the BH model in the Josephson and Fock regimes. Deviations are expected, instead, in the Rabi regime. The Rabi regime can be reached experimentally by employing

Feshbach resonances to suppress interactions. It is therefore very interesting for our purposes of realizing an interferometer with non-interacting atoms.

7.1.3 Classical results

One can easily compute the classical formulas for the thermal average of the coherence parameter α. Explicitly, for the QP model

$$\alpha^{QP,class} = \frac{\int e^{\frac{\cos\phi}{T}} \cos\phi d\phi}{\int e^{\frac{\cos\phi}{T}} d\phi} \quad , \tag{7.17}$$

while, for the BH model,

$$\alpha^{BH,class} = \frac{\int \sqrt{1-\frac{n^2}{N^2}} e^{-\frac{\gamma n^2}{8T}} \int \cos\phi e^{\frac{\sqrt{1-\frac{n^2}{N^2}}\cos\phi}{T}} dnd\phi}{\int e^{-\frac{\gamma n^2}{8T}} \int e^{\frac{\sqrt{1-\frac{n^2}{N^2}}\cos\phi}{T}} dnd\phi} \quad . \tag{7.18}$$

It is easy to see that, in the limit $\gamma \gg 8T/N^2$, equation 7.18 reduces to 7.17, since the term $e^{-\frac{\gamma n^2}{8T}}$ becomes proportional to the Dirac delta $\delta(n)$. Interestingly, the limit of validity of the QP model depends on T. For certain parameters, the system can obey the QP model for low T, but can show deviations for higher T[1]. The numerical calculation of the two equations gives the result of picture 7.1. We can see that the QP result represents an upper bound to the coherence of the system as calculated from the BH model. We can have some insight by considering small fluctuations of the parameters n and ϕ around zero

$$\alpha = \left\langle \sqrt{1-\frac{n^2}{N^2}} \cos\phi \right\rangle \approx 1 - \frac{\delta n^2}{2N^2} - \frac{\delta\phi^2}{2} \quad . \tag{7.19}$$

The QP model neglects the thermal fluctuations on the atom number, but account properly for the ones in the phase. We can conclude that, in the regime in which quantum fluctuations are not dominant (low interactions), the increase of the interaction strength can counterbalance thermal fluctuations and increase coherence.

[1] strictly speaking, in any situation the system will show deviations from 7.17 for large enough T. Anyway, in practical experimental conditions, the two-mode approximation will be inappropriate to describe the system when T becomes too large

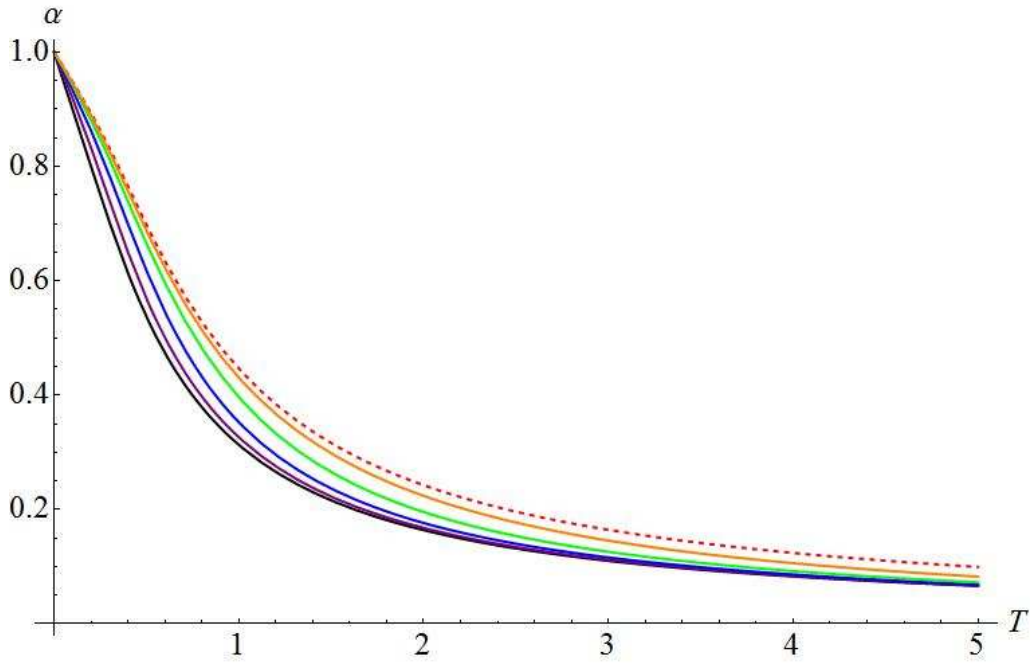

Figure 7.1: Numerical calculation of the classical coherence factor. The black line is the non interacting result. Red dashed curve is the classical QP model result. The rest of the curves are classical BH results for various γs: purple curve is $\gamma = 3/N^2$, blue is $\gamma = 10/N^2$, green is $\gamma = 30/N^2$ and orange $\gamma = 100/N^2$. Even though this values of γ are in the Josephsson regime at T=0, the QP shows deviations from the BH result at non zero temperature.

7.1.4 Quantum results

I numerically diagonalized the BH Hamiltonian for N=100 and compute the coherence factor α by the formula 7.4. I did the same for the QP model, by discretizing the phase space on a 1000 points grid. The time consumption was similar for the two models and of the order of a minute on a standard laptop. The results showed agreement with the correspondent classical results for small interactions. For high interactions, the coherence is lost due to the suppression of number fluctuations (Fig. 7.2). In the high interactions regime, the QP model shows nice agreement with the BH model. We see from Fig.7.2 that, for high interactions, the effect of

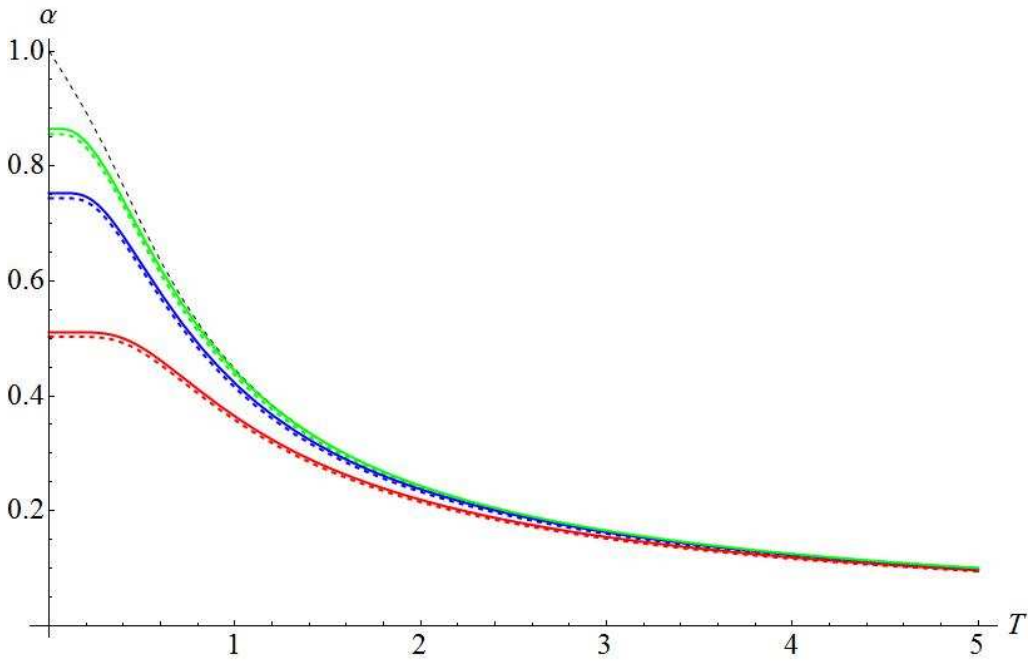

Figure 7.2: Numerical calculation of the quantum coherence factor. The black dashed line is the classical result (in the regime of γs considered here QP and BH classical results agrees). Solid curves refers to the quantum BH result, while dashed ones to the quantum QP. The green curves are calculated for $\gamma = 1/3$, the blue curves for $\gamma = 1$ and the red ones for $\gamma = 3$.

quantum fluctuations reduces the coherence of the system. By combining the classical result of the previous section (which turn out to be valid for low interactions) to the quantum results, we see that, at non zero T, the effect of interactions initially increases the coherence factor, for low values of γ, while it decreases it for higher values. This leads to the appearance of a "coherence maximum", that is shown in Fig. 7.3.

The reported calculations reveals the interplay of thermal and quantum fluctuations in determining the coherence of a BEC in a double well. In [61] the authors uses the QP model to determine the temperature of the system by measuring the phase fluctuations in the Josephson regime. Corrections to the QP model might be

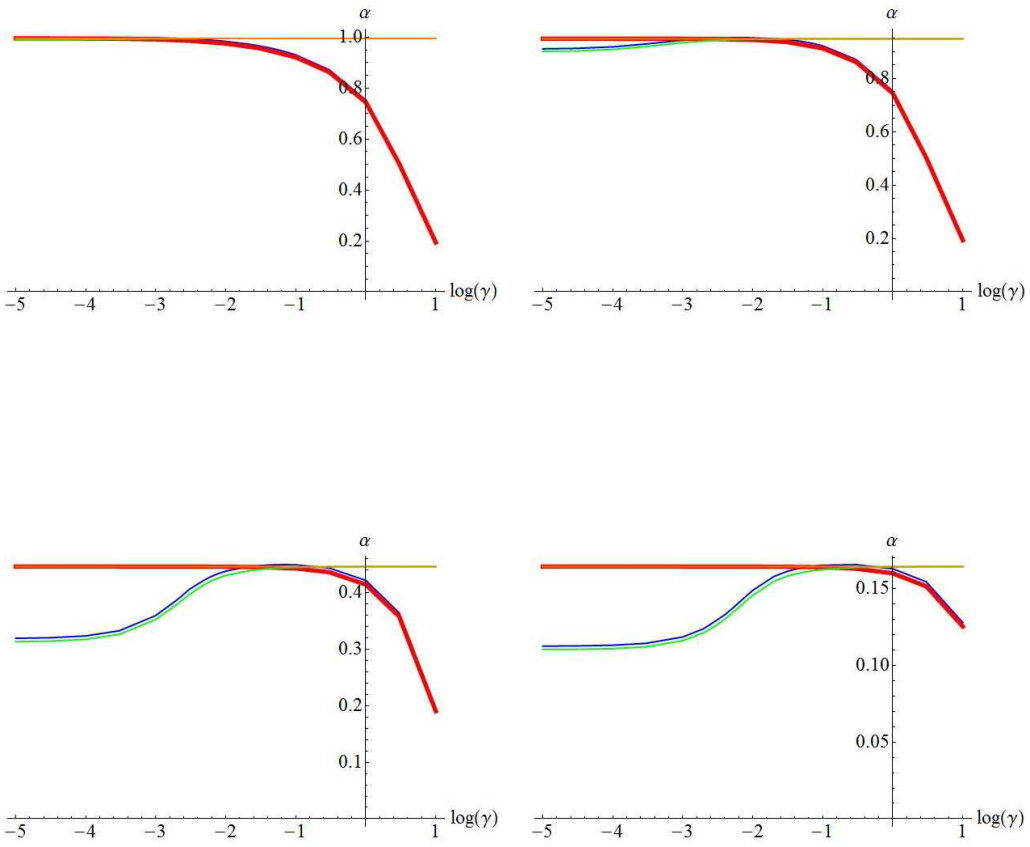

Figure 7.3: Coherence factor as a function of γ, in log scale, calculated using the four models described in the text for T=0.01 (up left) T=0.1 (up right) T=1 (low left) and T=3 (low right). Classical QP result (orange), QP numerical result (red), classical BH (green) and BH numerical result (blue). We see that, for low temperatures the two quantum models agrees with each other as do the two classical models. Quantum fluctuations reduces the quantum coherence with respect to the classical result when approaching the Fock regime. Already for T=0.1, corrections to the QP model are significant in the Rabi regime. For higher temperatures a coherence maximum developes.

important to determine the exact temperature. As it is shown in Fig. 7.3, those corrections are, in fact, important in the low interaction part of the Josephson regime and for $k_BT \approx E_j$. This is exactly the temperature regime in which thermometry can be performed. The appearance of the coherence maximum has an analogy to the phase diagram of bosons on a lattice in the presence of disorder and interactions. In that case the presence of disorder can easily destroy the coherence of the non-interacting BEC by causing Anderson localization. Adding moderate interaction the system is brought back into the BEC phase, gaining coherence. Increasing further the interaction strength, the system ends up in the Mott insulator incoherent regime. Temperature in the double well can play the role of disorder in the lattice.

7.2 Optical double well design

The design and feasibility check of the double-well trap was carried out during the first year of my PhD. The main requirements, to be able to perform high precision, entanglement-assisted, measurements, concerns the stability of the trap. The use of an optical lattice was already successful in the demonstration of entanglement in a double well in[18]. An optical lattice scheme is very robust against intensity fluctuations of the lattice beams, since this kind of fluctuations are common-mode for the double well. The use of an extra laser, as in [18], for the selection of two sites among the others, introduces an extra instability due to pointing instability and can determine noise on the double well potential.

Our idea is to improve on such scheme by the use of a superlattice configuration. Two lasers, one with a wavelength twice the other, will create such superlattice, which can be visualized as a lattice of equally spaced double wells (see Fig.7.4). The parameters of the wells can be tuned acting on the individual lasers power and on their frequency difference. By crossing the bichromatic beams at a small angle,

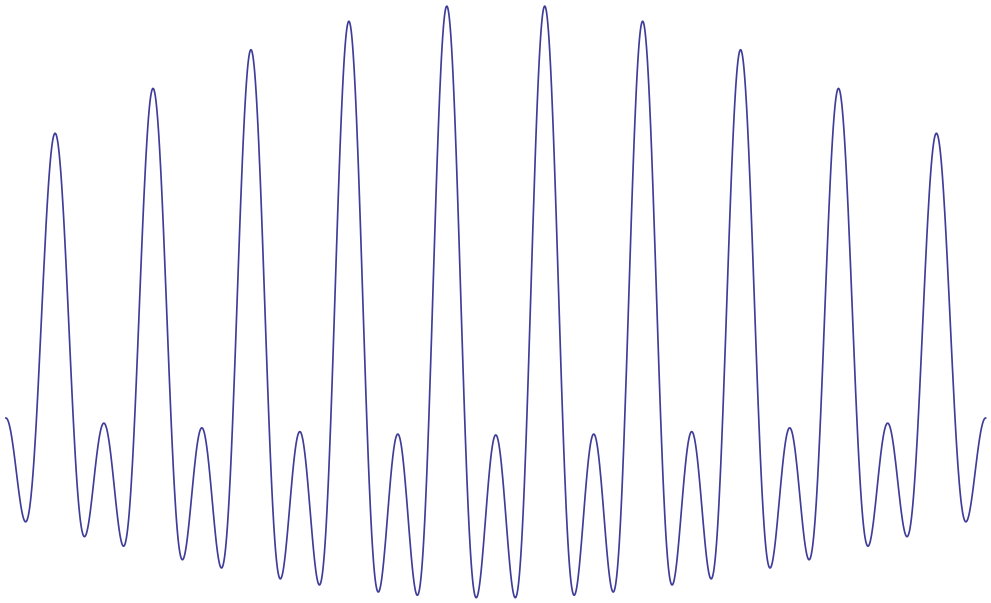

Figure 7.4: Optical potential originating from the superlattice configuration described in the text. In each primary site a double well interferometer can be realized. The spacing between the wells depends on the angle under which the lattice lasers are crossing.

the distance between the wells can be magnified, allowing for single-site resolved imaging. Such a simple idea presents many technical difficulties. My analysis was a first step towards their identification.

The first parameter to choose is the laser wavelength to use. Differently from the recent realizations of superlattices[65, 66], one of the main concern is about the lifetime of the sample to be large. For this reason, the two employed wavelength have both to be far off-resonance from the atomic transition. An option is to use a Yb laser at 1064 nm and double it to 532 nm: the first laser is red-detuned and the second one blue-detuned with respect to the D2 line of potassium. The atomic polarizability and the scattering rate are similar for the two wavelengths. An even better option would be a CO_2 laser around 10μm and its frequency doubled at 5μm

region. The need for special optics for the vacuum windows and the easier operation and reliability of the Yb lasers, brought the choice on the first option. A Coherent Mephisto laser with a custom doubling stage is being prepared in the laboratory at this moment.

The second choice was on the angle between the beams, for this influences the tunneling rate and the trapping frequencies, effectively acting on the time scale of the experiment. If the beams cross with an angle θ, the spacing between the wells is magnified by a factor $a = 1/\sin(\theta/2)$. The trapping frequency on the shallower direction is reduced by a factor a^{-2}. This implies that, if we want to significantly magnify the separation, we will have to work with a very low trapping frequency. Such low trapping frequency will set a limit on the time variation of the trap parameters, in order not to excite radial modes. For this reason we decided to use an extra trapping beam, aligned along the lattice direction, in order to increase the radial trapping frequencies. The extra trapping beam contributes to the energy along the lattice only via a constant term plus its longitudinal trapping. This is anyway small compared to the radial trapping of the lattice beams. Given this, its intensity noise will be reasonably common mode.

An angle of around 0.1 rad (5°) will result in double wells with a separation of 5 μm, spaced by 10 μm. Such large spacing also brings down the power requirement for the realization of negligible tunneling rates. The extra trapping laser for the radial trapping can be, in principle, of a different wavelength with respect to the lattice lasers. If for such a laser a wavelength of 1064 nm is used, and we want to achieve reasonable trapping frequencies (50-100 Hz), the scattering rate of such a beam will be around 10 mHz. This will constitute the main decoherence source induced by the trapping beams.

We require that, during the time of the interferometric sequence τ, not even one atom undergoes an out of resonance transition. This will, in fact, spoil the phase co-

herence of an entangled sample. We can rephrase the condition in $N\tau \ll 1/(10\text{ mHz})$ [2]. For a 1 s interferometer, this condition sets the maximum atom number in each interferometer to around 100. If we have a BEC with 10^5 atoms, the best strategy consists of splitting it into 10^3 double wells, each containing 100 atoms. This way, the entanglement will be preserved in most of the double wells in each experimental realization. Algorithms to reject the eventual incoherent outcomes of the interferometer will be useful to sort them out. Otherwise, the optimal squeezing level can be chosen for which, given the experimentally determined level of decoherence, the final sensitivity is maximized. I did not consider these possibilities since they are very sensitive to the final experimental situation. The number of realizable double wells is anyway limited by the trapping beams power. The operation of such a high number of interferometers in parallel would also allow for noise cancellation and for large statistics with a single experimental realization. The main problem will be the dishomogeneity of the double well parameters along the lattice due to the beam profile.

In order to increase the sustainable atom number in each interferometer, a CO_2 laser for the radial trapping beam can be implemented, substantially reducing its decoherence contribution to around 1 mHz. This would allow for 1000 atoms given the same time τ=1 s . Such an upgrade would anyway require an analogue one, for the vacuum lifetime to reach 10^3 s. Background collisional losses, as one-body processes, are, in fact, no different from out of resonance scattering, for what concerns the coherence of the sample.

The beam waist for the lattice lasers has to be as large as possible, given the available power, in order to increase homogeneity of the lattice itself. A waist of

[2]This condition is the one that we need to fulfill to preserve the coherence of a maximally entangled state, that would give a phase resolution at the Heisemberg limit. The use of different squeezed states relaxes such a request allowing for more atoms in each interferometer or longer phase accumulation times.

around 0.5 mm is feasible given the actual setup, which provides 3 W at 532 nm and 10 W at 1064 nm. The limit being the green laser power. Such a waist sets to around 50 the number of interferometers that can be operated in parallel with similar double well parameters.

Another important source of decoherence comes from three-body losses. The rate of such losses depends on the density. The same requirement of not even one event during the experiment translates into $N\tau \ll 1/(N^2 A)$. A is a parameter containing information about the K_3 coefficient for the losses and the trapping frequencies. Its value is given by

$$A = \frac{8K_3 m^3 \overline{\nu}^3}{\sqrt{27}\hbar^3} \quad , \tag{7.20}$$

in which $\overline{\nu} = \overline{\omega}/(2\pi)$ is the average trapping frequency. Substituting the minimum K_3=1.3×10^{-41} m^6/s, realized on the zero crossing of the Feshbach resonance, the coherence requirement reads $\overline{\nu}$ ≪6.2×10^4/(N$\tau^{1/3}$) Hz. Which limits the average trapping frequency to 600(60) Hz for N=100(1000) and τ=1s.

It seems feasible, therefore, to implement, in the existing setup, an interferometer that operates at the Heisemberg limit for 100 atoms in each of the double wells. Higher atom numbers can be used depending on the achieved squeezing level. Environmental noise, coming from spurious magnetic fields or beams vibrations, will be seen as phase noise and, therefore, have to be minimized. The possibility to perform differential measurements, however, can allow us to reduce those effects and recognize the common mode noise from the fundamental one.

7.3 Detection issues and possible strategies

Efficient detection of the atoms remains the most complicated point to address. I will only briefly discuss the main problems and I will give some simple ideas on how we are counting to solve them. Anyway this is still work in progress. The fundamental

problem originates from the fact that photon counting is exploited to count the atoms themselves. The shot noise in the photon's detection can dominate over the atomic noise if squeezing is employed[67]. The photon's noise is shot noise limited and thus can be reduced if every atom scatters many photons. Let us consider a certain number of atoms N, that we want to detect with an error of ± 1 atom (Heisemberg limit). If each atom scatters a certain number of photons N_p, which are detected with an efficiency β, the total signal from the cloud on the camera will be proportional to $\beta N N_p$, with shot noise fluctuations given by: $\sqrt{\beta N N_p}$. If those fluctuations are lower than the signal of a single atom, βN_p, the requirement is fulfilled. This implies $\beta N_p > N$. The number of detected photons, therefore, has to be higher than the number of atoms. A reasonable collection efficiency for fluorescence imaging can range around 10 %, by considering the collection angle, the ccd camera quantum efficiency, and reflections on the optical elements. the efficiency can be as high as 80 % in absorption. This means that, if we want to be Heisemberg limited for a cloud of 1000 atoms, each of them has to scatter at least 10000 photons in fluorescence or 1250 in absorption. In standard flourescence or absorption imaging such a high number of scattered photons is not sustainable, due to recoil heating of the cloud.

Recently developed fluorescence techniques for the detection of single atoms in optical lattices[7] can provide such high number of scattered photons. The technique employed are based on the fact that atoms are stored in an extremely confining optical lattice (trap depth of thousands of recoil energies) and continuously cooled by laser cooling during the signal acquisition. The acquired signal is nothing but the scattered cooling light. In such techniques usually single site resolution is also achieved, which is however not necessary in our case. The main problem this approach presents is the occurrence of atomic recombinations whenever two atoms are found to occupy the same lattice site. In order to avoid such occurrence our idea

is to load a very diluted atomic sample, into the imaging lattice, once the interferometric sequence is performed. Dilution can be realized by increasing interaction energy and decreasing or even releasing radial trapping before loading. A dipole trap with wavelength around 750 nm can be used to create the imaging lattice[3]. If a cloud, containing 1000 atoms, is made into an average size of 10 μm, the average number of atoms per site would be 5×10^{-2}. Such a scheme was never attempted for potassium and requires a substantial complication of the experimental apparatus. Anyway it seems, in principle, feasible. In the case in which also single site resolution for the imaging lattice is available, the estimation for the number of scattered photons required relaxes. The only requirement is that the signal from each atom has to be substantially larger than the background noise on the ccd camera. The probability of atom losses has be lower than $1/N$ in both cases. This is probably the main limiting factor. For example, if the imaging time is 1 s, as in[7], the lifetime of the sample needs to be N times larger than the imaging time, for not even 1 atom to be lost during detection. The detection time will be determined by the achievable scattering rate of the imaging photons and by the background noise level. Due to the peculiarity of laser cooling in potassium, the performances of laser cooling in a sample of atoms trapped in an optical lattice are hardly predictable and experimental tests needs to be carried out in this direction.

[3]This is just one possible choice. Its advantages are the small lattice spacing and the large polarizability, which reduces the required power to realize large trap depths. The problem is, anyway, the large heating determined by out-of-resonance scattering. This can increase the atomic temperature if the heating rate becomes comparable to the one given by the cooling beams. The cooling parameters are hard to predict at the moment given the peculiarity of laser cooling for potassium.

Chapter 8

Conclusions

In conclusion, in this thesis I described the first steps towards quantum interferometry with tunable BECs. They consisted in the realization of an apparatus for the production of tunable BECs of ^{39}K in single species operation, with all the related development of the laser and evaporative cooling processes that this requires, and in the first numerical simulations and design of a few key ingredients of the future device. In particular, during the realization of the experiment, we demonstrated for the first time sub-Doppler laser cooling in this system which is one of the key ingredients for the production of the BEC and opens the way for many interesting applications with tunable ^{39}K. For example, interferometry with thermal samples, as well as the imaging technique described in the last section, both requires efficient sub-Doppler cooling to be operated. The obtainment of condensation of ^{39}K in single species operation reduces the experimental effort necessary to operate with tunable BECs and allows for more stable and reliable systems to be realized. Note that, the new apparatus will allow for many different applications besides interferometry, ranging from Efimov physics to Anderson localization. The various simulations reported in the last part of this thesis, regarding finite temperature effects and the design of an ultra stable experimental setup can now be exploited for the experimental real-

ization of an atom interferometer based on tunable BECs in double well potentials that will be able to operate below the shot-noise limit, possibly approaching the Heisemberg limit.

Special thanks

I would like to thank Giovanni Modugno and Marco Fattori ("l'infallibile") for having involved me in the project and given me the opportunity to realize all the things described in this thesis. I also thank Augusto Smerzi to have tried hard and eventually succeeded in teaching me some theory.

I would also like to give credit and to thank all the friends who worked in the lab during these years: l'infallibile Marco Fattori for sharing his ideas with me, for taking care of most of the electronic systems in the lab and for his major contribution to the design of the vacuum system. Dimitris Trypogeorgos for organizing most of the lab and the computer system, for programming most of the software used in the experiment, for his help in building the laser system, for the coffee and the advices. Stefano Ferrari for his help in building part of the vacuum system and in the realization of the MOTs. Leonardo Carcagnì for his help in the measurements and the analysis related to sub-Doppler cooling and to the magnetic transport and for his efforts to realize the previous coil mount. Giacomo Roati for his advices on just about everything, for the seminal design of the laser system and his help during the baking of the science chamber. Sanjukta Roy-Chaudhuri for building part of the trapping laser system and for her help during the optimization of the evaporation procedures. Arturo Bambini, even if I never met him, for his foreseen about potassium and for writing the code used for the analysis of the sub-Doppler cooling process that Francesco Cataliotti kept in its laptop for about ten years until

he passed it over to us. It was a great adventure and it's not over yet. I'm just sorry that the nice results all came up in the last months so that some of you were not here to enjoy them.

I would also like to thank many other people for stimulating lunch discussions: Eleonora Lucioni, Luca Tanzi, Chiara D'Errico, Matteo Zaccanti, Benjamin Deissler, Saptarishi Chaudhuri, Francesco Piazza, Jan Chwedenczuk, Philipp Hyllus, Pietro Lombardi, Guido Pagano, Marco Schioppo, Marco Tarallo, Giacomo Lamporesi, Jacopo Catani, Devang Naik, Chiara Fort and Massimo Inguscio. A special thanks goes to Caterina for her help in correcting the thesis. Infine ringrazio la mia famiglia, e la famiglia di Caterina per avermi aiutato e sostenuto per questi tre anni.

Bibliography

[1] M. H. Anderson, J. R. Ensher, M. R. Matthews, C. E. Wieman and E. A. Cornell. "Observation of Bose-Einstein Condensation in a Dilute Atomic Vapor", Sciece, 269:198-201 (1995).

[2] M. Inguscio, S. Stringari and C. E. Wieman, "Bose-Einstein condensation in atomic gases", Proceedings of the International School of Physics "Enrico Fermi", course CXL, IOS Press, Amsterdam (1999).

[3] M. R. Matthews, B. P. Anderson, P. C. Haljan, D. S. Hall, C. E. Wieman and E. A. Cornell, "Vortices in a Bose-Einstein condensate", Phys. Rev. Lett. **83**, 2498 (1999).

[4] J. Billy et al., "Direct observation of Anderson localization of matter waves in a controlled disorder", Nature **453** (7197), 891-894 (2008).

[5] G. Roati et al., "Anderson localization of a non-interacting Bose-Einstein condensate", Nature **453** (7197), 895-898 (2008).

[6] M. Greiner, O. Mandel, T. Esslinger, T. W. Haensch and I. Bloch, "Quantum phase transition from a superfluid to a Mott insulator in a gas of ultracold atoms", Nature **415**, 39-44 (2002).

[7] J. F. Sherson, C. Wetenberg, M. Endres, M. Cheneau, I. Bloch and Stefan Kuhr, "Single-atom-resolved fluorescence imaging of an atomic Mott insulator", Nature **467**, 68-72 (2010).

[8] J. I. Cirac and P. Zoller, Phys. Today **57**, 38 (2004).

[9] U. Fano (1935) Nuovo Cimento **12** 156.

[10] U. Fano (1961) Phys. Rev. **124** 1866.

[11] H. Feshbach H. (1962) Ann. Phys. (N. Y.) **19** 287.

[12] M. R. Andrews et al., Science **275**, 637 (1997).

[13] B. P. Anderson and M. A. Kasevich, Science **282**, 1686 (1998).

[14] A Peters, K Y Chung and S Chu "High-precision gravity measurements using atom interferometry" Metrologia **38** 25 (2001).

[15] M. Fattori, C. D'Errico, G. Roati, M. Zaccanti, M. Jona-Lasinio, M. Modugno, M. Inguscio, and G. Modugno, "Atom Interferometry with a Weakly Interacting Bose-Einstein Condensate" Phys. Rev. Lett. 100, 080405 (2008).

[16] L. Pezzé, L. A. Collins, A. Smerzi, G. P. Berman and A. R. Bishop, "Sub-shot-noise phase sensitivity with a Bose-Einstein condensate Mach- Zehnder interferometer", Phys. Rev. A **72**, 043612 (2005).

[17] Y. Shin, M. Saba, T. A. Pasquini, W. Ketterle, D. E. Pritchard, and A. E. Leanhardt, "Atom Interferometry with Bose-Einstein Condensates in a Double-Well Potential", Phys. Rev. Lett. **92**, 050405 (2004).

[18] J. Esteve, C. Gross, A. Weller, S. Giovanazzi, and M. K. Oberthaler, Nature 4**55**, 1216-1219.

[19] L. De Sarlo, P. Maioli, G. Barontini, J. Catani, F. Minardi and M. Inguscio, Phys. Rev. A **75**, 022715 (2007).

[20] G. Modugno, G. Ferrari, G. Roati, R. J. Brecha, A. Simoni and M. Inguscio, Science **294**, 1320 (2001).

[21] Cohen-Tannoudji, C., Dupont-Roc, J. and Grynberg, G. (2008) Frontmatter, in Atom - Photon Interactions: Basic Process and Appilcations, Wiley-VCH Verlag GmbH, Weinheim, Germany.

[22] H. Perrin, "Les Houches lectures on laser cooling and trapping" 19-30 September 2011.

[23] H. J. Metcalf, P. Van der Straten, "Laser cooling and trapping" Springer (1999).

[24] T. W. Hänsch and A. L. Schawlow, Opt. Comm. **13**, 68 (1975).

[25] J. Dalibard, and C. Cohen-Tannoudji, J. Opt. Soc. Am B. **6**, 2023 (1989).

[26] Castin Y., Mølmer K., Phys. Rev. Lett. **74** 3772-3775 (1995), "Monte Carlo wave-function analysis of 3D optical molasses".

[27] J.T.M. Walraven, "Elements of Quantum Gases: Thermodynamic and Collisional Properties of Trapped Atomic Gases Les Houches lectures and more" (2008).

[28] A. Einstein, "Quantentheorie des einatomigen idealen gases", Sitzungsberichte der Preussischen Akademie der Wissenschaften **1**:3 (1925).

[29] S. N. Bose, "Plancks gesetz und lichtquantenhypothese", Zeitschrift fur Physik **26**:178 (1924).

[30] L. P. Pitaeskii and S. Stringari, "Bose-Einstein Condensation", Clarendon Press, Oxford, (2003).

[31] N. Bogoliubov, J. Phys. USSR, **11**, 23 (1947).

[32] F. Dalfovo, S. Giorgini, L. Pitaevskii, S. Stringari, Rev. Mod. Phys., **71**, 453 (1999).

[33] C. J. Joachain, "Quantum Collision Theory", North Holland, Amsterdam (1983).

[34] C. Cohen Tannoudji "Condensation de Bose-Einstein des gaz atomiques ultra froids : effets des interactions" Leçons du Collège de France, (13 10 1998).

[35] C. Ramsauer, Über den Wirkungsquerschnitt der Gasmoleküle gegenüber langsamen Elektronen, Annalen der Physik, **4**, 64 (1921), pp. 513-540.

[36] V. B. Braginsky, Y. I. Vorontsov, Sov. Phys. Usp. **17**, 644 (1975).

[37] P. Hyllus, O. Gühne, A. Smerzi, "Not all pure entangled states are useful for sub shot-noise interferometry", Phys. Rev. A, **82**, 012337 (2010).

[38] C. W. Helstrom, "Quantum Detection and Estimation Theory", Academic Press, New York, (1976).

[39] A. S. Holevo, "Probabilistic and Statistical Aspects of Quantum Theory" North-Holland, Amsterdam, (1982).

[40] F. Piazza, L. Pezzé, and A. Smerzi "Macroscopic superpositions of phase states with Bose-Einstein condensates" Phys. Rev. A **78**, 051601(R) (2008).

[41] E. Arimondo, M. Inguscio and P. Violino, Rev. Mod. Phys. **49**, 31 (1977).

[42] J. H. Shirley, "Modulation transfer processes in optical heterodyne saturation spectroscopy", Opt. Lett. **7**, 537 (1982).

[43] D.J. McCarron, S.A. King, and S.L. Cornish, "Modulation transfer spectroscopy in atomic rubidium", Meas. Sci. Technol. **19**, 105601 (2008).

[44] http://www.esrf.eu/Accelerators/Groups/InsertionDevices/Software/Radia

[45] K. Dieckmann, R.C. Spreeuw, M. Weidemüller, and J.T.M. Walraven, "Two-dimensional magneto-optical trap as a source of slow atoms", Phys. Rev. A **58** 3891 (1998).

[46] M. Landini, S. Roy, L. Carcagnì, D. Trypogeorgos, M. Fattori, M. Inguscio, and G. Modugno,"Sub-Doppler laser cooling of potassium atoms", Phys. Rev. A, **84**, 043432 (2011).

[47] J. Dalibard and Y. Castin, in the Frontiers in Laser Spectroscopy, proceedings of the CXX International School of Physics "Enrico Fermi".

[48] C. J. Cooper, G. Hillenbrand, J. Rink, C. G. Townsend, K. Zetie and C. J. Foot, Europhys. Lett. **28**, 397 (1994).

[49] A. Bambini, and A. Agresti, Phys. Rev. A **56**, 3040 (1997).

[50] C. Fort, A. Bambini, L. Cacciapuoti, F. S. Cataliotti, M. Prevedelli, G. M. Tino, and M. Inguscio, Eur. Phys. J. D **3**, 113 (1998).

[51] X. Xu, T. H. Loftus, J. W. Dunn, C. H. Greene, J. L. Hall, A. Gallagher, and J. Ye, Phys. Rev. Lett. **90**, 193002 (2003).

[52] S. Ferrari, "An apparatus for experiments with Bose-Einstein condensates with tunable interactions", Diploma thesis, Università degli studi di Milano.

[53] L. Carcagnì, "Un nuovo apparato per BEC ad interazione controllabile", Dipolma thesis, Università del Salento.

[54] G. Roati, M. Zaccanti, C. D'Errico, J. Catani, M. Modugno, A. Simoni, M. Inguscio, and G. Modugno, "39K Bose-Einstein condensate with tunable interactions", Phys. Rev. Lett. 99, 010403 (2007).

[55] R. L. D. Campbell, R. P. Smith, N. Tammuz, S. Beattie, S. Moulder, and Z. Hadzibabic, "Efficient Production of Large 39K Bose-Einstein Condensates", Phys. Rev. A **82**, 063611 (2010).

[56] A. Simoni, private communication.

[57] C. D'Errico, M. Zaccanti, M. Fattori, G. Roati1, M. Inguscio, G. Modugno, and A. Simoni, "Feshbach resonances in ultracold ^{39}K", New J. Phys. **9**, 223 (2007).

[58] M. Zaccanti, B. Deissler, C. D'Errico, M. Fattori, M. Jona-Lasinio, S. Müller, G. Roati, M. Inguscio, and G. Modugno, Nat. Phys. **5**, 586 (2009).

[59] T. Kraemer, M. Mark, P. Waldburger, J. G. Danzl, C. Chin, B. Engeser, A. D. Lange, K. Pilch, A. Jaakkola, H.-C. N*ä*gerl and R. Grimm, "Evidence for Efimov quantum states in an ultracold gas of caesium atoms", Nature **440**, 315 (2006).

[60] F. Ferlaino, R. Grimm, "Forty years of Efimov physics: How a bizarre prediction turned into a hot topic", Physics **3**, 9 (2010).

[61] R. Gati, J. Esteve, B. Hemmerling, T.B. Ottenstein, J. Appmeier, A. Weller, and M. K. Oberthaler N. J. Phys. **8**:189.

[62] A. Smerzi, S. Fantoni, S. Giovannazzi, and S. R. Shenoy, Phys. Rev. Lett. **79**, 4950 (1997).

[63] G. Schön and A. D. Zaikin, Phys. Rep. **198**, 237 (1990).

[64] L. Pitaevskii, and S. Stringari, Phys. Rev. Lett. **87**, 180402 (2001).

[65] M. Anderlini, J. Sebby-Strabley, J. Kruse, J. V. Porto, and W. D. Phillips, "Controlled atom dynamics in a double-well optical lattice", J. Phys. B **39**, S199-S210 (2006).

[66] S. Foelling, S. Trotzky, P. Cheinet, M. Feld, R. Saers, A. Widera, T. Mueller, I. Bloch, Nature **448**, 1029-1032 (2007).

[67] C. Gross, T. Zibold, E. Nicklas, J. Estève, and M. K. Oberthaler, "Nonlinear atom interferometer surpasses classical precision limit", Nature **464**, 1165-1169 (2010).